Electrochemical Texturing and Deposition of Transparent Conductive Oxide Layers for the Application in Silicon Thin-Film Solar Cells

Jan-Philipp Becker

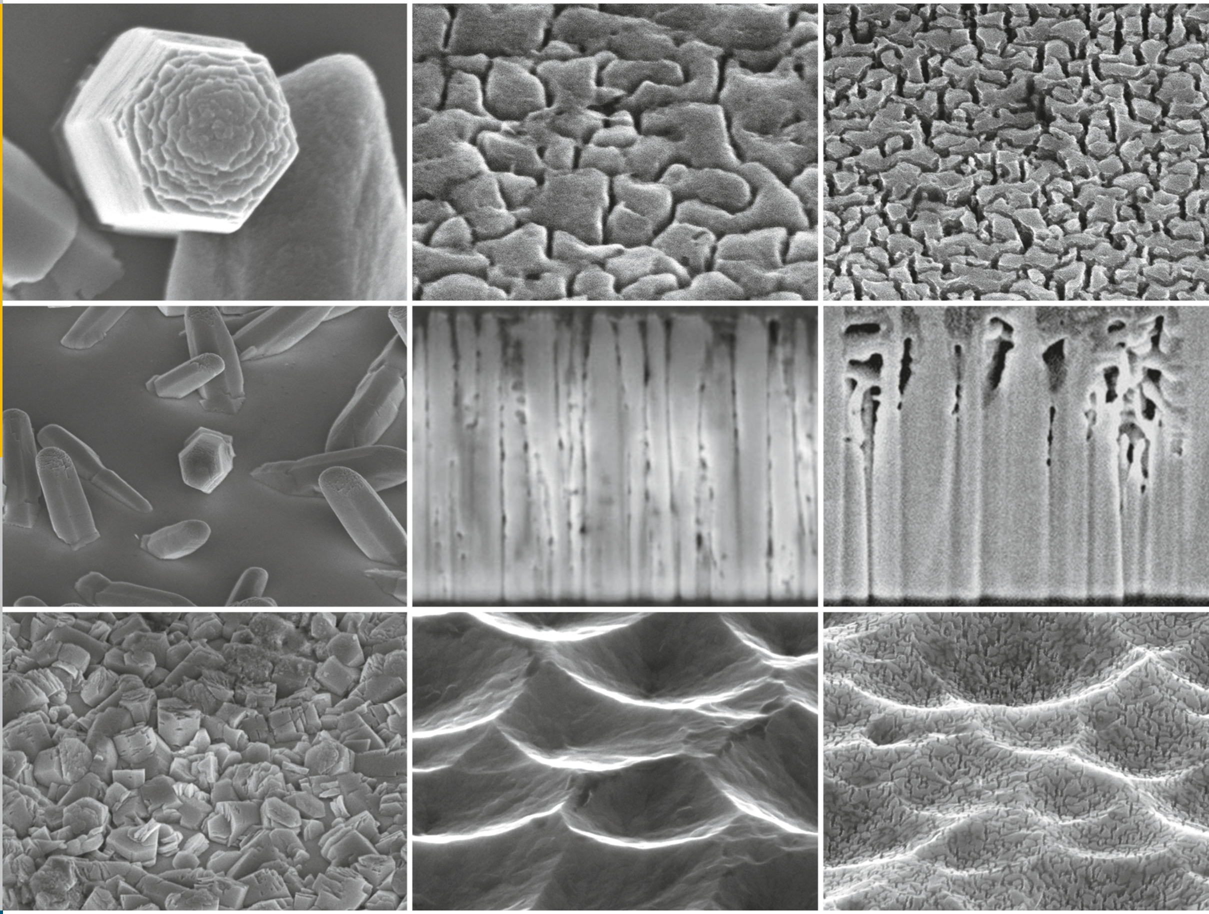

Member of the Helmholtz Association

Energie & Umwelt /
Energy & Environment
Band / Volume 247
ISBN 978-3-95806-027-2

JÜLICH
FORSCHUNGSZENTRUM

Schriften des Forschungszentrums Jülich
Reihe Energie & Umwelt / Energy & Environment Band / Volume 247

Forschungszentrum Jülich GmbH
Institute of Energy and Climate Research
IEK-5 Photovoltaics

Electrochemical Texturing and Deposition of Transparent Conductive Oxide Layers for the Application in Silicon Thin-Film Solar Cells

Jan-Philipp Becker

Schriften des Forschungszentrums Jülich
Reihe Energie & Umwelt / Energy & Environment Band / Volume 247

ISSN 1866-1793 ISBN 978-3-95806-027-2

Bibliographic information published by the Deutsche Nationalbibliothek.
The Deutsche Nationalbibliothek lists this publication in the Deutsche
Nationalbibliografie; detailed bibliographic data are available in the
Internet at http://dnb.d-nb.de.

Publisher and Distributor:	Forschungszentrum Jülich GmbH Zentralbibliothek 52425 Jülich Tel: +49 2461 61-5368 Fax: +49 2461 61-6103 Email: zb-publikation@fz-juelich.de www.fz-juelich.de/zb
Cover Design:	Grafische Medien, Forschungszentrum Jülich GmbH
Printer:	Grafische Medien, Forschungszentrum Jülich GmbH

Schriften des Forschungszentrums Jülich
Reihe Energie & Umwelt / Energy & Environment, Band / Volume 247

D 82 (Diss. RWTH Aachen University, 2014)

ISSN 1866-1793
ISBN 978-3-95806-027-2

Abstract

Doped zinc oxide layers are widely used in thin-film solar cells for several purposes, for instance as transparent contacts, as a source of light scattering and as part of the back reflector. Magnetron sputtered, aluminum-doped zinc oxide thin films provide very high transparency and conductivity, and are usually flat in the as-deposited state. To introduce light scattering, a surface texture is conventionally introduced by post-deposition etching in diluted hydrochloric acid. However, the ability to obtain suitable surface morphologies by chemical dissolution is strongly dependent on the deposition process. Thus, optimization of zinc oxide thin films requires a careful trade-off between optical, electric, and morphological properties. This markedly limits the process window and excludes layers with excellent optical and electric properties due to a lack of suitable texturing processes. Electrochemical methods can help to overcome these limitations by making novel zinc oxide structures accessible. Both deposition and dissolution can be achieved using electrochemical methods. In this context, an advanced understanding of the stability of polycrystalline zinc oxide thin films in aqueous solutions is crucial. This work investigates the zinc oxide/electrolyte interface under various conditions in order to further the understanding of the interfacial reactions and the zinc oxide itself.

Cathodic electrochemical deposition was used for the growth of zinc oxide films and nano-structures from aqueous solutions. This method utilizes specific manipulation of the interfacial pH at the substrate surface by reduction of a suitable precursor such as nitrate or molecular oxygen. The dependence of the zinc oxide precipitation and crystallization on several parameters such as the deposition potential, the bath temperature, the substrate, and the composition of the electrolyte were investigated. Temperatures above 50 °C were found to be necessary for the crystallization of well defined hexagonal crystals. The comparison of electrochemical deposition on indium tin oxide and zinc oxide substrates revealed the fundamental influence of the substrate on the nucleation. While the growth on zinc oxide seed layers seemed to proceed epitaxially, conserving the preferential c-axis orientation and crystallite size of the substrate, the nucleation on indium tin oxide substrates depended largely on the applied potential. With increasing cathodic potential the density of nucleation sites increased. The crystallite size decreased simultaneously. Due to a catalytic effect of Zn^{2+} ions in solution on the reduction of NO_3^-, the Zn^{2+} concentration plays a decisive role on the growth process and must be carefully adjusted. A Burstein-Moss shift was observed for electrochemically deposited zinc oxide suggesting degenerate doping by intrinsic defects, hydrogen, or chloride incorporated in the film.

The main determinant of the stability of zinc oxide in aqueous solutions is the *p*H. The chemical dissolution of polycrystalline zinc oxide thin films was investigated frequently. However, the dissolution rate and the film thickness were, so far, accessible only after the etching process. This work applies an electrochemical method which allows for the *in-situ* measurement of the dissolution rate. Therefore an online process control becomes feasible allowing to stop the process when a desired film thickness is dissolved. The evolution of the dissolution rate was monitored in several buffered and unbuffered acidic solutions. The measured values were in good agreement with values found in literature.

Electrochemical anodic dissolution of polycrystalline zinc oxide thin films was found to provide access to a novel type of surface textures. A unique surface morphology was obtained due to a pronounced selectivity of the anodic dissolution process to the close vicinity of the grain boundaries. The obtained surface features were too small to provide efficient light scattering, however, a decreased absorptance in the near infrared spectral range was observed. The selectivity of the etching process to the grain boundaries could be varied by the application of different electrolytes. Sulfate solutions showed the highest selectivity, which was ascribed to a buffering effect on the interfacial *p*H. Enhanced dissolution under illumination suggested that the dissolution kinetics were limited by the abundance of holes at the zinc oxide/electrolyte interface. The determination of the flat band potential by means of Mott-Schottky analysis provided access to the band alignment at the interface and revealed band to band tunneling as the dominant charge transfer process. A field enhancement at the grain boundaries was assumed to be the reason for the preferred dissolution at these sites.

To benefit from the increased transmittance of the electrochemically obtained texture and the light scattering provided by chemically introduced surface textures, both processes were combined in a two-step approach. Depending on the sequence either a superposition of both surface textures was obtained or a gradual adjustment of the feature size was feasible. The application of both types of two-step textured zinc oxide thin films as front contacts in microcrystalline silicon solar cells has proven their usability for thin-film photovoltaic devices.

Zusammenfassung

Zinkoxid wird in Dünnschichtsolazellen zu verschiedensten Zwecken eingesetzt. Als dünne Schichten findet es insbesondere als transparenter Kontakt, als Lichtstreuer oder als Teil des Rückreflektors Anwendung. Kathodenzerstäubte, aluminiumdotierte Zinkoxidschichten zeichnen sich dabei sowohl durch eine sehr hohe Transparenz als auch durch eine exzellente Leitfähigkeit aus. Die dünnen Schichten sind nach der Abscheidung typischerweise glatt und um sie für die Lichtstreuung einsetzen zu können, wird häufig eine Oberflächentextur erzeugt, die konventionell durch eine chemische Behandlung in verdünnter Salzsäure erreicht wird. In Prinzip ermöglicht dieses Vorgehen eine von den optoelektronischen Eigenschaften des Materials entkoppelte Einstellung der Lichtsteuung. In der Praxis ist die nasschemisch zugängliche Oberflächentextur allerdings stark von dem Depositionsprozess abhängig, so dass bei der Optimierung der Zinkoxidschichten für den Einsatz in Dünnschichtsolarzellen sorgfältig zwischen den optischen, den elektrischen und den morphologischen Eigenschaften der Schichten abgewogen werden muss. Dies schränkt das mögliche Prozessfenster bei der Deposition deutlich ein und führt dazu, dass einige Schichten mit exzellenten optischen und elektrischen Eigenschaften aufgrund fehlender Texturierungsprozesse keinen Eingesetzt finden. Elektrochemische Methoden können helfen, diese Limitierungen zu umgehen indem sie neue Oberflächenstrukturen zugänglich machen. Zinkoxid kann elektrochemisch sowohl abgeschieden als auch geätzt werden wobei für den gezielten Eiseatz beider Prozesse ein gutes Verständnis der Stabilität von polykristallinem Zinkoxid in wässriger Lösung nötig ist. Diese Arbeit beschäftigt sich daher mit der Zinkoxid/Elektrolyt-Grenzfläche unter verschiedensten chemischen Bedingungen und versucht damit, das Verständnis der Grenzflächenreaktionen und des Zinkoxids selbst zu erweitern.

Für das Wachstum von Zinkoxidschichten und -nanostrukturen aus wässrigen Lösungen wurde die kathodische elektrochemische Abscheidung verwendet. Dieses Verfahren nutzt die gezielte Manipulation des pH-Wertes an der Substratoberfläche durch die Reduktion geeigneter Prekursoren, wie Nitrat oder molekularen Sauerstoff. Die Abhängigkeit der Zinkoxidfällung und Kristallisation von Prozessparametern wie dem angelegten Potential, der Badtemperatur, des Substrats und der Zusammensetzung des Elektrolyten wurde untersucht. Es wurde beobachtet, dass Temperaturen oberhalb von 50 °C erforderlich sind um die Kristallisation von

gut definierten hexagonalen Kristallen zu ermöglichen. Der Vergleich der elektrochemischen Abscheidung auf Indiumzinnoxid- und Zinkoxid-Substraten verdeutlichte einen grundlegenden Einfluss des Substrats auf die Keimbildung. Während sich das Wachstum auf Zinkoxid-Saatschichten epitaktisch fortzusetzen schien, und c-Achsen-Vorzugsorientierung sowie Kristallitgröße des Substrats übernommen wurde, hing die Keimbildung auf ITO-Substraten stark von der angelegten Spannung ab. Mit zunehmendem Kathodenpotential erhöhte sich die Dichte der Nukleationszentren während sich die Kristallitgröße gleichzeitig verringerte. Aufgrund einer katalytischen Wirkung der Zn^{2+}-Ionen in der Lösung zur Reduktion von NO_3^-, spielt die Zn^{2+}-Konzentration eine entscheidende Rolle für den Wachstumsprozess und muss sorgfältig eingestellt werden. Für die elektrochemisch abgeschieden Zinkoxidschichten wurde eine Burstein-Moss-Verschiebung beobachtet, die auf eine entartete Dotierung durch intrinsische Defekte, eingebauten Wasserstoff oder Chlor hindeutet.

Die Stabilität von Zinkoxid in wässriger Lösung wird maßgeblich durch den *p*H-Wert bestimmt. Die chemische Auflösung von polykristallinen Zinkoxidschichten wurde bereits intensiv untersucht. Allerdings ist die Ätzrate experimentell bisher nur nach dem Ätzprozess zugänglich. In dieser Arbeit wird eine elektrochemische Methode genutzt, die es erlaubt die Ätzrate *in-situ* zu bestimmen. Dies ermöglicht eine instantane Prozesskontrolle, die es erlaubt den Ätzprozess zu unterbrechen wenn die gewünschte Schichtdicke erreicht ist. Die zeitliche Entwicklung der Ätzrate wurde in verschiedenen gepufferten und ungepufferten, sauren Lösungen untersucht. Die gemessenen Werte zeigten gute Übereinstimmung mit Literaturwerten.

Es konnte gezeigt werden, dass die elektrochemische anodische Auflösung von polykristallinen Zinkoxidschichten neue Oberflächentexturen zugänglich macht. Eine einzigartige Oberflächentextur, die auf anderem Wege nicht erreichbar ist, wurde durch eine ausgeprägte Selektivität des anodischen Auflösungsprozesses für die enge Umgebung der Korngrenzen erzeugt. Die erhaltenen Strukturen waren zwar zu klein um eine effiziente Lichtstreuung bereit zu stellen, führten aber zu einer deutlichen niedrigeren Lichtabsorption im nahen Infrarotbereich. Die Selektivität des Ätzprozesses auf die Korngrenzen konnte durch den Einsatz verschiedener Elektrolyten beeinflusst werden. Sulfathaltige Lösungen zeigten dabei die höchste Selektivität. Dies konnte auf einen Puffereffekt auf den Grenzflächen-*p*H-Wert zurückgeführt werden. Eine Beschleunigung der Ätzrate unter Beleuchtung mit UV-Licht legt nahe, dass die Kinetik der anodischen Auflösung durch die Verfügbarkeit von Löchern an der Zinkoxid/Elektrolyt-Grenzfläche limitiert ist. Die Ermittlung des Flachbandpotentials mittels der Mott-Schottky-Methode ermöglichte es die Bandstruktur an der Grenzfläche zu bestimmen. Darüber konnte gefolgert werden, dass Band-zu-Band-

Tunneln der dominierende Ladungstransferprozess ist. Eine Felderhöhung an den Korngrenzen ist vermutlich der Grund für die lokal bevorzugte Auflösung.

Um von der erhöhten Transmission der elektrochemisch texturierten Zinkoxidschichten bei gleichzeitig guter Lichtstreuung zu profitieren, wurde der elektrochemische Prozess mit einem konventionellen chemischen Ätzschritt kombiniert. In Abhängigkeit von der Sequenz der Schritte, konnte entweder eine Superposition der beiden Oberflächentexturen oder eine graduelle Einstellung der Oberflächenstrukturgröße erreicht werden. Die erfolgreiche Implementierung beider Arten von zweifach texturierten Zinkoxidschichten als transparente Frontkontakte in mikrokristallinen Siliziumdünnschichtsolarzellen wurde demonstriert.

Contents

1. Introduction 1

2. Transparent Conducting Oxides - Zinc Oxide 5
  2.1. Transparent Conducting Films 5
  2.2. Zinc Oxide 6
    2.2.1. Crystal Structure 7
    2.2.2. Electrical properties 8
      2.2.2.1. Doping 8
      2.2.2.2. Electrical Conduction in Solids 12
      2.2.2.3. Electrical Transport in TCO Thin Films 13
    2.2.3. Optical properties 13

3. Basics of Semiconductor Electrochemistry 19
  3.1. Basic Concepts of Electrochemistry 19
    3.1.1. The Electrochemical Potential 19
    3.1.2. Absolute Electrode Potential 20
  3.2. The Electrochemical Setup 21
    3.2.1. Three-Electrode Configuration 21
  3.3. The ZnO/Electrolyte Interface 22
    3.3.1. Charge and potential distribution 23
    3.3.2. Charge Transfer 27
  3.4. Stability of ZnO in Aqueous Electrolytes 29

4. Electrochemical Deposition of Zinc Oxide 31
  4.1. Introduction 31
  4.2. Results and Discussion 34
    4.2.1. Electrochemical Deposition from Zinc Nitrate Solutions 34
      4.2.1.1. Experimental Conditions 35
      4.2.1.2. Zinc Concentration and Temperature 35
      4.2.1.3. Current density 37
    4.2.2. Electrochemical Deposition from Chloride and Perchlorate Solutions 38
      4.2.2.1. Experimental Conditions 40

4.2.2.2. Substrate, Potential, and Supporting Electrolyte . . 40
4.2.2.3. Optical Properties and Band Gap 45
4.3. Conclusion 48

5. Chemical Dissolution of Zinc Oxide 51
5.1. Electrochemical Determination of the Chemical Dissolution Rate of Metal Oxides 53
5.2. Application to ZnO:Al thin films 56
5.2.1. Integrity of the Method 57
5.2.2. Unbuffered Acids 58
5.2.3. Acetate Buffer 62
5.3. Discussion 64

6. Electrochemical Dissolution of Zinc Oxide 67
6.1. Introduction 67
6.2. Experimental 69
6.3. Results 69
6.3.1. Electrochemical Dissolution Rate 72
6.3.2. Potential Dependence 74
6.3.3. The Electrolyte 75
6.3.3.1. The Anion Species 75
6.3.3.2. Buffered Electrolytes 83
6.3.4. Photo-anodic Dissolution of ZnO:Al 85
6.3.5. Detection of the Aluminum Dopant 87
6.4. Discussion 91
6.4.1. Charge Transfer 93
6.4.2. Influence of the Anion Species 96
6.4.3. Influence of the solution pH 98
6.4.4. Applicability of Electrochemically Anodized ZnO:Al to Solar Cells 99
6.5. Summary 99

7. Integration of Electrochemically Textured ZnO:Al Layers into Thin-Film Silicon Solar Cells 101
7.1. Experimental 101
7.2. Combined Texturing 102
7.3. Tuning the Surface Texture Size 110
7.4. Conclusion 118

8. Conclusion and Future Prospects **121**

Bibliography **127**

A. Methods and materials **III**
- A.1. Sputter Deposition Systems III
  - A.1.1. Zinc Oxide Sputter Deposition III
  - A.1.2. Indium Tin Oxide Sputter Deposition IV
- A.2. Solar Cell Deposition V
- A.3. Electrochemical Measurements V
- A.4. Physical and Chemical Characterization of Thin Films VII
  - A.4.1. Profilometer VII
  - A.4.2. UV-VIS-NIR Photospectroscopy VIII
  - A.4.3. Photothermal Deflection Spectroscopy (PDS) VIII
  - A.4.4. Hall Measurements VIII
  - A.4.5. Scanning Electron Microscopy (SEM) IX
  - A.4.6. Focused Ion Beam (FIB) X
  - A.4.7. X-ray Photoelectron Spectroscopy X
  - A.4.8. Raman Spectroscopy X
- A.5. Solar Cell Characterization XI
  - A.5.1. Spectral Response and Quantum Efficiency XI
  - A.5.2. Current-Voltage Characteristic XI

Glossary **XIII**

Publications **XIX**

Curriculum Vitae **XXI**

Acknowledgements **XXIII**

1. Introduction

Transparent conductive oxides (TCOs) are a unique class of materials that exhibit both transparency and electronic conductivity at the same time. These materials have found wide spread use in today's technologies such as displays, photovoltaics, "low-e" windows and flexible electronics. In many of these applications TCOs are crucial in their role as transparent contacts. However, current demands extend beyond the requirement of conductivity and transparency. Additional performance is needed, taking into account morphology, processing and patterning requirements, cost and elemental abundance.

Doped zinc oxide is one of the most widely used TCOs. It is a large band gap, n-type semiconductor which can be deposited using several chemical and physical deposition techniques. Its high abundance, cost efficiency, and excellent opto-electronic properties make it a promising candidate for diverse applications. In particular, its utilization as a transparent front contact in silicon thin-film solar cells has proven very successful. This type of solar cell features a very thin silicon absorber, usually below 2 µm, which makes it a very material- and cost-efficient photovoltaic technology. The optimization of the front contact is crucial for high cell efficiency. Beside the need to minimize optical and ohmic losses due to parasitic absorption or electric resistance in the front contact, light scattering structures have to be implemented in order to enable elongated pathways of light within the active silicon layers. In the ideal case, this leads to *trapping* of the incident light within the silicon absorber.

Zinc oxide thin films can be grown with a rough surface using chemical vapor deposition or solution based techniques. However, sputter-deposited zinc oxide thin films that satisfy high demands on opto-electronic properties are generally flat. Therefore, the surface is regularly textured by acidic etching to introduce light scattering surface features [1]. In principle, this allows for the separate optimization of the opto-electronic properties and the surface texture. However, the actual surface texture was found to depend on the deposition conditions rather than the etchant [2,3]. In fact, all investigated acids provide crater-shaped surface features. Furthermore, the feature size is mainly determined by the deposition conditions. An exception is hydrofluoric acid which was found to provide somewhat smaller surface features [4]. However, in this case the deposition process still has to be tailored in order to optimize electric, optical, and surface properties simultaneously. Also, zinc oxide thin films with superior opto-electronic properties, obtained by slight changes of the deposition parameters [2,3], cannot be employed due to the lack of suitable texturing processes. Thus, new approaches are necessary to allow for novel types of surface textures.

The quest for new ways of energy conversion and storage to subsidize fossil energy sources has recently stimulated a huge amount of interest in electrochemistry. Electrochemical devices such as fuel cells and batteries are constantly being improved. The interfaces between electronic conductors and electrolytes play a key role in this context. Especially the semiconductor/electrolyte interface is crucial to several applications such as dye sensitized solar cells and photocatalytic watersplitting. Furthermore, the close relation between electrochemistry and neighboring sciences, like surface science or semiconductor physics has resulted in cross-fertilizing effects.

Because the dissolution of n-type semiconductors is generally an electrochemical process, the extension of the conventional, purely chemical texturing to electrochemical texturing technique seems natural and intuitive. Despite this fact, the electrochemical dissolution of zinc oxide thin films has not yet been used to introduce light scattering surface morphologies, even though the first studies on the electrochemical behavior of zinc oxide date back to the 1960's [5,6]. In fact, besides silicon, zinc oxide is one of the most frequently studied semiconductors in electrochemistry. Thus, a large proportion of the early understanding of the semiconductor/electrolyte interface resulted from investigations on crystalline zinc oxide electrodes. However, electrochemical studies on polycrystalline zinc oxide are sparse. Its structural inhomogeneity introduces local fluctuations on the reaction kinetics, making a systematic understanding of the interface processes challenging. Despite the recent interest in electrochemically deposited zinc oxide structures, for instance as transparent electrodes in organic or dye sensitized solar cells, systematic studies on their stability in aqueous electrolytes are lacking.

This work aims to fill this gap in semiconductor electrochemical research. The stability of polycrystalline zinc oxide thin films in aqueous media will be the central topic of this thesis. In particular, the polycrystalline zinc oxide/electrolyte interface will be studied extensively under various conditions. The electrochemical methods applied in this work will not only enable the study of interfacial reactions, but also allow for specific surface manipulations. Thus, electrochemical deposition and dissolution of zinc oxide will be used to obtain zinc oxide structures which might help to improve light management in thin-film solar cells. Furthermore, results will be presented that may contribute to the general understanding of the electrochemistry of polycrystalline semiconductors.

This work consists of the following: First, in chapter 2, an introduction to transparent conductive oxides with a focus on degenerately doped zinc oxide thin films is presented. In particular, a review of the relevant research and prior knowledge is provided to offer a basis for the understanding of the various experiments that are discussed later on. Chapter 3 covers the basics of semiconductor electrochemistry in general and introduces the background information that is necessary to understand the zinc oxide/electrolyte interface. In this, special attention is payed to the stability of the electrode.

The results of new experiments on zinc oxide are presented in chapter 4. This chapter focuses on results obtained from the electrochemical deposition of zinc oxide. This solution based growth technique has shed new light on the deposition-dissolution equilibrium and on how diverse zinc oxide structures from closed films to nanowires can be achieved. In addition, the dependence of the initial growth phase on the substrate and the electrolyte were investigated.

The chemical stability of zinc oxide is examined in chapter 5. Here, an elegant technique for the *in-situ* determination of the chemical dissolution rate of zinc oxide was used to investigate the dissolution kinetics in selected buffered and unbuffered acidic solutions. Chapter 6 focuses on the electrochemical stability of polycrystalline zinc oxide thin films. In particular, a novel surface texture was obtained by anodic polarization. A comprehensive study of the key parameters in the anodic process is presented and the charge transfer at the polycrystalline zinc oxide/electrolyte interface are discussed.

While chapters 4 - 6 are largely fundamental in nature, with respect to the presented research, chapter 7 is application oriented. Specifically, the unique surface texture obtained by anodic polarization was combined with a conventional chemically obtained texture using two different sequences. One allowed both textures to be superimposed and the other allowed for the gradual tuning of the texture size. The surface textured zinc oxide thin films that were obtained, were then implemented as front contacts in silicon thin-film solar cells. The measuring stations that were utilized and all necessary information on measurement errors are described in the appendix A. Finally, chapter 8 provides a short summary and discusses the future prospects of this work.

2. Transparent Conducting Oxides - Zinc Oxide

This chapter gives an introduction to transparent conducting materials with focus on degenerately doped zinc oxide thin films for the application in silicon thin-film solar cells. Section 2.1 names demands made on transparent conductors and presents suitable candidates. Section 2.2 focusses exclusively on zinc oxide and addresses it crystalline, electric and optical properties.

2.1. Transparent Conducting Films

For the fabrication of opto-electronic devices such as thin-film solar cells or flat panel displays optically transparent contact layers are needed. The two main requirements are high electrical conductivity as well as transparency in a wide spectral range. There are both organic and inorganic materials that fulfil these requirements. Examples are graphene [7, 8], carbon nanotube networks [9], and conductive polymers [10, 11], silver nanowire networks [12, 13] and several degenerately doped metal oxides, often referred to as transparent conducting oxides (TCO).

According to Freeman *et al.* [14] a good TCO must fulfill three requirements:

(i) strong curvature of the conduction band to give high carrier mobilities,

(ii) the gap between valence and conduction band must be wide enough to transmit the visible spectrum, and

(iii) retention of good optical properties with high doping levels.

Oxides with a band gap of 3 eV or more are insulators at room temperature. To become conductors, the oxides must be doped to degeneracy by increasing the free carrier density such that the Fermi level is shifted into the conduction band. This so called degenerate doping requires a source of electron donors in the form of point defects (often oxygen vacancies) or impurities with an ionization energy close to the conduction band. This limits the selection of TCO materials severely. All current practical transparent conductors are degenerately doped *n*-type with either intentionally added impurities or native point defects created through non-stoichiometric deposition conditions. Suitable candidates are doped In_2O_3, SnO_2, ZnO, CdO, and TiO_2. The most intensely investigated and utilized TCOs are tin-doped indium oxide (In_2O_3:Sn), fluorine-doped tin oxide (SnO_2:F), and aluminum-doped zinc oxide (ZnO:Al). Review articles on the variety of TCOs can be found in Ref. [15–17].

With respect to sustainable large scale production of high efficiency thin-film solar cells, besides electric conductivity and optical transparency, further considerations such as scarcity of composing materials and environmental and health aspects (toxicity of materials) have to be taken into account [18]. Additionally, the ability to deposit homogeneously on a large scale must be considered. Furthermore, for silicon based thin-film solar cells, the ability to introduce light scattering surface textures within the transparent conducting film must be taken into account. With these additional constrains in mind, the best two candidates currently available for use as transparent contacts in thin-film silicon solar cells are doped SnO_2 and ZnO thin films. Both, namely SnO_2:F and ZnO:Al/ZnO:B, have proven to be suitable transparent contact layers in silicon thin-film photovoltaic devices [19–23]. They exhibit similar optical and electrical properties, however, different chemical properties provide different advantages and disadvantages. The higher formation energy for SnO_2 of 6.0 eV, compared to 3.6 eV for ZnO, makes it less susceptible to environmental or acidic degradation [20]. In contrast, ZnO has proven much more stable than SnO_2 in a hydrogen plasma which is used in the plasma enhanced chemical vapor deposition (PECVD) of silicon [24,25].

2.2. Zinc Oxide

Zinc oxide is nowadays widely used in varistors [26], gas sensors [27], light emitting diodes [28], and photovoltaic devices [29,30] due to its merits such as being non-toxic, low cost and easy to process during large scale commercialization. A variety of deposition techniques is utilized to produce doped zinc oxide thin films, including vapor deposition techniques such as pulsed laser deposition (PLD) [31–33], chemical vapor deposition (CVD) [30,34,35], and sputter deposition [2,36–38]. Furthermore, liquid phase deposition is feasible, e.g. the sol-gel technique [39–41], electrochemical deposition [42,43], and spray pyrolysis [44,45]. Among these deposition methods, magnetron sputter deposition is an established technique that offers the advantage of enabling the production of homogeneous thin films on large areas up to several m^2 at moderate temperatures, thus, being applicable for industrial production. Comprehensive text books about zinc oxide in its various forms and applications are available [46–50]. Ref. [46] is in particular concerned with ZnO films for the application in thin-film photovoltaics.

2.2.1. Crystal Structure

ZnO generally crystallizes in the wurtzite crystal structure. However, it can be grown with zincblende structure when deposited on a cubic lattice substrate such as gallium arsenide [51], or with rocksalt structure when grown at high pressures [52, 53] or strongly alloyed with another material such as magnesium oxide [50]. The wurtzite crystal structure, as shown in Fig. 2.1, is a hexagonal lattice and generally characterized by two lattice constants $a = 0.325\,\mathrm{nm}$ and $c = 0.521\,\mathrm{nm}$ as measured by x-ray diffraction (XRD) measurements at room temperature [54]. The ratio of $c/a = 1.60$ is close to the ideal ratio for a hexagonal cell $c/a = (8/3)^{1/2} \approx 1.63$. The wurtzite crystal structure belongs to the hexagonal system with space group C_{6v}^4 ($P6_3mc$) in the Schoenflies (short standard) notation [55]. Each of two atom species occupy the positions of a closest packed hexagonal lattice. These two sublattices are shifted along the c-axis against each other (Fig. 2.1). The wurtzite-structure lattice is fourfold coordinated and has no inversion symmetry along the c-axis, so the (0001) and $(000\bar{1})$ planes are Zn- and O-terminated, respectively (Fig. 2.1). Besides these polar c-axis oriented faces, the two non-polar $(11\bar{2}0)$ (a-axis) and $(10\bar{1}0)$ faces are common, both containing an equal number of Zn and O atoms. The polar faces are known to possess different chemical and physical properties, and the O-terminated face possesses a slightly different electronic structure to the other three faces [56]. The Zn-O bond is highly ionic, due to the large difference in their electronegativity values (1.65 for Zn and 3.44 for O) [57]. These polar bonds lead to planes of positively charged zinc and negatively charged oxygen atoms perpendicular to the c-axis. The combination of a lack of inversion symmetry and the polarization of the atomic planes gives ZnO the properties of being both piezoelectric and pyroelectric.

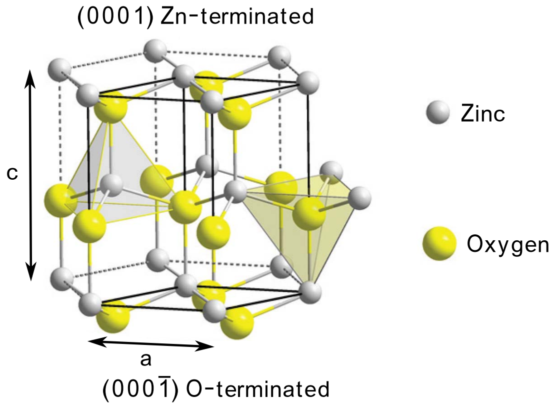

Fig. 2.1. Wurtzite crystal structure of ZnO. The polar Zn- and O-terminated faces of the c-axis are indicated. The unit cell containing two of each atom is indicated by solid black lines. Zn and O atoms are tetrahedrally bound to the four nearest O and Zn atoms, respectively [58].

2.2.2. Electrical properties

2.2.2.1. Doping

ZnO is a direct band gap semiconductor with a gap of approximately 3.3 eV (Table 2.1). In a semiconductor, the intrinsic Fermi level lies in the middle of the band gap. Thus, in stoichiometric ZnO, very few electrons are thermally or optically excited from the valence to the conduction band, exhibiting carrier densities as low as $n = 1 \times 10^6\,\mathrm{cm}^{-3}$ [59]. Thus, the carrier concentration must be drastically increased to use ZnO as a TCO. This can be done by intrinsic, extrinsic, and hydrogen doping. At high enough carrier concentration, the ZnO becomes degenerately doped and it behaves as if it were a metal. The critical carrier concentration (n_crit) required for a semiconductor to become degenerate is given by the Mott criterion [60],

$$n_\mathrm{crit}^{1/3}\, a_0^* \approx 0.26. \tag{2.1}$$

The effective Bohr radius a_0^* is given by

$$a_0^* = \frac{\mathrm{h}^2\, \varepsilon\, \varepsilon_0}{\pi\, e^2\, m_e^*} \tag{2.2}$$

where h, ε_0, ε, and m_e^* are Planck's constant, the permittivity of free space, the dielectric constant, and the effective electron mass, respectively. The dielectric constant for ZnO is $\varepsilon = 8.656$ [59]. Thus, for ZnO, the effective Bohr radius is $a_0^* = 1.7\,\text{nm}$ and the critical carrier concentration is $n_{\text{crit}} = 5 \times 10^{18}\,\text{cm}^{-3}$. This carrier concentration is well below those typically found in this work. Therefore, the ZnO thin films used throughout this work can be assumed electrically to behave like metals.

The incorporation of dopants in metal oxides and other ionic materials can be conveniently described with the Kröger-Vink notation [61], which is summarized in Fig. 2.2. For a more extensive description the reader is referred to textbooks on this subject [62, 63]. The references [64–66] deal with the particular defect chemistry of ZnO.

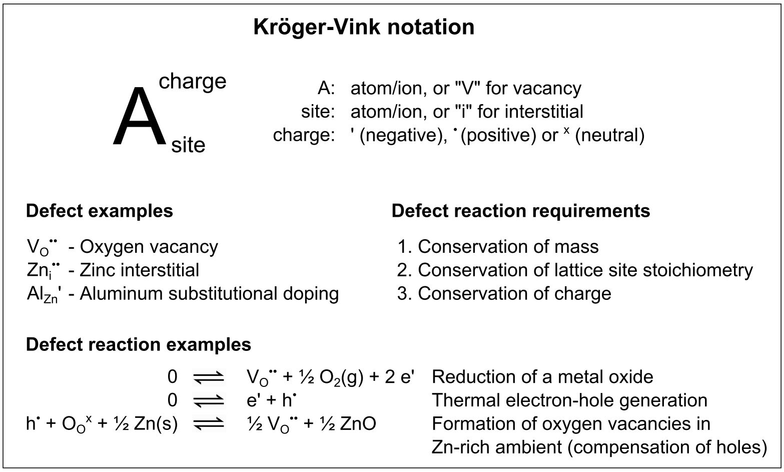

Kröger-Vink notation

$A_{\text{site}}^{\text{charge}}$

A: atom/ion, or "V" for vacancy
site: atom/ion, or "i" for interstitial
charge: ' (negative), $^\bullet$ (positive) or ^{x} (neutral)

Defect examples

$V_O^{\bullet\bullet}$ - Oxygen vacancy
$Zn_i^{\bullet\bullet}$ - Zinc interstitial
Al_{Zn}' - Aluminum substitutional doping

Defect reaction requirements

1. Conservation of mass
2. Conservation of lattice site stoichiometry
3. Conservation of charge

Defect reaction examples

$0 \rightleftharpoons V_O^{\bullet\bullet} + \frac{1}{2} O_2(g) + 2\,e'$ Reduction of a metal oxide
$0 \rightleftharpoons e' + h^\bullet$ Thermal electron-hole generation
$h^\bullet + O_O^x + \frac{1}{2} Zn(s) \rightleftharpoons \frac{1}{2} V_O^{\bullet\bullet} + \frac{1}{2} ZnO$ Formation of oxygen vacancies in Zn-rich ambient (compensation of holes)

Fig. 2.2. Diagram summarizing the key elements of the Kröger-Vink notation for point defects in ZnO. The formation of defects can be described with defect-chemical reactions and corresponding equilibrium constants. Adapted from [67].

When describing defect chemical reactions, the conservation of mass and charge has to be considered, as for any other chemical (half)reaction. Beyond that, in the defect chemistry of ionic solids one has to take into account the conservation of lattice site stoichiometry. For example, if zinc oxide is doped with Al_2O_3, two Al ions substitute for Zn, and two oxygen ions occupy two oxygen sites while the third occupies an interstitial site.

$$\mathrm{Al_2O_3} \xrightarrow{\mathrm{2ZnO}} \mathrm{2Al^{\bullet}{}_{Zn}} + \mathrm{2O_O^x} + \mathrm{O_i^{''}} \tag{2.3}$$

If the synthesis is performed under Zn-rich conditions the oxygen interstitials can be prevented by the following defect reaction which provides an electron, thus, increasing the n-type conductivity of the ZnO.

$$\mathrm{O_i^{''}} + \mathrm{Zn} \rightleftharpoons \mathrm{ZnO} + \mathrm{e^{'}} \tag{2.4}$$

Intrinsic doping results from defects within the crystal structure. Small deviations from the stoichiometric composition of the ZnO crystal result in vacancies of oxygen atoms ($\mathrm{V_O^{\bullet\bullet}}$) or zinc atoms on interstitial lattice sites ($\mathrm{Zn_i^{\bullet\bullet}}$). In these cases, the zinc valence electrons are not tetrahedrally bonded to oxygen atoms (see Fig. 2.1). The Zn-Zn bond is much weaker, building energy states in the band gap. Thus, energies much smaller than that of the band gap can excite electrons from the valence to the conduction band. Unintentionally doped ZnO is n-type. Carrier concentrations larger than $n > 1 \times 10^{20}$ cm^{-3} have been reported for intrinsically doped ZnO [68]. However, annealing under atmospheric conditions reduces the carrier concentration of the intrinsically doped ZnO films permanently, which is attributed to the chemisorption of oxygen [69]. Thus, solely intrinsically doped ZnO is generally not used for TCO applications.

Extrinsic doping in the form of intentionally added impurities can be either cationic (*e.g.*, $\mathrm{B^{3+}}$, $\mathrm{Al^{3+}}$, $\mathrm{Ga^{3+}}$, or $\mathrm{In^{3+}}$ substitutionally on the two-valent Zn site in ZnO) [23, 29, 70, 71] or anionic (*e.g.*, $\mathrm{F^-}$ or $\mathrm{Cl^-}$ substitutionally on an O site) [72–74]. This leads to an increased n-type conductivity. The donor binding energies (the energy required to free the extra valence electron) are 53.0, 54.5, and 63.2 meV for aluminum, gallium, and indium, respectively [75]. Most work to date has focused on Al-doped ZnO. This dopant requires a high degree of control over the oxygen potential in the sputter gas because of the high reactivity of Al with oxygen [76, 77]. Gallium is less reactive and has a higher equilibrium oxidation potential, which makes it theoretically a better choice for ZnO doping applications. Furthermore, the slightly smaller bond length of Ga-O (1.92 Å) compared to Zn-O (1.97 Å) offers the advantage of minimizing the deformation of the ZnO lattice at high substitutional doping concentrations. However, opto-electronical properties of ZnO:Ga, so far, did not achieve the high quality of ZnO:Al. While n-type doping is thus relatively easy to accomplish *p*-type remains elusive. It is typical for wide band gap semiconductors to be easily doped *n*- or *p*-type, but not both. This asymmetry has been attributed to the fact that a wide band gap semiconductor has a low valence band maximum or high conduction band minimum with respect to the vacuum level, leading to the so-called doping pinning rule [78]; materials with a low valence band tend to be *p*-type and a those with a high conduction band tend to be *n*-type. As mentioned previously, the intrinsic defects are *n*-type, so *p*-type dopants must first compensate for these carriers.

Hydrogen doping results from the incorporation of hydrogen into the crystal lattice. It can play a role in both *n*-type and *p*-type doping. The incorporation of hydrogen into the film during growth is unavoidable. In this respect, hydrogen doping is an intrinsic property of the film, as the doping effect is not intentional. The hydrogen incorporation depends strongly on ZnO preparation with concentrations as low as $5 \times 10^{16}\,\mathrm{cm}^{-3}$ in single crystals and as high as $1 \times 10^{20}\,\mathrm{cm}^{-3}$ in magnetron sputtered polycrystalline ZnO:Al films [79]. In contrast to the situation in many other semiconductors, hydrogen doping does not compensate extrinsic dopants, but tends to exhibit *n*-type behavior [80]. Hofmann et al. showed that in ZnO, incorporated hydrogen is always a shallow donor [81]. Thus, ZnO films can be extrinsically doped by introducing hydrogen to the ZnO during growth [82]. The donor binding energy for the electron to the hydrogen atom is about 60 meV [83], which is comparable with other common dopants.

Doping limits in ZnO are important in two aspects: The possibility for *p*-type doping and the possibility for degenerate *n*-type doping. *P*-type conductivity requires a Fermi energy close to the valence band maximum, where the formation enthalpy of compensating donors is very low. According to defect calculations, the most important intrinsic defect for the compensation of *p*-type conductivity is the oxygen vacancy ($\mathrm{V}_{\mathrm{O}}^{\bullet\bullet}$). On the other hand, the formation of zinc vacancies ($\mathrm{V}_{\mathrm{Zn}}''$) will limit *n*-type doping in ZnO. That this limitation occurs for Fermi level positions well above the conduction band minimum is a prerequisite for a transparent conducting electrode material, as otherwise no high electron concentrations are possible. However, it is indeed observed experimentally that the doping efficiency (number of free carriers per dopant atom) decreases with the increase of the dopant concentration [84].

2.2.2.2. Electrical Conduction in Solids

Following well-known Ohm's law, the current density j at a given location in a material depends on the product of the local electric field E and the conductivity σ of the material,

$$\vec{j} = \sigma \vec{E}. \tag{2.5}$$

The conductivity and its inverse, the resistivity $\rho = 1/\sigma$, are material dependent. A very successful classical model for the conduction of electrons through metals was proposed by Drude in 1900 [85]. This model assumes fixed positively charged ions and free negatively charged electrons. The only interaction considered is the collision between the two species. This allows for the treatment of the electrons as a gas and application of kinetic theory. The current density is then given by the product of the electron density n, the elementary charge e, and the drift velocity of the electrons v_d,

$$\vec{j} = -n\,\mathrm{e}\,\vec{v}_\mathrm{d}. \tag{2.6}$$

In the presence of an electric field, electrons are accelerated between collisions with localized ions and their drift velocity is given by,

$$\vec{v}_\mathrm{d} = -\frac{\mathrm{e}\,\tau}{m_\mathrm{e}^*}\,\vec{E}, \tag{2.7}$$

with τ and m_e^* being the average time between collisions and the effective electron mass [86], respectively. Thus, equation (2.6) can be rewritten as

$$\vec{j} = -\frac{n\,\mathrm{e}^2\,\tau}{m_\mathrm{e}^*}\,\vec{E}. \tag{2.8}$$

Comparing equation (2.8) with the general form of Ohm's law, equation (2.5), the conductivity, as given by the Drude model, can be identified as

$$\sigma = \frac{n\,\mathrm{e}^2\,\tau}{m_\mathrm{e}^*} =: \mathrm{e}\,n\,\mu, \tag{2.9}$$

where the charge carrier mobility μ is defined as the ratio of the drift velocity to the magnitude of the electric field,

$$\mu = \frac{v_\mathrm{d}}{E} = \frac{\mathrm{e}\,\tau}{m_\mathrm{e}^*}. \tag{2.10}$$

2.2.2.3. Electrical Transport in TCO Thin Films

In degenerately doped polycrystalline materials such as ZnO:Al additional scattering mechanisms are limiting the charge carrier transport. The most dominant processes that limit charge carrier mobility are collisions of charge carriers with oppositely charged dopant nuclei, known as ionized impurity scattering [87–89], and the scattering at grain boundaries which form potential energy barriers due to the locally high density of defects [89–93]. Furthermore, phonon scattering [94–97], piezoelectric mode scattering [98, 99], neutral impurity scattering [100], and dislocation scattering [101] are possible scatter mechanisms in polycrystalline degenerately doped semiconductors. The total charge carrier mobility as measured by Hall measurements/van der Pauw method is given by an inverse relationship of the sum of the mobilities due to the various scatter mechanisms i,

$$\frac{1}{\mu_\mathrm{meas}} = \sum_\mathrm{i} \frac{1}{\mu_\mathrm{i}}. \tag{2.11}$$

2.2.3. Optical properties

Light that is incident on a material can be either reflected, absorbed, or transmitted. Which of these processes is dominant depends on the material and the wavelength λ of the incident radiation. The reflectance R and the total transmittance T_t can be measured and, due to conservation of energy, the absorptance A is assumed to account for the rest of the incident light,

$$A(\lambda) = 1 - T_\mathrm{t}(\lambda) - R(\lambda). \tag{2.12}$$

The probability of transmission can be derived from the Drude (free electron) model (section 2.2.2.2). The permittivity (resistance to the formation of an electric field within a medium) is given by the dielectric function ε as a function of angular frequency ω as

$$\varepsilon(\omega) = 1 - \frac{n\,\mathrm{e}^2}{\varepsilon_\infty\,\varepsilon_0\,m_\mathrm{e}^*\,\omega^2} = 1 - \frac{\omega_\mathrm{p}^2}{\omega^2} \tag{2.13}$$

where ε_∞ is the high-frequency dielectric constant and the plasma frequency ω_p is defined as

$$\omega_\mathrm{p} = \sqrt{\frac{n\,\mathrm{e}^2}{\varepsilon_\infty\,\varepsilon_0\,m_\mathrm{e}^*}}. \tag{2.14}$$

The derivation of equation (2.13) from the equations of motion for a free electron gas can be found elsewhere [102]. Wavelength and angular frequency are related by

$$\lambda = \frac{2\,\pi\,\mathrm{c}}{\omega}, \tag{2.15}$$

where c is the speed of light in vacuum. Ideally, when the angular frequency of the incoming light is greater than the plasma frequency ($\omega > \omega_\mathrm{p}$), the dielectric function is positive and light can propagate through the material. In contrast, when the angular frequency of the incoming light is smaller than the plasma frequency ($\omega < \omega_\mathrm{p}$), the dielectric function is negative and light cannot propagate through the material. Hence, the light is reflected. When the angular frequency of the incoming light is equal to the plasma frequency ($\omega = \omega_\mathrm{p}$), the dielectric function is zero and equal portions are transmitted and reflected. The plasma frequency is the resonance frequency of the charge carriers, and incident light of this frequency is absorbed strongly. The polycrystalline ZnO:Al films are far from perfect crystals, and the effects of the plasma frequency are not confined to one particular wavelength. The width of the absorption peak about the plasma frequency depends on the mobility of the charge carriers [103]. Samples with higher mobilities exhibit more sharply-defined resonance peaks. The absorption at the plasma frequency is referred to as free carrier absorption.

The optical and electrical properties of ZnO are strongly interdepend. Fig. 2.3 displays the absoptance, reflectance, and transmittance of unetched ZnO:Al thin films with low and high carrier concentrations n as a function of the wavelength of the incident light. The optical spectrum can be devided into three regions, which will be discussed separately; the ultraviolet region (UV) between 300 and 400 nm, the visible (Vis) and near infrared region (NIR) between 400 and 1000 nm, and the infrared region (IR) between 1000 and 2500 nm. Depending on the band gap of the active material in a solar cell, the transmitted portion of the ultraviolet spectrum, make up the usable solar spectrum for solar cells. Thus, for efficient solar cells, the transmission through ZnO:Al is of particular interest.

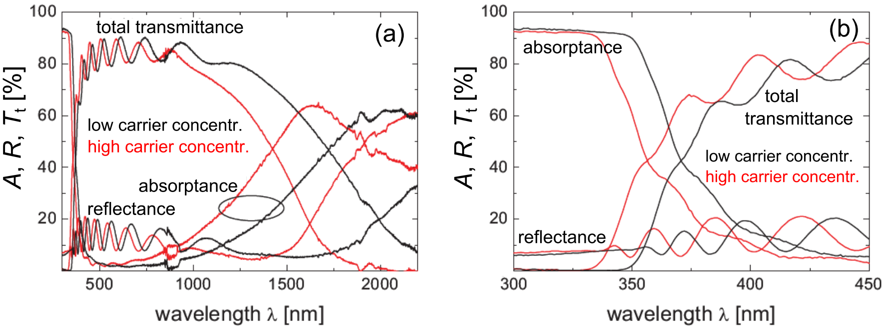

Fig. 2.3. Absorptance A, reflectance R, and total transmittance T_t of ZnO:Al thin films with low and high aluminum concentration in the wavelength range between (a) 300 and 2500 nm and (b) 300 and 450 nm. Adapted from [58].

Ultraviolet region (300-400 nm): Fig. 2.3(b) shows the high energy region of the optical spectrum. At wavelengths smaller than 350 nm the ZnO thin film with a low carrier concentration exhibits high absorptance. The absorptance then drops off and becomes relatively small by 400 nm, the transmission shows the opposite effect. This sharp transition is related to the band gap of ZnO. The energy of the incident light E_{photon} as a function of wavelength λ is given by Planck's relation,

$$E_{\text{photon}}(\lambda) = \frac{\mathrm{h\,c}}{\lambda}. \tag{2.16}$$

Incident light with an energy greater than the band gap of ZnO (about 350 nm), is readily absorbed while light with a lower energy is transmitted primarily through the ZnO:Al. Increasing the charge carrier concentration in ZnO:Al shifts the absorption edge towards a higher wavelength [3, 104] (see Figure 2.3 (b, red)). A similar effect is also observed for other semiconductors [105–107]. Burstein [105] and Moss [106] explained that this increase in the optical band gap is due to full energy states in the conduction band. This is the case in degenerately doped semiconductors where the Fermi level is very close to, or above the conduction band edge. If the lowest energy states in the conduction band are occupied, according to the Pauli exclusion principle, an electron, which is exited from the valence band into the conduction band, must occupy an unoccupied state at a higher energy. Thus, the optical band gap is shifted to higher energies. This so-called Burstein-Moss shift allows more transmission of ultraviolet light through ZnO:Al [104]. The increase in the energy of the band gap, ΔE_{BM}, is given by

$$\Delta E_{\mathrm{BM}} = \frac{\hbar^2}{2}(3\,n\,\pi^2)^{2/3}\left(\frac{1}{m_{\mathrm{e}}^*} + \frac{1}{m_{\mathrm{h}}^*}\right), \tag{2.17}$$

where $\hbar$ is the reduced Planck's constant ($\hbar = \mathrm{h}/2\pi$) and m_{h}^* is the effective mass of holes.

The band gap of a material can be determined from a measurement of the absorption coefficient vs. wavelength. If the bottom of the conduction band and the top of the valence band are assumed to have a parabolic shape, the absorption coefficient α can be expressed as

$$\alpha = \mathrm{const.}\frac{(\mathrm{h}\nu - E_{\mathrm{g}})^m}{\mathrm{h}\nu}. \tag{2.18}$$

Here, m depends on the nature of the optical transition: $m = 1/2$ for a direct band gap, and $m = 2$ for an indirect band gap. From equation (2.18), extrapolation of a plot of $(\alpha \mathrm{h}\nu)^{1/2}$ vs. $\mathrm{h}\nu$ plot gives the indirect band gap, while a plot of $(\alpha \mathrm{h}\nu)^2$ vs. $\mathrm{h}\nu$ yields the direct band gap of the material. Such a plot is called "Tauc plot" [108]. The band gap of ZnO at room temperature is in the range of 3.2 to 3.4 eV (see Table 2.1). However, due to degenerate doping resulting in Burstein-Moss shift the optical band gap can be wider.

Visible and near infrared regions (400-1000 nm): The transmittance of flat ZnO:Al thin films oscillates between 80 and 90 % in this region (see Fig. 2.3(a)). The oscillations are caused by constructive and destructive interference from the thin ZnO:Al films, which have a thickness on the order of the wavelength of the incoming light (around 800 nm). The offset of the interference fringes between the two samples shown in Fig. 2.3 are due to slightly different film thicknesses. When the surface is randomly textured these interference fringes disappear. Towards the lower energy end of the usable solar spectrum the transmittance begins to decrease and the absorptance increases. This absorption is the tail of the free charge carrier absorption peak.

Table 2.1. The fundamental absorption edge in ZnO corresponds to the direct transition from the highest valence band to the lowest conduction band at the Γ-point of the Brillouin zone. The table summarizes data for the band gap E_g at room temperature. Adapted from [51].

Reference		E_g [eV]
Srikant (1998)	[109]	3.24 ... 3.32
Ohtomo (1998)	[110]	3.29
Studenikin (1998)	[111]	3.195 ... 3.370
Paraguay (1999)	[112]	3.28
Meng (2000)	[113]	3.21
Minemoto (2000)	[114]	3.24
Postava (2000)	[115]	3.35 ... 3.44
Santana (2000)	[116]	3.28
Park (2002)	[117]	3.25
Tokumoto (2002)	[118]	3.28
Takeuchi (2003)	[119]	3.28
Chen (2003)	[120]	3.273
Shan (2003)	[121]	3.25 ... 3.28
Misra (2004)	[122]	3.28
Shan (2004)	[123]	3.274
Zhao (2005)	[124]	3.25 ... 3.27

Infrared region (1000-2200 nm): At wavelengths above 1000 nm, the transmittance decreases while first the absorptance and then the reflectance increase (see Fig. 2.3(a)). In this region the dielectric function goes from positive to negative (equation (2.13)). The exact position of this transition and the plasma frequency (equation (2.14)) depend on the charge carrier concentration. Please notice in Fig. 2.3(a) that increasing the carrier concentration shifts the free carrier absorption peak towards shorter wavelengths.

In conclusion, there are both positive and negative effects of doping on the optical transmittance spectra of ZnO. Higher doping increases the optical band gap, which allows more ultraviolet light to be transmitted. On the other hand, the plasma frequency is shifted to higher energy levels, which increases the free charge carrier absorption of longer wavelength visible and near infrared light.

3. Basics of Semiconductor Electrochemistry

Semiconductor electrochemistry is concerned with the interfaces of electric semiconductors and electrolytes. There are a lot of analogies to the semiconductor/vacuum and semiconductor/metal interfaces. However, the language and concepts used in electrochemical literature differ from those used in solid-state physics in some aspects. Therefore, this chapter aims to briefly introduce the concepts used in electrochemistry with special regards to the semiconductor/electrolyte interface and the zinc oxide/electrolyte interface in particular.

3.1. Basic Concepts of Electrochemistry

3.1.1. The Electrochemical Potential

In thermodynamics the chemical potential of a species i is defined as

$$\mu_i = \left(\frac{\partial G}{\partial N_i} \right)_{p,T}, \tag{3.1}$$

where G denotes the Gibbs energy of the phase under consideration, N_i is the number of particles of species i, p is the pressure, and T the temperature. The chemical potential is thus the work required to add a particle of species i to the system under constant pressure and temperature. For charged particles of species i additional work has to be done against the inner potential ϕ and one might rather define an electrochemical potential instead,

$$\tilde{\mu}_i = \left(\frac{\partial G}{\partial N_i} \right)_{p,T} = \mu_i + z_i \, \mathrm{e} \, \phi, \tag{3.2}$$

with z_i being the charge number of species i, and e the elementary charge. For uncharged species the chemical and electrochemical potential are equal.

Electrons in a solid at $T = 0$ occupy the lowest energy level compatible with the Pauli exclusion principle. On the other hand, the highest energy level occupied at zero temperature is the Fermi level E_F. Thus, any electron that is added to the system must occupy the Fermi level and hence $E_\mathrm{F} = \tilde{\mu}_i$ at $T = 0$. At finite temperatures the Fermi level and the electrochemical potential differ by terms in the order of $(\mathrm{k_B}T)^2$ which are usually negligible.

3.1.2. Absolute Electrode Potential

The standard electrode potential E° [125] of an electrochemical reaction is commonly referred to the standard hydrogen electrode (SHE) [126] and the corresponding values have been compiled in tables (*e.g.* [57]). The choice of this reference potential is arbitrary. In other branches of chemistry and physics potentials are commonly referred to an absolute standard such as the vacuum level. Discussing electrochemical processes at semiconducting electrodes requires combination of the Fermi level in the semiconductor band structure and the electrochemical potential of the redox couple onto a common energy scale. This is of particular importance because the band bending at the semiconductor surface and the position of the band edges in relation to the redox system are largely determining the electrochemical behavior of the interface. Fig. 3.1 shows the Fermi energy scale using the vacuum level as a reference and the electrochemical scale using the standard hydrogen electrode (SHE), *i.e.* the redox potential of the H_2/H^+ couple, as a reference. Note that more positive energies on the Fermi scale correspond to more negative potentials on the electrochemical scale and *vice versa*.

For a metal or semiconductor, the negative of the work function gives the position of the Fermi level with respect to the vacuum level. Likewise, the negative of the work function of an electrochemical reaction is referred to as the Fermi level of this reaction (see paragraph 3.1.1). Thus, Fermi level and electrochemical potential are used synonymously in this context. The work function of the SHE (*i.e.* the energy released when an electron from the vacuum level is brought to the potential of the SHE) is estimated to be 4.5 ± 0.2 eV [128, 129]. Thus, the Fermi level (or electrochemical potential) of any electrochemical reaction on the Fermi scale can be obtained by

$$E_\mathrm{F,redox} = \tilde{\mu} = -(4.5\,\mathrm{eV} + \mathrm{e}\,{E^\circ}_\mathrm{redox}), \tag{3.3}$$

with ${E^\circ}_\mathrm{redox}$ being the standard electrode potential of the redox reaction. Using the same scale for both the electrode and the electrolyte the equilibrium condition for

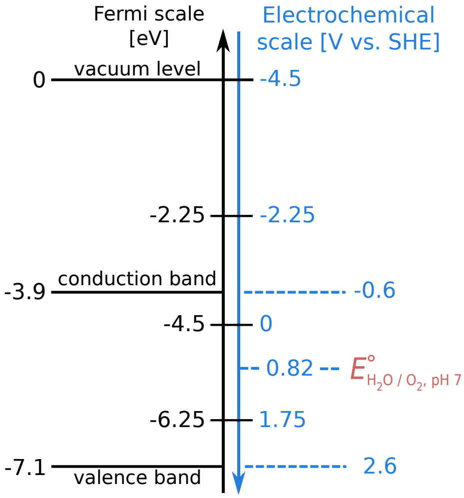

Fig. 3.1. Comparison of the Fermi energy scale and the electrochemical potential vs. SHE. Values of conduction band and valence band energies are taken from [127]. The electrochemical potential of the oxygen evolution reaction was calculated for pH 7.

the redox system becomes simple, $E_{\mathrm{F,electrode}} = E_{\mathrm{F,redox}}$, which makes the concept of a Fermi level for a redox couple quite convenient. However, it should be noted that this terminology does not imply free electrons in the solution which obey Fermi-Dirac statistics [130].

3.2. The Electrochemical Setup

3.2.1. Three-Electrode Configuration

Usually a particular interface between an electrode and an electrolyte is of interest. However, at least two electrodes are necessary to pass a current through the system. Additionally, to determine the potential of the electrode of interest (working electrode) a reference electrode is necessary. Furthermore, no current should flow through the reference electrode in order to maintain a constant potential. Thus, in practice three electrodes are used; the working electrode (WE), a counter electrode (CE) which takes up the current, and a reference electrode (RE). The potential of the WE is measured with respect to that of the RE. To minimize the ohmic potential drop between the WE and the CE the distance between them is kept as small as possible. The CE should be aligned plane-parallel, to the working electrode to avoid inhomogeneous current distribution, and of sufficient size such that it is not limiting the total current. An electrochemical cell in a three-electrode configuration is depicted schematically in Fig. 3.2. What is actually measured as electrode potential is the difference between the electrochemical potentials of the redox couple and of the RE. The Ag|AgCl reference electrode possesses a standard potential of $E^{\circ} = 0.23$ V vs. SHE and is used throughout this work. Further details about the used electrochemical setup can be found in section A.3.

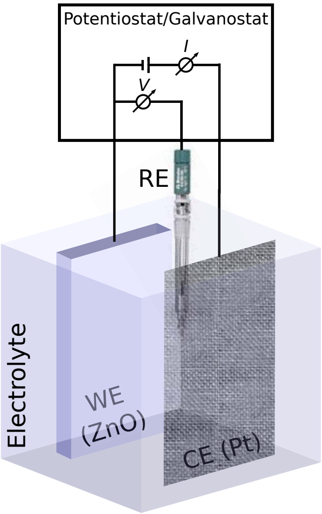

Fig. 3.2. Schematic illustration of an electrochemical cell in a three-electrode configuration controlled by a potentiostat or galvanostat, respectively. The potential of the working electrode (WE) is sensed against the stable reference electrode (RE) potential. Current transport takes place only between working electrode and counter counter electrode (CE).

3.3. The ZnO/Electrolyte Interface

Electrochemical investigations on zinc oxide were initially triggered by corrosion studies of zinc electrodes which regularly exhibit passive films formed in various electrolytes. These passive films show several semiconducting properties of zinc oxide which were found to play an important role in the corrosion behavior of zinc [131]. Since the early years of semiconductor electrochemistry zinc oxide is one of the most frequently used materials in studies on semiconductor electrochemical and photoelectrochemical phenomena. Hence, a large portion of the early understanding of semiconductor electrochemistry was actually obtained from these studies [132]. For comprehensive text books on semiconductor electrochemistry the reader is referred to Ref. [133–135].

As far as possible all processes introduced in this section will be discussed directly on the example of the zinc oxide/electrolyte interface. However, interpretations equally apply for other n-type semiconductors. Furthermore, considerations are valid for p-type semiconductors as well, albeit, with due regard to the acceptor state density N_A instead of the donor state density N_D.

3.3.1. Charge and potential distribution

Upon immersion of a zinc oxide electrode in an aqueous solution, protons, hydroxide ions and other ions adsorb at the surface. Due to the polarity of the zinc oxide crystal hydroxide ions are attracted to the zinc sites and protons are attracted to the oxygen surface sites. A dynamic equilibrium will establish, which can be described by protonation and deprotonation reactions,

$$\mathrm{Zn{-}OH^{+}} \rightleftharpoons \mathrm{ZnO} + \mathrm{H_{aq}}^{+} \tag{3.4}$$

$$\mathrm{Zn{-}OH^{+}} + \mathrm{H_{aq}}^{+} \rightleftharpoons \mathrm{Zn{-}OH_2}^{2+}. \tag{3.5}$$

The equilibrium of these reactions depends on the pH of the solution and the Brønsted acidity of the surface [67]. Thus the net charge adsorbed at the surface is determined by these conditions. The pH at which the net adsorbed charge is zero is called the point of zero charge (PZC) of the semiconductor [127, 136]. Main determinants for the PZC are impurities in the zinc oxide and the nature of the electrolyte. Further factors are discussed in Ref. [137].

Specifically adsorbed ions and electrons trapped in surface states lead to a surface charge. The counter charge is provided by ionized donors in the semiconductor and an accumulation of oppositely charged ions in the solution. The dipole moment of water causes the ions in solution to be surrounded by a solvation shell of water molecules which prevents them from approaching the surface closer than a few Å.

The region between the specifically adsorbed ions and the closest ions in solution is called Helmholtz layer. The potential drop V_H across the Helmholtz layer is pH dependent according to

$$V_\mathrm{H} = \frac{2.3\,\mathrm{k_B}\,T}{\mathrm{e}}\,(PZC - p\mathrm{H})\,. \tag{3.6}$$

The formed double layer acts as a parallel plate capacitor with a typical capacitance C_H of $10 - 20\,\mathrm{\mu F\,cm^{-2}}$ [138]. According to equation (3.6) V_H changes with $2.3\,\mathrm{k_B}\,T/\mathrm{e} = -59\,\mathrm{mV}$ per pH unit at 25 °C. At sufficiently high electrolyte concentrations as used in this work ($\geq 0.1\,\mathrm{M}$) the surface charge is completely compensated within the outer Helmholtz layer. For low electrolyte concentrations the charges are distributed over a much wider diffuse layer, the Guoy layer [135].

An energy diagram of the semiconductor/electrolyte interface is illustrated in Fig. 3.3. When no excess charge is present in the semiconductor and consequently there is no electric field and the energy bands are flat. This situation is depicted in Fig. 3.3(a). The electrode potential under this conditions is called flatband potential E_fb. It is a useful quantity as it is experimentally accessible and connects the electrochemical measurements to the electric bulk properties of the semiconductor. The flatband potential of a semiconductor is found to be quantitatively related to its electron affinity [127].

When a zinc oxide electrode is brought into contact with a solution containing a redox couple, the Fermi levels equalize via redistribution of charges at the interface. Electrons are transferred into the solution leaving behind a positive space charge region (depletion layer) where uncompensated immobile ionized donors are present. This is depicted in Fig. 3.3(b). The width of the space charge layer W depends on the donor density N_D and the potential drop across the space charge region φ_sc [67],

$$W = \sqrt{\frac{2\,\varepsilon_0\,\varepsilon_\mathrm{r}}{\mathrm{e}\,N_\mathrm{D}}\left(\varphi_\mathrm{sc} - \frac{\mathrm{k_B}T}{\mathrm{e}}\right)}. \tag{3.7}$$

Here, ε_0, ε_r, e, $\mathrm{k_B}$ and T are the permittivity of free space, the relative dielectric constant of the semiconductor, the elementary charge, the Boltzmann constant and the temperature. For typical carrier concentrations of the zinc oxide used in this work ($N_\mathrm{D} \approx 10^{21}\,\mathrm{cm^{-3}}$) the space charge layer extends typically 0.1 nm - 1 nm into the zinc oxide. For lower doping concentrations W increases up to several hundred nanometers [128]. The positions of the band edges in contact to the electrolyte are,

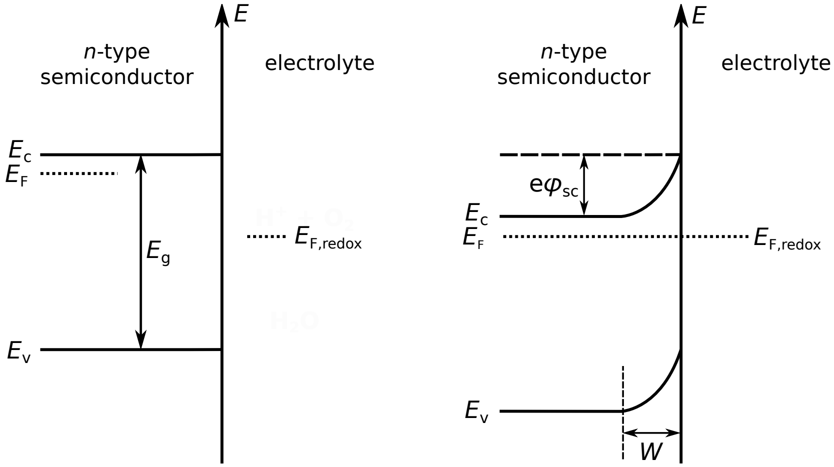

(a) non-equilibrium (b) equilibrium

Fig. 3.3. Schematic illustration of a semiconductor/electrolyte interface. The energy band model is depicted for an n-type semiconductor with band gap E_g into a solution containing a redox couple with the Fermi level $E_{F,redox}$. (a) Band levels before contact between semiconductor and electrolyte. (b) Band diagram for the case in which the semiconductor is in equilibrium with the electrolyte ($E_F = E_{F,\text{ redox}}$). The electron transfer during equilibration of the Fermi energies shifts the band positions in the semiconductor bulk downwards. As a consequence a space charge layer with thickness W is established over which an energy drop $e\varphi_{sc}$ occurs. The space charge in the semiconductor is balanced by am oppositely charged layer in the electrolyte (Helmholtz layer) of thickness d_H.

in good approximation, not altered as the energy levels inside the semiconductor shift [139].

The electrode potential of a semiconductor can be altered by an external power source. Thereby the band bending is changed. Upon application of a reverse bias (anodic potential in case of an n-type semiconductor) in the dark the band bending is increased. Usually almost no current flow is observed in this potential regime because the semiconductor surface is depleted of majority charge carriers and minority charge carrier concentrations are negligible in highly doped semiconductors.

To determine the flat band potential and the charge carrier concentration of a semiconductor in contact with a metal or an electrolyte, impedance spectroscopy at varying bias potential can be used. The method is called Mott-Schottky analysis and utilizes the capacitance of a Schottky junction in reverse bias. It exploits the charge separation in junctions where one side has a much higher carrier concentration than the other. This condition is met, *e.g.*, in semiconductor/metal junctions and semiconductor/electrolyte junctions. The depletion layer in an n-type semiconductor/electrolyte junction is usually completely contained in the semiconductor. The charge separation across the depletion layer creates an associated capacitance. When a reverse bias is applied to the junction (anodic potential at the semiconductor) the depletion width will extend further in the semiconductor as electrons are removed from the semiconductor. Thus, the locally fixed positive charge of the doping ions in the growing space charge layer results in a potential dependent interface capacitance

$$C = A\,\frac{dQ}{dE} = A\,\mathrm{e}\,N_\mathrm{D}\,\frac{dW}{dE}. \tag{3.8}$$

Here, dQ is the positive fixed charge in the depletion layer during application of the bias potential dE, A is the area of the junction, e is the elementary charge, N_D is the carrier concentration, and dW is the change in the space charge layer width. By inserting the expression from equation (3.7) for the space charge layer width and expressing the relationship as C^{-2} vs. E, a linear function with respect to the applied potential E is obtained,

$$\frac{1}{C^2} = \frac{2}{\mathrm{e}\varepsilon_0\varepsilon_\mathrm{r}N_\mathrm{D}A^2}\left(E - E_\mathrm{fb} - \frac{\mathrm{k_B}T}{\mathrm{e}}\right). \tag{3.9}$$

Here, C is the capacitance, ε_0 is the permittivity of free space, ε_r is the relative dielectric constant, A is area of the contact, k_B is the Boltzmann constant, and T is the absolute temperature. The band bending in the space charge layer accounts for

$$\mathrm{e}\,\varphi_\mathrm{sc} = E - E_\mathrm{fb}. \tag{3.10}$$

In practice, the junction capacitance is measured imposing an alternating potential (of approximately 10 mV) over a DC potential and determining the impedance. The capacitance can than be found using impedance-capacitance relationships. According to equation (3.9) a plot of C^{-2} vs. E is linear. The intersection with the potential axis yields the value of E_fb and the slope can be used to determine N_D. Typical values of the E_fb for moderately doped ZnO electrodes ($N_\mathrm{D} \approx 10^{16} - 10^{18}\,\mathrm{cm}^{-3}$) are in the range of -0.2 to -0.82 V vs. SHE [140–143]. It is determined by the variation of the bulk Fermi level and the interaction of surface states with the electrolyte. Due to the shift of the potential drop V_{H} across the Helmholtz layer with pH according to equation (3.6), the flatband potential also varies 59 mV per unit pH [140,144,145]. Furthermore, E_{fb} depends on the surface conditions such as crystal orientation [145] or pretreatments in acidic or alkaline solutens [143]. This can be explained by differing charge densities at the ZnO/electrolyte interface due to a variation in the amount of Zn and O atoms at the surface and consequent changes in the adsorbed excess charge.

The frequency used for measuring the capacitance has been found to have various effects on the value of E_{fb} as determined by Mott-Schottky analysis. Dewald reported that Mott-Schottky analysis in 1 M KCl at pH 8.5 is independent of the frequency in the range from 0.1 to 10 kHz [143]. In contrast, Vanden Berghe *et al.* found a frequency dependence of 70 mV over approximately the same frequency range in 1 M KCl containing 0.5 M $[\mathrm{Fe(CN)}_6]^{3-}$ [142]. Surface states, possessing energies within the band gap, are often considered responsible for the frequency dependence. This is in accordance with the observation of a very strong frequency dependence for polycrystalline zinc oxide thin films [146] which exhibit a relatively large amount of structural disorder and defect states.

3.3.2. Charge Transfer

The electrode kinetics of zinc oxide have been extensively investigated by Morrison and Freund [141,147–149], and Pettinger *et al.* [145,150]. The charge transfer is mainly governed by the charge carrier density in the electrode. The anodic current in the dark is very low ($\sim$ nA cm^{-2}). Breakdown of the blocking behavior is found to occur at high anodic potentials [145] depending on the doping concentration. Fig. 3.4 illustrates possible charge transfer processes at the zinc oxide/electrolyte interface. It contains the energies of reduced and oxidized redox species with a Gaussian shaped distribution as a function of fluctuations in the electric field due to the movement of solvent and species themselves [151]. The identical shape and integral of these distribution functions for both oxidation states are assumed for simplicity in these theoretical considerations but are far more complex in real systems [128], especially due to different activities of these species as the main determinant for the integral.

Two main transfer processes are illustrated in the Fig. 3.4 [133]. The first one is the tunneling of electrons of equal energy level through an energy barrier caused by the space charge region and the second is the direct transfer at the band edges. It is

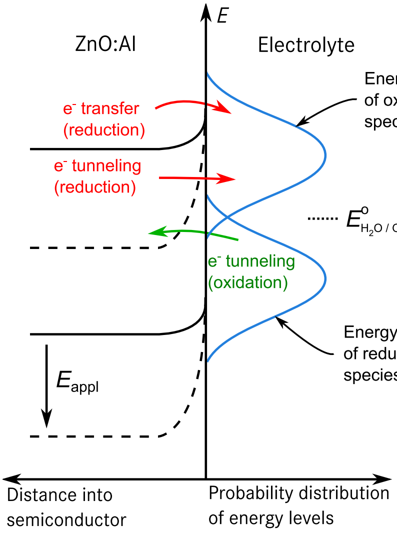

Fig. 3.4. Schematic illustration of electron transfer processes between a zinc oxide electrode and oxygen in the absence and presence of anodic polarization (E_{appl}). A symmetrical density of states distribution of oxidized and reduced form of the redox system is assumed for simplicity. Charge transfer is possible when electrons in occupied states in either the zinc oxide or the electrolyte find empty states in the other phase and no energy barrier is present or the barrier is sufficiently narrow to allow for tunneling.

evident from Fig. 3.4 that an external anodic polarization E_{appl} causes the energy levels in the semiconductor bulk to shift downward and therefore decreases the charge carrier density of majority carriers in the region of charge transfer to the oxidized redox species.

In case of anodic polarization (which manifest in a downwards shift of the energy levels in the semiconductor in Fig. 3.4), the density of electrons in the conduction band is decreased, first allowing electron uptake by tunneling from the reduced redox species. This tunneling process depends strongly on the redox potential of the present redox species [150]. Ultimately, when the band bending exceeds the band gap, band to band tunneling from the valence band into the conduction band can occur leading to an increase of holes in the valence band and a direct hole transfer causing oxidation of the redox system. However, a comparably large overpotential is required, called the blocking region. Due to the dependence of the band bending and the space charge layer width on the charge carrier concentration, this blocking region is strongly affected by the dopant and defect density in the electrode [145]. The potential at anodic breakdown generally decreases with increasing doping concentration.

3.4. Stability of ZnO in Aqueous Electrolytes

The most decisive factor for the stability of both crystalline and polycrystalline zinc oxide in aqueous media is the *p*H value. The Pourbaix diagram of the zinc-water system gives a fundamental illustration of this dependency derived from chemical equilibria [152]. It is depicted in Fig. 3.5 and describes the relative dominance of a species in a particular potential-*p*H regime. Reaction (a) shows the onset potential for hydrogen evolution (HER, reaction (3.11)) and (b) the reversible potential of the oxygen evolution reaction (OER, reaction (3.12)),

$$2\ H_2O + 2\ e^- \rightleftharpoons H_2 + 2\ OH^-, \tag{3.11}$$

$$2\ H_2O \rightleftharpoons O_2 + 4\ H^+ + 4\ e^-. \tag{3.12}$$

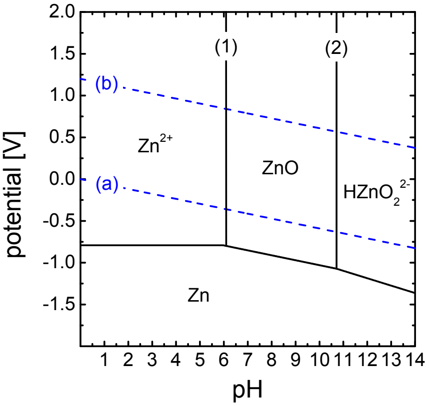

Fig. 3.5. Pourbaix diagram of the zinc-water system. Note that the potentials are given vs. the standard hydrogen electrode (SHE). (a) shows the onset potential of HER and (b) of OER. Zinc oxide is thermodynamically stable in a *p*H range between approximately 6 and 11 and can be dissolved in both acidic and alkaline solutions due to its amphoteric character. Adapted from [152].

A thermodynamically stable window for zinc oxide in the pH range between approximately 6 and 11 [152]. At low and high pH values zinc oxide dissolves. Both acidic (1) and alkaline dissolution (2) are dependent on the zinc concentration in the solution. For higher zinc concentration the zinc oxide precipitation starts at lower pH values because the solubility product is reached earlier.

At neutral pH zinc oxide is usually stable at anodic polarization. However, at high anodic polarization zinc oxide can dissolve in the dark when the blocking behavior of the zinc oxide/electrolyte junction breaks down as was mentioned above. This is usually accompanied by water oxidation. Furthermore, zinc oxide decomposes under illumination with light of energy $\mathrm{h}\nu > E_\mathrm{g}$, according to

$$2\ \mathrm{ZnO} + 4\ \mathrm{h}\nu \longrightarrow 2\ \mathrm{Zn}^{2+} + \mathrm{O}_2 + 4\ \mathrm{e}^- \cdot \qquad (3.13)$$

Chemical dissolution and photo-anodic decomposition of zinc oxide singe crystals were extensively investigated by Gerischer and co-workers [153–155]. Cathodic decomposition is not observed, however, at high cathodic potentials reduction to metallic zinc occurs which can subsequently be stripped in an anodic potential sweep [146].

4. Electrochemical Deposition of Zinc Oxide

This chapter focuses on the growth of zinc oxide using electrochemical deposition. An introduction to the field is given in section 4.1 comprising a review of the literature. Section 4.2 provides information on the experimental conditions used and presents results of zinc oxide samples deposited from solutions using either nitrate (paragraph 4.2.1) or molecular oxygen (paragraph 4.2.2) as precursors. The impact of the potential, current density, temperature, and the Zn^{2+} *concentration is investigated. The use of sputter-deposited indium tin oxide and aluminum-doped zinc oxide seed layers as substrates for growth is shown to trigger different growth modes for the electrochemical deposition. Furthermore, substituting the anion species of the supporting electrolyte with perchlorate is found to lead to local corrosion, competing with the electrochemical deposition process. Finally, the results are concluded in section 4.3 and some ideas for further improvements are suggested.*

4.1. Introduction

The electrochemical deposition (ECD) of zinc oxide was first reported in 1996 independently by Peulon and Lincot [156] and by Izaki and Ohmi [42, 157]. Since these pioneering works, ECD of zinc oxide gained increasing attention due to its simplicity, low cost, and the good crystalline quality of the deposited material. Furthermore, ECD allows for the deposition of nanostructured topographies such as nanorods [158–160], nanotubes [161–163], and nanoporous films [164–168]. A review of the electrodeposition of zinc oxide with a focus on the formation of porous structures can be found in Ref. [166].

The principle of ECD of zinc oxide is based on the controlled increase of the interfacial pH by electrochemical formation of OH^-. This can be done by the reduction of a suitable precursor such as molecular oxygen [156, 169–171], nitrate ions [42, 172, 173], or hydrogen peroxide [174, 175] according to

$$\begin{aligned} {}^1\!/\!_2\,O_2 + H_2O + 2\ e^- &\longrightarrow 2\ OH^-, & (4.1)\\ NO_3{}^- + H_2O + 2\ e^- &\longrightarrow NO_2{}^- + 2\ OH^-,\ \text{and} & (4.2)\\ H_2O_2 + 2\ e^- &\longrightarrow 2\ OH^-,\ \text{respectively.} & (4.3) \end{aligned}$$

Subsequently, the hydroxyl ions precipitate with Zn^{2+} ions to form zinc hydroxide [176]

$$Zn^{2+} + 2\ OH^- \longrightarrow Zn(OH)_2, \tag{4.4}$$

which can react to ZnO if the temperature of the solution is sufficient,

$$Zn(OH)_2 \longrightarrow ZnO + H_2O\ \cdot \tag{4.5}$$

Therefore, ECD of ZnO is usually performed in the temperature range between 60 and 90 °C [173, 177, 178]. Several studies on the temperature dependence of electrochemical ZnO deposition can be found in the literature [173, 177–181].

The reduction of nitrate ions is kinetically slow as compared to the reduction of O_2 and H_2O_2. They are usually inert and can be reduced only in the presence of certain metal ions [182, 183]. For the ECD of zinc oxide the Zn^{2+} ions serve as catalysts for the reduction of $NO_3{}^-$ and the growth rate in nitrate solutions is influenced by the concentration of zinc cations [178, 184, 185]. This makes the deposition of ZnO films from nitrate solutions less reproducible compared to the deposition from oxygen saturated chloride solutions. However, even the deposition of compact films was achieved, which is experimentally challenging because zinc oxide tends to grow in columnar nanostructures [184, 186–190]. Also the preparation of inverse opals using polystyrene spheres as templates in nitrate solutions was reported [168, 191–194].

Even though the standard electrode potentials for the reduction of oxygen precursors with respect to the Ag|AgCl reference electrode used in this work are -0.212 V for reaction (4.1) [57], +0.179 V for reaction (4.2) [57], and +0.718 V for reaction (4.3) [174], respectively, the cathodic electrodeposition typically only starts at potentials below -0.6 V due to high overpotentials. On the other hand, a lower limit of the potential is set by the reduction of zinc ions to metallic zinc, which typically starts at approximately -1.1 V vs. Ag|AgCl.

A broad range of materials was used as a substrate. Other than metal substrates such as Zn [195], Au [158, 196, 197], and Pt [176] also semiconducting substrates such as Si [198–201], GaN [169, 171, 202], Cu_2O [203] served as a substrate. However, most studies were performed on transparent conductive oxide films on glass, *e.g.* tin-doped indium oxide (ITO) [188, 201, 204–208] or flourine-doped tin oxide (FTO) [158, 187, 209, 210]. Heteroepitaxial growth on aluminum-doped zinc oxide thin films was also studied [159, 211–213].

Even though the vast majority of reported studies uses aqueous solutions, ECD of ZnO was also successfully conducted in non-aqueous solutions such as dimethyl sulfoxide [214–218], propylene carbonate [219, 220], or ionic liquids [221] allowing to perform depositions at higher temperatures. However, films deposited in aqueous solutions are, so far, of better crystalline quality.

Besides intrinsic doping via oxygen deficiencies or zinc interstitials (see section 2.2.2.1) which is present in most electrochemically deposited zinc oxide films, extrinsic doping by incorporation of B [222,223], Al [204,210,224–227], In [204,225,228] has been achieved. Furthermore, doping with Co [198], Cu [229] and Cl [230, 231] was reported.

The main focus was the application of the deposited thin films as transparent front contacts in CIGS and CIS thin-film solar cells [214, 225, 227, 232–234]. However, electrodeposited zinc oxide in its various forms was further used in Si thin-film solar cells [224, 235, 236], dye sensitized solar cells [237–241], and photo-detectors based on ZnO nanowires/p-Si heterojunctions [242].

Due to the high chemical reactivity of ZnO and the reversibility of the overall reaction,

$$\mathrm{Zn^{2+}} + 2\ \mathrm{OH^-} \rightleftharpoons \mathrm{ZnO} + \mathrm{H_2O}, \tag{4.6}$$

dissolution and recrystallization reactions take place during electrochemical deposition in aqueous media which allows for the growth of highly ordered arrays of crystals. Typically, a faster crystal growth on the polar (0001) face is observed as compared to the non-polar faces. This anisotropy in the growth rate is known also for other deposition methods [243]. In case of deposition from aqueous solutions it is subscribed to differing dissolution rates of the different zinc oxide faces. During growth, deposition and dissolution compete with each other and a higher dissolution rate results in a lower net growth rate. Gerischer *et al.* [153] showed that the dissolution rate of the zinc-terminated (0001) face is lower than those of the oxygen-terminated $(000\bar{1})$ and the non-polar (0010) faces using the method described in chapter 5. When other anion species such as sulfate, chloride, nitrate, perchlorate, and acetate are added, the dissolution rate is also affected (see chapter 6) [153]. This can be used to control the morphology of the deposited zinc oxide [244, 245].

By varying the concentration of the reactants and the supporting electrolyte in the deposition bath the deposition of nanowires of differing width and length is feasible [158, 178, 185, 224, 245–248]. The diameter of electrochemically deposited nanowires was found to increase with increasing concentration of zinc nitrate in the solution. In case of ECD from oxygen-saturated zinc chloride solutions the chloride concentration was identified as a major determinant for the nanowire diameter [245, 249]. This was attributed to preferred adsorption of Cl^- ions on the polar (0001) face, preventing fast growth in this direction.

4.2. Results and Discussion

The investigations presented in this chapter represent first efforts to utilize solution based deposition of zinc oxide at the IEK-5. Therefore, characterization is restricted to a qualitative analysis of the deposition process and the deposited material. Morphological properties were mainly studied using electron microscopy which allows to observe dependencies on deposition parameters such as the deposition potential, temperature, and concentrations in the electrolyte. The focus was set on the initial nucleation phase. However, first results on optical properties of a closed zinc oxide film are presented in paragraph 4.2.2.3.

Cathodic deposition was performed using reduction of both nitrate (section 4.2.1) and molecular oxygen (section 4.2.2) to provide a suitable interfacial pH at the cathode for precipitation of zinc oxide.

4.2.1. Electrochemical Deposition from Zinc Nitrate Solutions

Electrochemical deposition using nitrate reduction to increase the interfacial pH at the electrode via reaction (4.2) was performed under potentiostatic and galvanostatic control. In order to find a suitable process window and to learn about the dependencies of the deposits on the process parameters, potential, current density, Zn^{2+} concentration and temperature were varied.

4.2.1.1. Experimental Conditions

As substrates room temperature sputter-deposited ITO thin films were used which were approximately 100 nm thick and provided a sheet resistance of $R_{\mathrm{sh}} < 100\,\Omega$. The electrochemical depositions were conducted on 2.5 cm × 5 cm pieces contacted using a metallic clamp. The actual surface area exposed to the deposition bath was determined after deposition in order to calculate the correct current density. It has to be noted that for elevated temperatures evaporation of the electrolyte solution cannot be prevented and, even though some effort was undertaken to isolate the contact, condensation of water on the contact remained a problem. Thus, a temperature of $T = 50\,°\mathrm{C}$ was initially chosen representing a trade-off between maintaining sufficient temperatures to decompose the initially formed $Zn(OH)_2$ to ZnO via reaction 4.5 with a reasonable rate on the one hand [177], and preventing wetting of the contact on the other hand. All depositions were conducted in a conventional three-electrode setup (see section 3.2.1) using a Ag|AgCl|3 M KCl reference electrode. The *p*H value of the initial electrolytes was approximately 5. During all depositions the solution was stirred by a magnetic stirrer at a constant rotation speed of 400 rpm. All samples were carefully cleaned in deionized water before characterization. Scanning electron microscopy (SEM) images were recorded with a tilt of 50° to the surface normal.

4.2.1.2. Zinc Concentration and Temperature

Linear sweep voltammetry was used to determine a suitable potential range for ECD of ZnO with the used setup. Measurements with varied Zn^{2+} concentrations are depicted in Fig. 4.1. The voltammetry was conducted starting at $E = 0$ in cathodic direction with a scan rate of $\nu = 30\,\mathrm{mV\,s^{-1}}$. The cathodic reduction peak observed at a potential of approximately $E = -0.8\,\mathrm{V}$ is ascribed to nitrate reduction. At more negative potentials the current density increases further, which is due to hydrogen evolution (water reduction) and finally, reduction of Zn^{2+} from the solution to metallic zinc. Thus, the potential range between -0.6 V and -1.0 V was determined to be suitable for zinc oxide deposition from nitrate based aqueous solutions.

The cathodic current increased with increasing Zn^{2+} concentration even though the zinc oxide formation via reactions (4.4) and (4.5) is a purely chemical process and not comprising any electron transfer which could be observed as a current density in voltammetric measurements. Note that the initial nitrate concentration was the same for each measurement. This was provided by adding KNO_3^- as a supporting salt such that the total NO_3^- concentration was 0.1 M. Therefore, the increase of the

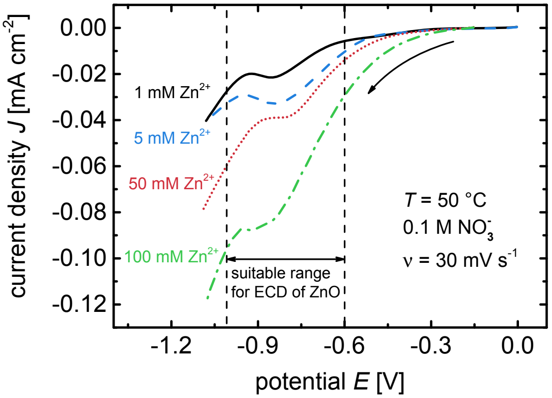

Fig. 4.1. Linear sweep voltammograms of ITO electrodes in aqueous zinc nitrate solutions recorded with a scan rate of $\nu = 30 \mathrm{mV\,s^{-1}}$ in cathodic direction. The solutions contained 0.1 M NO_3^- and differing Zn^{2+} concentrations in the range between 1 mM and 100 mM.The temperature was maintained at $T = 50$°C for all scans. The potential is referred to Ag|AgCl|3 M KCl.

reduction peak suggests a catalytic effect of the zinc ions adsorbed at the working electrode surface on the reduction of nitrate [184]. A similar catalytic effect of other metals on nitrate reduction was reported by Cox *et al.* [182]. Thus, the interface *p*H at the working electrode may depend crucially on the zinc ion concentration which would certainly affect the deposition rate and the composition of the deposits.

Fig. 4.2 depicts scanning electron micrographs of ZnO deposited from solutions with constant nitrate concentrations of 0.1 M and varied zinc ion concentrations. Depositions were conducted at a constant potential of $E = -0.87$ eV for $t = 2500$ s at a temperature of $T = 50$ °C with stirring. It is evident that not only the amount of deposited material, *i.e.* the growth rate, differs, but also its structure. For a zinc concentration as low as 1 mM (see Fig. 4.2a) comparably few crystallization nuclei are formed. Moreover, the formed crystallites vary strongly in size. For Zn^{2+} concentrations in the range between 5 mM and 25 mM a more uniform surface coverage of the electrode was observed (see Fig. 4.2b). Higher zinc concentrations apparently promote more porous and irregular growth. A typical example which was deposited from a 50 mM Zn^{2+} containing nitrate solution is depicted in Fig. 4.2c. Generally, crystalline growth seems to occur preferentially for low zinc concentrations, while higher zinc concentrations appear to promote the formation of flake-like deposits covering the surface. The transition was found to be at approximately 25 mM zinc concentration. The thin flaky deposits might consist of zinc hydroxide which is not efficiently transformed into ZnO at the provided temperature.

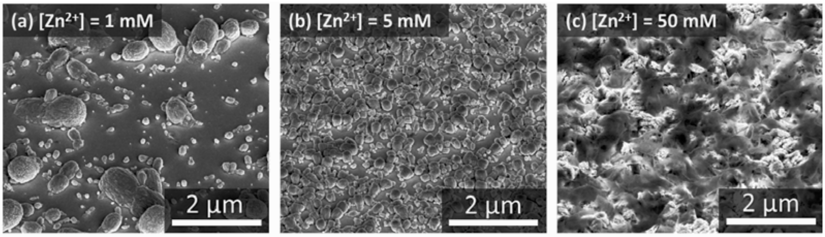

Fig. 4.2. SEM images of zinc oxide deposited on ITO substrates by means of potentiostatically controlled ECD from an aqueous zinc nitrate bath at a potential of $E = -0.87$ V vs. Ag|AgCl|3 M KCl. The nitrate concentration was $[NO_3^-] = 0.1$ M and the solution was stirred by means of a magnetic stirrer with a rotation speed of 400 rpm. The bath temperature was maintained at $T = 50$ °C. The zinc concentrations in the solution were 1 mM (a), 5 mM (b), and 50 mM (c).

This behavior can also be observed in SEM images of zinc oxide deposited by galvanostatic ECD at different temperatures and zinc concentrations (Fig. 4.3). The depositions were conducted under galvanostatic control at a current density of $j = -0.06\ \mathrm{mA\,cm^{-2}}$. The samples depicted in Fig. 4.3a and Fig. 4.3b were prepared under identical conditions except for the bath temperature which was maintained at $T = 50$ °C and $T = 70$ °C, respectively. For the used conditions the temperature obviously played a crucial role for the crystallization process. At 50 °C indeed small crystallites are formed however of irregular shape and again covered with a thin layer of flaky material. In contrast, the deposition at 70 °C promoted the growth of crystallites with a regular hexagonal shape. However, for high zinc concentrations, a temperature of 70 °C is apparently still insufficient to grow crystalline zinc oxide, as depicted in Fig. 4.3c on the example of 100 mM zinc concentration.

4.2.1.3. Current density

The effect of the current density during deposition is discussed in the example of two samples deposited under galvanostatic control at $j = -0.06\ \mathrm{mA\,cm^{-2}}$ and $j = -0.12\ \mathrm{mA\,cm^{-2}}$, respectively. Each deposition was stopped when a charge of $240\ \mathrm{mC\,cm^{-2}}$ was exchanged at the electrode. Thus, assuming similar faradaic

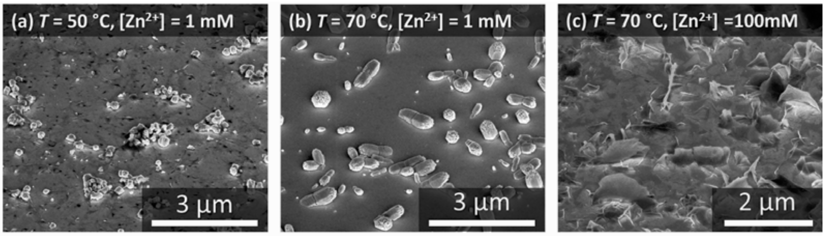

Fig. 4.3. SEM images of zinc oxide deposited on ITO substrates by means ECD under galvanostatic control from an aqueous zinc nitrate bath at a current density of $j = -0.06\,\mathrm{mA\,cm^{-2}}$. The solutions were stirred by means of a magnetic stirrer with a rotation speed of 400 rpm and contained 0.1 M nitrate. Temperature and zinc concentration were varied: (a) $T = 50\,°\mathrm{C}$, $[\mathrm{Zn}^{2+}] = 1\,\mathrm{mM}$, (b) $T = 70\,°\mathrm{C}$, $[\mathrm{Zn}^{2+}] = 1\,\mathrm{mM}$, (c) $T = 70\,°\mathrm{C}$, $[\mathrm{Zn}^{2+}] = 0.1\,\mathrm{M}$.

efficiencies, the amount of deposited zinc oxide is expected to be the same for both samples. Fig. 4.4 compares the potential transients of the two deposition processes and Fig. 4.5 depicts SEM images of the corresponding samples. A higher current density results in an increased initial deposition potential. However, the potentials are approaching each other in the course of the deposition and finally show similar values for both depositions. It is apparent from the SEM images in Fig. 4.5 that the sample deposited at higher cathodic current density, which is depicted in Fig. 4.5b, exhibits more but smaller crystallites than the sample deposited at smaller cathodic current densities, which is plotted in Fig. 4.5a.

Recalling that the growth of zinc oxide in solution is a dissolution-precipitation process the higher growth rate at higher cathodic current densities might shift the equilibrium between dissolution and recrystallization such that reorientation is less probable. Thus, the density of nucleation centers is higher in this case. In contrast, at lower growth rates the precipitate might have sufficient time to find an energetically more favorable position making the integration in an already present crystal more probable.

4.2.2. Electrochemical Deposition from Chloride and Perchlorate Solutions

Electrochemical deposition of zinc oxide using the reduction of molecular oxygen via reaction (4.1) was performed under potentiostatic control. The impact of chloride and

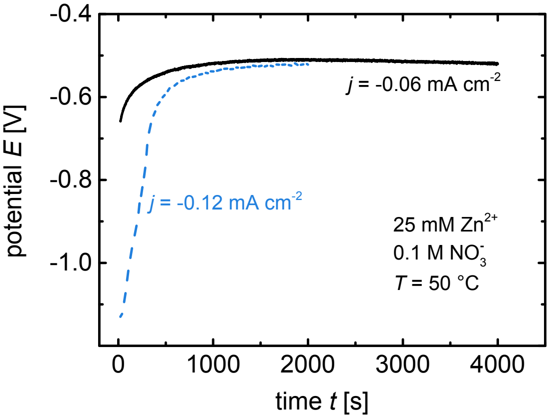

Fig. 4.4. Potential evolution during galvanostatic ECD of zinc oxide on ITO substrates from aqueous zinc nitrate solutions. The ion concentrations were $[NO_3^-] = 0.1\,\text{M}$ and $[Zn^{2+}] = 25\,\text{mM}$ and the bath temperature was maintained at $T = 50\,°C$. A magnetic stirrer with a rotation speed of 400 rpm was used to provide convection. The deposition current density was varied. The potential is referred to Ag|AgCl|3 M KCl.

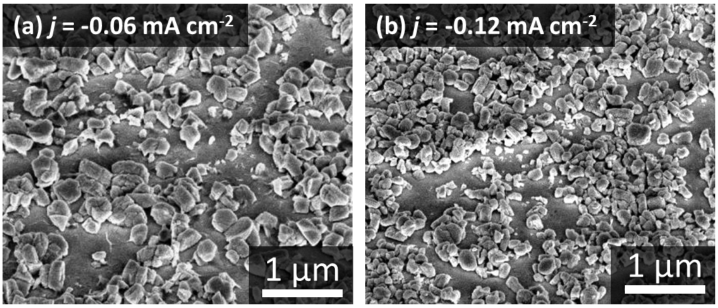

Fig. 4.5. SEM images of zinc oxide deposited on ITO substrates by means ECD under galvanostatic control from an aqueous zinc nitrate bath. The ion concentrations were $[NO_3^-] = 0.1$ M and $[Zn^{2+}] = 25$ mM and the bath temperature was maintained at $T = 50$ °C. The deposition current density was set to (a) $j = -0.06\,\text{mA}\,\text{cm}^{-2}$, and (b) $j = -0.12\,\text{mA}\,\text{cm}^{-2}$, respectively. Stirring was done using a magnetic stirrer with a rotation speed of 400 rpm.

perchlorate on the deposited zinc oxide was studied. Furthermore, the electrochemical deposition on ITO and ZnO:Al substrates was compared.

4.2.2.1. Experimental Conditions

All depositions in this section were carried out at a temperature of $T = 70°\text{C}$ and with stirring at a rotation rate of 400 rpm. The deposition bath contained 1 mM $ZnCl_2$. As a supporting salt, either 0.1 M KCl or 0.1 M $KClO_4$ was used. The depositions were done on sputter-deposited ITO thin films with a thickness of approximately 100 nm and a sheet resistance of $R_{\text{sh}} < 100\,\Omega$ and ZnO:Al thin films with a thickness of approximately 800 nm and a sheet resistance of $R_{\text{sh}} = 3.6\,\Omega$. Samples were cut into 2.5 cm × 5 cm pieces and contacted using a metallic clamp. A three-electrode setup was used featuring a Ag|AgCl|3 M KCl reference electrode to which all potentials are referred. After deposition for $t = 1\,\text{h}$ the samples were carefully rinsed with deionized water.

To start with, again linear sweep voltammetry was used to get an idea of the potential range usable for ECD from O_2-saturated solutions. Two sweeps of an ITO and a ZnO:Al electrode, respectively, measured from $E = 0$ to $E = -1.0$ V with a scan rate of $\nu = 50\,\text{mV}\,\text{s}^{-1}$ in cathodic direction in an aqueous solution containing 0.1 M KCl and 1 mM $ZnCl_2$ are plotted in Fig. 4.6. The solid line represents the behavior of the ITO electrode whereas the dotted line corresponds to the measurement of the ZnO:Al electrode. A cathodic current density is observed for both sweeps, however, the cathodic peak at the ITO electrode starts at approximately -0.6 V whereas the ZnO:Al electrode exhibits a current onset at approximately -0.4 V. This is probably caused by a higher overpotential for the ITO electrode due to a higher sheet resistance or a lower exchange current density increasing the necessary overpotential according to the Butler-Volmer equation.

4.2.2.2. Substrate, Potential, and Supporting Electrolyte

Based on the linear sweep voltammograms depicted in Fig. 4.6 potentials more negative than $E = -0.6$ V were figured suitable for O_2 reduction and the potential for subsequent ECD experiments was varied in three steps between $E = -0.7$ V and $E = -0.9$ V.

The current density and charge density transients during ECD are depicted in Fig. 4.7. Data of depositions on ITO substrates with KCl as a supporting electrolyte

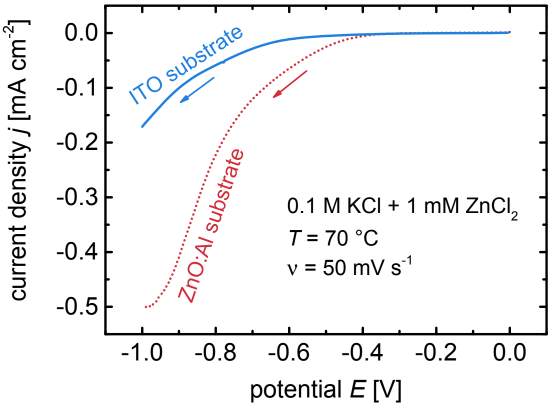

Fig. 4.6. Linear sweep voltammograms of ZnO:Al substrates in aqueous KCl solutions recorded with a scan rate of $\nu = 50\,\mathrm{mV\,s^{-1}}$ in cathodic direction. The solid line represents the measurement of the ITO electrode whereas the dotted line corresponds to the measurement of the ZnO:Al electrode. The temperature was $T = 70\,°\mathrm{C}$. The potential is referred to Ag|AgCl|3 M KCl.

are plotted in Fig. 4.7a and Fig. 4.7b. In the initial phase the cathodic current density was higher for higher applied potentials. However, this dependence does not hold for the whole deposition time. The same applies for the deposition on ITO substrates from O_2-saturated aqueous solutions containing $KClO_4$, plotted in Fig. 4.7c and Fig. 4.7d. However, for the deposition on ZnO:Al substrates, of which the data is depicted in Fig. 4.7e and Fig. 4.7f, a clear increase of the current density with increasing potential is apparent. The irregular behavior of the ITO electrodes might be related to a less homogeneous sputter-deposition and resulting deviations in the sheet resistance in the order of $\pm 30\,\Omega$. However, the deposited structures allow some conclusions to be drawn. SEM pictures of the corresponding samples are depicted in Fig. 4.8. They were recorded with a tilt of 50° to the surface normal. Colored frames are applied corresponding to the colors in Fig. 4.7 to make the assignment easier.

Regarding the deposition on ITO substrates (Fig. 4.8a to Fig. 4.8f), several trends are obvious. Focusing on the deposition on ITO substrates from chloride solutions (Fig. 4.8a to Fig. 4.8c) several trends are obvious. First of all, hexagonal zinc oxide crystals were formed at all potentials applied, indicating high crystallinity. No preferred orientation of the c-axis with respect to the surface normal is evident from the SEM images. In fact, the orientation seems to be random. Approximately the same charge was transferred during the deposition at $E = -0.7\mathrm{V}$ and $E = -0.9\mathrm{V}$

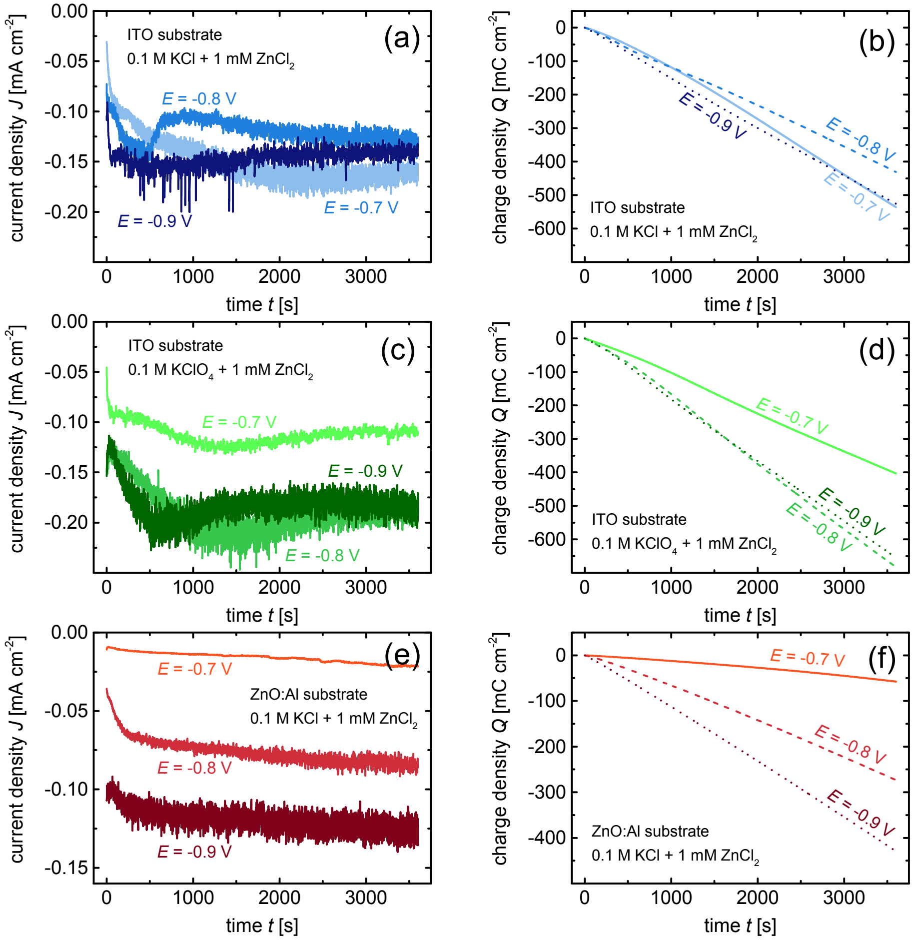

Fig. 4.7. Potentiostatic ECD of ZnO on ITO substrates in an aqueous solution containing 1 mM $ZnCl_2$. Prior to each deposition the solution was saturated with O_2 and during deposition a constant flow of O_2 was bubbled through the solution. The temperature was maintained at $T = 70$ °C and the solution was stirred by means of a magnetic stirrer with a rotation speed of 400 rpm. Depositions were performed at $E = -0.7$ V, $E = -0.8$ V, and $E = -0.9$ V. All potentials are referred to Ag|AgCl|3 M KCl. Two different supporting salts were used. (a) and (b) show current density and charge density transients, respectively, of depositions from solutions with 0.1 M KCl as a supporting salt. (c) and (d) depict current density and charge density transients, respectively, of depositions from solutions with 0.1 M $KClO_4$ as a supporting salt.

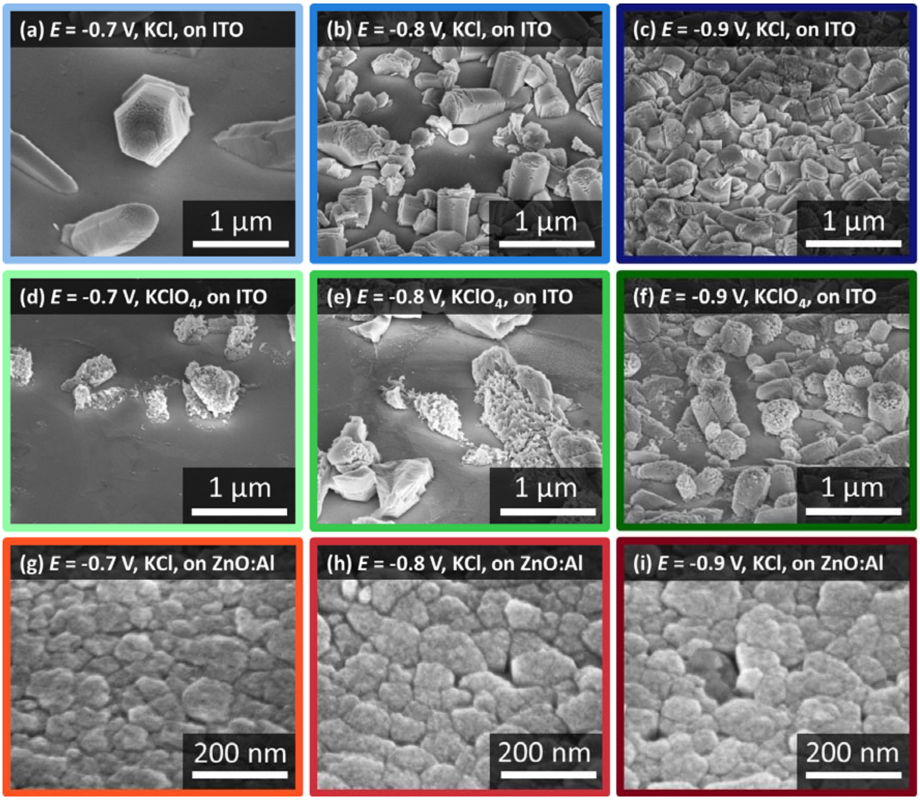

Fig. 4.8. SEM images of zinc oxide deposited on ITO and ZnO:Al substrates, respectively, by means of ECD under potentiostatic control from O_2-saturated aqueous solutions containing 1 mM $ZnCl_2$. The evolution of the current density and the charge transferred at the cathode can be found in Fig. 4.7. The bath temperature was maintained at $T = 70\,°C$ and stirring with a rotation speed of 400 rpm was applied. The deposition bath contained either 0.1 M KCl (a-c, g-i) or $KClO_4$ (d-f), respectively. The applied potentials were adjusted to $E = -0.7$ V (a, d, g), $E = -0.8$ V (b, e, h), and $E = -0.9$ V (c, f, i), respectively. All potentials refer to Ag|AgCl|3 M KCl.

(see Fig. 4.7b) which suggests that approximately the same amount of zinc oxide was deposited in both processes. However, the smaller the applied potential during deposition, the less nucleation seeds formed on the ITO electrode. Thus, the lack of nucleation sites promotes the few crystallites present to grow bigger. To put it the other way around, with increasing cathodic potential the crystallites become smaller but the surface coverage of the electrode with zinc oxide increases due to the formation of more nucleation sites.

This trend was also observed when Cl^- was substituted by ClO_4^- as the anion species in solution (see Fig. 4.8d to Fig. 4.8f). However, the deposits from perchlorate solutions show less defined hexagonal crystallites. And despite the fact that the exchanged charge during deposition in perchlorate solutions was slightly higher than in chlorate based solutions, the SEM images give the impression that less zinc oxide was deposited. Furthermore, perchlorate seems to promote the dissolution of the zinc oxide structures. Especially the polar faces of the crystallites seem to be affected but also the non-polar $(10\bar{1}0)$ and equivalent faces exhibit areas which are apparently strongly etched. SEM images with higher magnification are depicted in Fig. 4.9, showing nanowires grown in Cl^- (Fig. 4.9a) and in ClO_4^- containing solution (Fig. 4.9b), respectively. The nanowire obtained in chloride solution exhibits the typical hexagonal shape of the wurtzite crystal structure whereas the one obtained from perchlorate solution seems to be corroded and rather porous. The influence of various anion species on the dissolution of zinc oxide is discussed in more detail in chapter 6. The perchlorate obviously shifts the equilibrium of the dissolution-precipitation mechanism, defined by reaction (4.6), further to the dissolution side, leading to the observed corrosion of the deposits.

Comparing the zinc oxide structures grown under identical conditions on ITO and ZnO:Al electrodes provide evidence for the central role assigned to the substrate (Fig. 4.8a to Fig. 4.8c and Fig. 4.8g to Fig. 4.8i, respectively). The growth of zinc oxide on ZnO:Al apparently adapts to the polycrystalline structure and orientation of the substrate, which usually exhibits c-axis orientation perpendicular to the surface normal [250]. A hexagonal crystal structure was not observed. Instead, closed layers were formed showing grains of a similar lateral size to those of the substrate. Thus, the ZnO:Al obviously functions as a seed layer for the zinc oxide grown by ECD. The current density increased with increasing applied potential (see Fig. 4.7e), suggesting an increased growth rate. Compared to ECD on ZnO:Al from ClO_4^- containing solutions (not shown here) the films grown in Cl^- solutions are more homogeneous, again indicating a detrimental effect of perchlorate on the crystalline growth of zinc

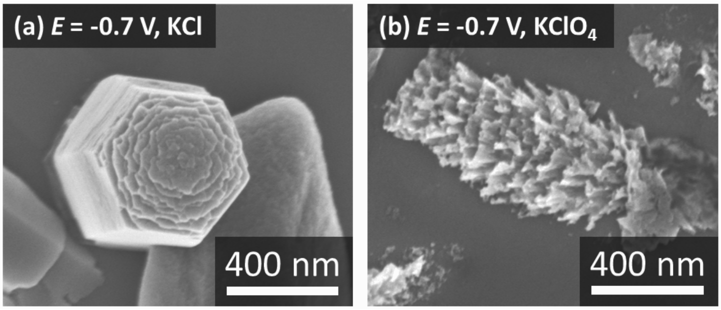

Fig. 4.9. SEM images of zinc oxide nanowires electrochemically deposited from O_2-saturated aqueous solutions containing 1 mM $ZnCl_2$ and either 0.1 M KCl (a) or 0.1 M $KClO_4$ (b) at a potential of $E = -0.7$ V vs. Ag|AgCl|3 M KCl and a temperature of $T = 70$ °C with stirring at 400 rpm.

oxide by means of ECD.

4.2.2.3. Optical Properties and Band Gap

In order to investigate the optical properties of zinc oxide, deposited by means of ECD, a closed ZnO layer was deposited on a sputter-deposited ITO substrate of approximately 900 nm thickness. The electrochemical deposition was performed under potentiostatic control at a potential of -0.9 V vs. Ag|AgCl|3 M KCl in an oxygen-saturated aqueous solution containing 5 mM $ZnCl_2$ and 0.1 M KCl. During deposition for $t = 6000$ s the solution was constantly stirred at 400 rpm and the temperature was maintained at $T = 60$ °C.

A thickness of $d = 470$ nm of the electrochemically deposited thin film was determined by masked etching and surface profiler measurement. The sheet resistance of $R_{\mathrm{sh}} = 55\ \Omega$ was measured by four-point probe. This was feasible due to the higher sheet resistance of the ITO substrate. Thus, the resistivity of the film is $\rho = 2.59 \times 10^{-3}\ \Omega$ and the deposition rate of $\nu_{\mathrm{dep}} = 0.27\ \mu\mathrm{m\,h^{-1}}$ was comparably low.

SEM images of a step prepared by masked etching in diluted HCl, are depicted in Fig. 4.10. No preferential orientation of the ZnO crystallites is evident and the film provides a considerable surface roughness. This is also apparent from its optical properties which are shown in Fig. 4.11. The total transmittance T_{tot}, the absorptance A, the reflectance R, and the haze in transmission $H_{\mathrm{T}} = T_{\mathrm{diff}}/T_{\mathrm{tot}}$ of the ITO substrate and the electrochemically deposited ZnO film are plotted as functions of the wavelength λ.

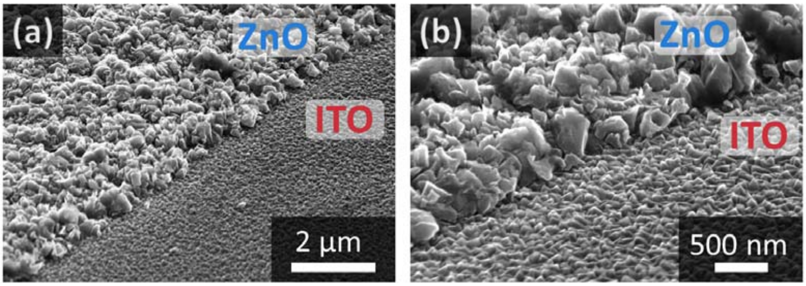

Fig. 4.10. SEM images of an ITO substrate layer and an electrochemically deposited ZnO film. ECD was conducted for $t = 6000$ s at -0.9 V vs. Ag|AgCl|3 M KCl in an aqueous solution containing 5 mM $ZnCl_2$ and 0.1 M KCl. The deposition bath was saturated with molecular oxygen and stirred at 400 rpm. The temperature was controlled and kept constant at $T = 60\,°\mathrm{C}$. The step visible in both images (a) and (b)was prepared using masked etching in diluted HCl.

The transmittance decreases over the whole wavelength range due to additional absorption in the ZnO layer. The magnitude of the interference pattern in both transmittance and reflectance decreases due to the surface roughness mentioned before. This roughness introduces light scattering which results in an increased haze. Another effect visible in Fig. 4.11a and Fig. 4.11b is a shift of the onset of fundamental absorption, *i.e.* of the optical band gap. Thus, the spectroscopic measurements depicted in Fig. 4.11 allow for the determination of the optical band gap of electrochemically deposited zinc oxide using Tauc plots (see page 16). The respective plot is shown in Fig. 4.12. The optical band gaps for the ITO substrate and the ZnO thin film are $E_{\mathrm{g}} = 3.76\,\mathrm{eV}$ and $E_{\mathrm{g}} = 3.5\,\mathrm{eV}$, respectively. The value for the zinc oxide layer is considerably higher than the value of $E_{\mathrm{g}} \approx 3.3\,\mathrm{eV}$ reported in the literature (see Table 2.1). This can be ascribed to Burstein-Moss shift of the band gap due to high charge carrier concentrations (see equation (2.17), page 16).

Doping of the electrochemically deposited zinc oxide can have several reasons. In the first place intrinsic doping can account for relatively high charge carrier concentrations. Pauporté and Lincot reported an increase of the band gap energy

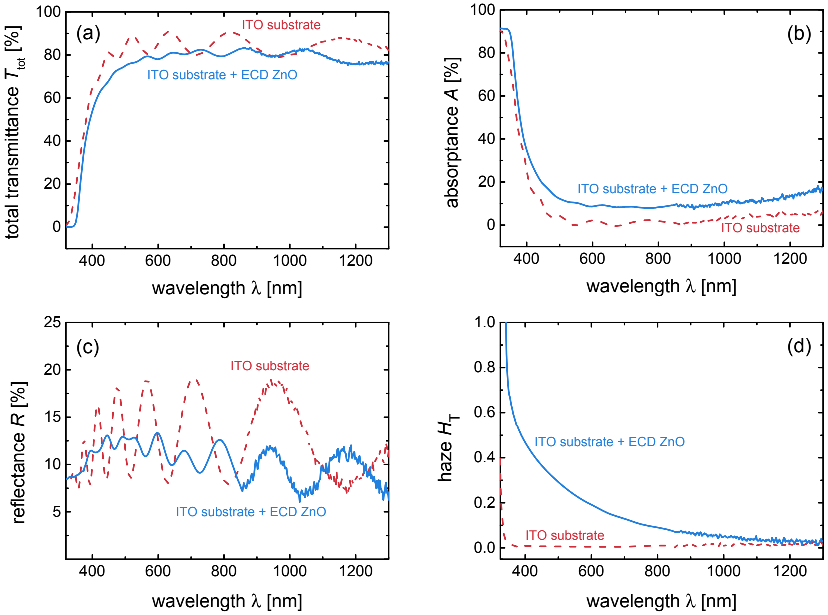

Fig. 4.11. Spectrally resolved (a) total transmittance T_{tot}, (b) absorptance A, (c) reflectance R, and (d) haze in transmission H_{T} of an ITO electrode on glass before (dashed line) and after ECD of a zinc oxide thin film (solid line). The zinc oxide layer was obtained at -0.9 V vs. Ag|AgCl|3 M KCl in an aqueous solution containing 5 mM $ZnCl_2$ and 0.1 M KCl with stirring and at a temperature of $T = 60$ °C.

in the range of 3.4 eV to 3.55 eV with increasing deposition potential [202]. Since this effect can be annealed by thermal heat treatment, hydrogen incorporation was suggested to be responsible for the increased band gap. However, at higher cathodic potentials the oxide precipitation might be accompanied by the reduction of Zn^{2+} to metallic zinc giving rise to the formation of Zn-rich zinc oxide films. Thus, oxygen vacancies or zinc interstitials are more likely to be responsible for n-type doping. Furthermore, due to hydrogen evolution occurring simultaneously during cathodic ECD of zinc oxide the incorporation of hydrogen cannot be excluded. This can also contribute to extrinsic doping (see section 2.2.2.1). In addition, contamination of the electrochemically deposited samples by other species in the deposition bath must be considered. Potassium has not been reported to be found in electrochemically deposited ZnO. Also, there is no evidence of either nitrate or nitrite supporting ions

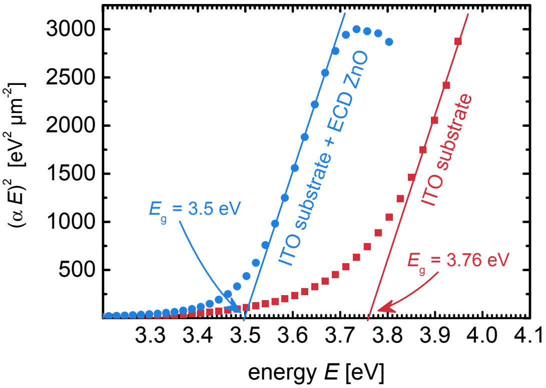

Fig. 4.12. Tauc plots for an ITO thin film on glass substrate before and after ECD of a ZnO thin film. The zinc oxide layer was obtained at -0.9 V vs. Ag|AgCl|3 M KCl in an aqueous solution containing 5 mM $ZnCl_2$ and 0.1 M KCl with stirring and at a temperature of $T = 60\,°C$. The optical band gaps of the ITO and the ZnO layers are determined to be $E_g = 3.76$ eV and $E_g = 3.5$ eV, respectively.

incorporating in zinc oxide (both molecules are too large). However, chloride can incorporate into zinc oxide [230], which was reported to lead to considerable n-type doping with charge carrier concentrations of up to $4 \times 10^{20}\,cm^{-2}$ [231].

4.3. Conclusion

Within this work zinc oxide was deposited using a solution based route for the first time at the IEK-5. ECD was performed using both nitrate and molecular oxygen reduction to manipulate the interfacial pH at the electrode such that zinc oxide precipitation is triggered. The effects of varying the deposition potential in case of ECD under potentiostatic control and the current density in case of galvanostatically controlled ECD were investigated. Higher cathodic potentials and current densities led to a higher density of nucleation sites and thus to a more homogeneous coverage of the surface. However, the crystallite size decreases simultaneously. The reduction of nitrate is strongly dependent on the zinc ion concentration which is ascribed to a catalytic effect of the Zn^{2+} ions. Therefore, the electrochemical deposition from nitrate based solutions changes strongly with zinc concentration. Furthermore, low zinc concentrations and high temperatures appear to promote the growth of hexagonal crystallites. In case of low potentials due to the lack of nucleation sites the crystallites form nanowires due to the preferred growth on the (0001) crystal face. The growth on ITO and ZnO:Al substrates revealed a fundamental influence of the substrate. On ZnO:Al the electrochemical deposition appeared to proceed epitaxially on the provided surface, conserving the grain size and orientation. Under identical conditions, the growth on ITO electrodes led to hexagonally shaped crystals, denoting good crystalline quality, with apparently random orientation of the c-axis with respect to the substrate normal. Furthermore, the anion species of the supporting salt was found to have a crucial impact on the deposited structures. In particular, perchlorate ions deteriorate the crystalline structure and seem to promote simultaneous corrosion.

Finally, on the example of a closed ZnO thin film, it was found by optical characterization that the films are degenerately doped. An optical band gap of $E_\mathrm{g} = 3.5$ eV was determined for the investigated film, suggesting degenerate doping by either intrinsic defects, hydrogen, or chloride incorporated in the film.

For further studies some improvements of the experimental setup might be useful. Specifically, the contacts of the substrate samples should be isolated such that wetting of the contact due to the condensation of evaporated solution is prevented. Therewith, a temperature range up to 90 °C would be accessible. Since sufficiently high temperatures were found to be important for the formation of crystalline zinc oxide this could help to improve the ZnO properties, keeping in mind the possible application in solar cells.

Other possibilities to improve the zinc oxide quality might be pre-treatments of the substrates and a thermal post-deposition treatment. Pre-treatments are regularly done to activate the surface of TCO electrodes and were found to enhance the growth rate and the homogeneity of the films. This can be done either chemically [202,251] or by a cathodic treatment [186,188,198,209,209,252]. Also, post-deposition annealing was shown to be beneficial for the film properties [253,254]. The annealing of defects in a single ZnO nanorod and the resulting improvement of local carrier concentrations and mobilities was recently reported by Stiegler *et al.* [255]. They investigated an annealing process at 450°C using scanning near field spectroscopy and transmission electron microscopy.

In conclusion the electrochemical deposition was successfully used to study the growth of zinc oxide from aqueous solutions. The major factors of influence on the formation of crystalline zinc oxide by means of ECD were investigated and promising first results were achieved. However, more work is necessary to optimize the deposition process in order to obtain thin films and nanostructures satisfying the prerequisites for the application in optoelectronic devices. Possibilities for further improvement were outlined and the necessary effort seems reasonable. This would open up new perspectives for future light scattering structures and anti reflection coatings in the application in thin-film silicon solar cells using a cost-efficient deposition technique. Furthermore, no elaborate vacuum processes are used and upscaling to very large areas is feasible as the example of electroplating shows, which has been implemented for decades *e.g.* in automotive industry.

5. Chemical Dissolution of Zinc Oxide

This chapter focuses on the chemical dissolution of zinc oxide in diverse acidic solutions. To start with, an introduction to the topic is presented. In section 5.1 a method is introduced which allows for the determination of the chemical dissolution rate by means of an electochemical measurement. This method, originally developed by Engell et al. *[256], is then applied in section 5.2 for both buffered and unbuffered acidic solutions. Furthermore, ZnO:Al thin films with two doping concentrations are investigated to evaluate the effect of carrier concentration on the dissolution rate. In section 5.3 the results are summarized and discussed.*

The chemical etching of zinc oxide thin films is of importance for several scientific fields, *e.g.* the structuring of thin-film transistors [257] or the resistance to corrosion in ambient media [258–260]. For the application of aluminum-doped zinc oxide as a TCO in some optoelectronic devices, such as light emitting diodes or thin-film solar cells, a rough surface is required to provide efficient light scattering [1, 261]. Conventionally, a simple chemical etching step in diluted HCl is applied to introduce a light scattering surface texture to sputter-deposited ZnO:Al thin films [1, 262]. Thereby, a crater-like surface texture is achieved with a typical root mean square surface roughness of 40 - 150 nm. SEM images of different magnifications of a typical surface morphology after 40 s etching in 0.154 M (0.5 w/w%) HCl are depicted in Fig. 5.1. The actual surface texture depends strongly on both the material properties, which are determined by the deposition parameters [2], and the etching conditions (*i.e.* etchant species, concentration, temperature) [263, 264].

To understand the chemical dissolution of zinc oxide thin films, it is advantageous to learn from the dissolution of single crystalline zinc oxide which has been under investigation since the early 1960s [265–267]. It can be understood on the basis of its wurtzite crystal structure and a dangling bond model, originally developed for III-V semiconductors [268–270]. Zinc oxide shows amphoteric character being able to accept protons towards mono-hydroxy complexes (and ultimately Zn^{2+} species via $2\ ZnO + 4\ H^+ \rightleftharpoons 2\ [ZnOH]^+ + 2\ H^+ \rightleftharpoons 2\ Zn^{2+} + 2\ H_2O$) or hydroxyl ions giving $[Zn(OH_3)]^-$ [258, 271]. Thus, it can be etched in either acidic or alkaline solutions

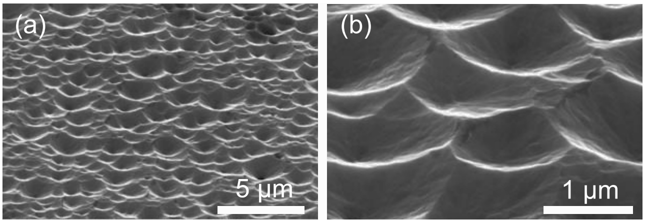

Fig. 5.1. SEM images of typical ZnO:Al surface morphologies after 40 s etching in diluted (0.154 M HCl). The scale bars correspond to (a) 2 µm and (b) 500 nm.

and the conditions for thermodynamic stability are rather narrow, *e.g.* around *p*H 6-11 [152, 272]. However, dissolution rates under moderate conditions are fairly low due to either slow kinetics [153] or transport limitations [258]. Fruhwirth [273] *et al.* and Gerischer *et al.* [153] investigated the chemical dissolution kinetics of zinc oxide crystals in aqueous electrolytes.

The missing symmetry of the wurtzite crystal structure accounts for anisotropic etching and different dissolution kinetics for the different crystal planes. Fig. 5.2 shows SEM images of the polar (0001) and $(000\bar{1})$ crystal surfaces after treatment in acidic (HCl) and alkaline (NaOH) solutions. The zinc-terminated (0001) surface exhibits inverted hexagonal pyramids upon treatment in acidic media and a random upright hexagonal pyramid texture upon treatment in alkaline media. In contrast, the oxygen-terminated $(000\bar{1})$ face is relatively unaffected by acidic treatment and shows inverted pyramids similar to the ones on the zinc-terminated face upon treatment in acids.

Only few models for the dissolution of zinc oxide thin films were proposed [263, 274]. Their polycrystalline nature introduces a more complex dissolution behavior due to inherent defects like grain boundaries and dislocations. A comprehensive description of the dissolution process of polycrystalline zinc oxide is still missing. However, observed trends gradually allow conclusions to be drawn. Generally, it is found that more compact films show a lower density of etching sites [2, 262]. In a recent review, a phenomenological model for the chemical etching of zinc oxide thin films has been proposed, based on the assumption that each grain boundary has a certain inherent probability to serve as an active site for etching, depending on both the compactness of the grain boundary and the etchant [263]. The anodic electrochemical dissolution, which is discussed in chapter 6, represents an extreme

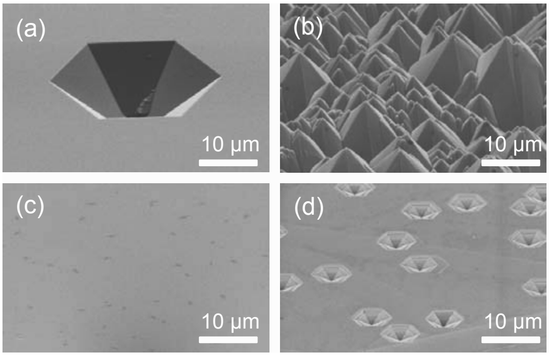

Fig. 5.2. SEM images of (a) (0001) oriented zinc oxide single crystal surface (Zn-terminated) and (b) $(000\bar{1})$ oriented zinc oxide single crystal surface (O-terminated) etched in HCl, and (c) (0001) oriented zinc oxide single crystal surface (Zn-terminated) and (d) $(000\bar{1})$ oriented single crystal zinc oxide surface (O-terminated) etched in NaOH. Taken from Hüpkes *et al.* [29].

case within this model, being able to attack grain boundaries with high selectivity.

The most decisive factors for the dissolution of zinc oxide in acidic media at room temperature, other than the material properties itself, are the *p*H value of the etchant and the anion species of the acid, which will be examined in this chapter.

5.1. Electrochemical Determination of the Chemical Dissolution Rate of Metal Oxides

Gerischer and Sorg [153] investigated the dissolution kinetics of zinc oxide single crystals. This has the advantage of having a good knowledge about the material in terms of the stoichiometry and the orientation of the crystal lattice. Inhomogeneities within the material, lattice defects, and porosity can be neglected in this case. Thus, the dissolution kinetics are more easily accessible. Generally, for high rates of dissolution the transport of the reagents or products in the solution is rate determining. This is especially the case in the absence of convection [58]. Unfortunately, upon dissolution of polycrystalline ZnO:Al layers the surface area varies during the process and the influence of transport processes is not easily accessible. However, the method used by Gerischer and Sorg, which was originally introduced by Engell [256, 275] and was later also applied by Williams [276] and Erbse *et al.* [277], is also applicable to the chemical dissolution process of polycrystalline zinc oxide thin films. This will be shown in section 5.2. Therefore, it will be reviewed briefly in this section.

When an n-type semiconductor like ZnO:Al dissolves stoichiometrically, *i.e.* without oxidation or reduction, electrons remain and accumulate at the surface until their activity is sufficiently high to reduce a component of the solution. The dissolution of ZnO:Al in an aqueous solution will be connected with hydrogen evolution corresponding to the rate of electron accumulation. The reaction follows

$$\mathrm{Zn}_{1-x}\mathrm{Al}_x\mathrm{O} + (2+x)\,\mathrm{H}^+ \longrightarrow (1-x)\,\mathrm{Zn}^{2+} + x\,\mathrm{Al}^{3+} + \mathrm{H_2O} + \frac{x}{2}\,\mathrm{H}_2\,\cdot \tag{5.1}$$

If the electrons are simultaneously removed from the zinc oxide electrode the hydrogen evolution can be prevented. Therefore, a small anodic voltage has to be applied, creating a depletion layer at the zinc oxide/electrolyte interface. The excess electrons of the dissolved part of the ZnO:Al layer are then collected at the counter electrode where they can reduce H^+ ions in the electrolyte. By measuring the current of electrons through the external circuit a rate of dissolution can be determined if the doping concentration N_D is known.

Fig. 5.3 shows an illustration of such a cell in which the dissolution rate can be derived from the current of electrons passing the external connection between the two electrodes. This current depends on the doping level N_D, and the sensitivity of this technique increases in parallel with it [153].

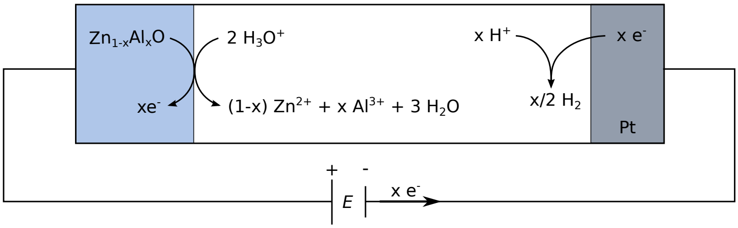

Fig. 5.3. Schematic illustration of the electrochemical cell with the interfacial reactions during chemical dissolution at small anodic bias potential of the ZnO:Al thin film (adapted from [153]).

The electrically determined rate of dissolution ν in $\mathrm{mol\,cm^{-2}\,s^{-1}}$ is connected with the stoichiometry of the $\mathrm{Zn_{(1\text{-}x)}Al_xO}$ by the relation

$$\nu = \frac{1}{x\,\mathrm{F}}\,j, \tag{5.2}$$

where j is the current density and F is the Faraday constant. The correlation between the stoichiometry x and the doping concentration N_D of a semiconductor is given by

$$x = \frac{M\,N_\mathrm{D}}{\rho\,\mathrm{N_A}} \tag{5.3}$$

where M is the molar mass, ρ is the density, and $\mathrm{N_A}$ is the Avogadro constant. The numerical values of the material parameters are given in Table 5.1. A more intuitively accessible dissolution rate in $\mathrm{nm\,s^{-1}}$ can be achieved via

$$\nu\,\left[\mathrm{nm\,s^{-1}}\right] = \frac{10^{-7}\,M}{\rho}\,\nu\,\left[\mathrm{mol\,cm^{-2}\,s^{-1}}\right], \tag{5.4}$$

assuming a homogeneous dissolution, which is fulfilled only on a macroscopic scale. This allows for the comparison between the electrochemically determined values and those from layer thickness measurements that are obtained by means of masked step etching and surface profiler measurements.

Table 5.1. Relevant values for the calculation of the rate of dissolution.

Quantity		Value and unit	Reference
molar mass of ZnO	M	$= 81.369\,\mathrm{g\,mol^{-1}}$	[278]
density of ZnO	ρ	$= 5.6730\,\mathrm{g\,cm^{-3}}$	[278]

Using the current density data to monitor the etching process, on-line process control is feasible. Both the actual dissolution rate and the accumulated amount of material or layer thickness can be determined *in-situ* from the current density and the charge density, respectively, using equation (5.2). Knowing the charge carrier density of the initial layer, *e.g.* from van der Pauw measurements, the presented method allows to stop the etching process when a desired layer thickness is removed.

5.2. Application to ZnO:Al thin films

The determination of the dissolution rate utilizing the introduced method was conducted in both unbuffered sulfuric and hydrochloric acids and acetate buffer solutions of differing *p*H values. This allows for the study of the effects of both the anion species and the *p*H value. Furthermore, ZnO:Al thin films with 1 w/w% and 0.5 w/w% Al_2O_3 were investigated to evaluate the effect of dopant concentration on the dissolution rate. The charge carrier concentration N_D was determined by van der Pauw measurements (see section A.4.4). The used aqueous electrolyte solutions are listed in Table 5.2. The total electrolyte concentration was 0.1549 M in HCl and H_2SO_4 solutions and 0.1 M in acetate buffer solutions to provide sufficient ionic conductivity.

Table 5.2. Used hydrochloric acid, sulfuric acid, and acetate buffer solutions with different acid concentrations and resulting measured *p*H values.

Etchant	Acid concentration [$\mathrm{mol\,l^{-1}}$]	pH (measured)
HCl	0.1549	1.23
HCl	0.1000	1.44
HCl	0.0100	2.43
HCl	0.0010	3.42
HCl	0.0001	5.05
H_2SO_4	0.1549	0.86
H_2SO_4	0.1200	1.10
H_2SO_4	0.0400	1.74
H_2SO_4	0.0050	2.75
H_2SO_4	0.0006	3.40
CH_3COOH	0.0948	3.50
CH_3COOH	0.0851	4.00
CH_3COOH	0.0644	4.50
CH_3COOH	0.0364	5.00
CH_3COOH	0.0153	5.50

All ZnO:Al samples were cut into 50 mm × 11 mm. Each series was conducted with pieces of the same 10 cm × 10 cm sample and all samples with the same doping concentration were sputter-deposited in one run to keep the measurements comparable. Furthermore, a fresh solution was used for each measurement in order to ensure constant conditions.

5.2.1. Integrity of the Method

Linear sweep voltammetry was used to determine a cathodic potential, which is small enough not to induce any additional electrochemical reaction on the one hand and sufficient to remove the accumulated electrons from the working electrode on the other hand. Fig. 5.4 shows such measurements in acetate buffer solutions of differing *p*H values. In the potential range between approximately 0.3 V and 1.3 V the current is relatively constant for all solutions before it increases due to the onset of oxygen evolution. In addition to that, it is already apparent that the current, and thus the dissolution rate, increases with decreasing pH. All further measurements were conducted at 0.3 V which is the smallest potential within the potential range of constant current density to assure minimal impact on the chemical dissolution rate. However, it is worth noting that dissolution rates determined at 0.3 V and 0.6 V were virtually identical.

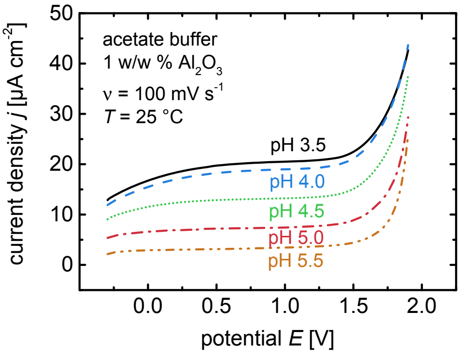

Fig. 5.4. Linear sweep voltammograms of ZnO:Al (1 w/w % Al) thin films in acetate buffer solutions of different *p*H at a temperature of $T = 25$ °C. The measurements were conducted with a scan rate of $\nu = 100\,\mathrm{mV\,s^{-1}}$. The potential is referred to a Ag|AgCl|3 M KCl reference electrode.

The most important assumption of the method is that the applied voltage does not induce any additional electrochemical dissolution. Thus, the measured current density only reflects the transport of the accumulating electrons from the ZnO:Al working electrode to the counter electrode. With respect to the electrochemical series (*e.g.* [57]) this assumption seems reasonable. To ensure that the applied potential of $E = 0.3\,\mathrm{V}$ vs. Ag|AgCl|3 M KCl does not influence the rate of dissolution, an identical measurement was conducted at open circuit potential (OCP), *i.e.* with no current flow through the external circuit, and the rate of dissolution was measured by means of film thickness measurements. The dissolution rates with and without external potential were identical within the accuracy of the measurements. Therefore, it is concluded that the assumption is met, meaning that the small external voltage has no effect on the dissolution rate but only relocates the reaction of the electrons from the working electrode to the counter electrode.

Furthermore, it has to be noted that the chemical dissolution is transport limited. Fig. 5.5 shows chronoamperometric transients at 3 V in a H_2SO_4 solution of pH 2.75. The current density is given on the left y-axis and the corresponding calculated dissolution rate is given on the right y-axis. One measurement was conducted without convection (dashed) while the other was performed with stirring by means of a magnetic stirrer with a speed of rotation of 1200 rpm. The measurement without convection exhibits a constant current density of approximately $4\,\mu A\,m^{-2}$ corresponding to a dissolution rate of approximately $3 \times 10^{-9}\,mol\,cm^{-2}\,s^{-1}$. In contrast, the measurement with stirring (solid) exhibits a distinctly higher dissolution rate, which decreases with time and drops to zero after an etching time of approximately 500 s. The decrease is probably related to a slow increase of the pH in the unbuffered system due to the consumption of protons at the counter electrode (see equation (5.1) and Fig. 5.3). When the current drops to zero the entire zinc oxide layer is dissolved. Additionally, the stirring introduces noise, either due to turbulent flow or induced electromagnetic fields. All measurements presented in the following sections were carried out without stirring.

5.2.2. Unbuffered Acids

The presented method was utilized to investigate the dependency of the dissolution rate on the pH of H_2SO_4 and HCl solutions. The dissolution of polycrystalline ZnO:Al with focus on the resulting surface texture was extensively investigated previously [4, 264, 279, 280]. Especially, surface texturing using HCl has been exhaustively studied in numerous works [2, 29, 262, 281–283]. However, there are few studies on the dissolution kinetics of polycrystalline thin films [264]. Furthermore, so far, no *in-situ* determination of the dissolution rate of polycrystalline zinc oxide was feasible. Reported dissolution rates were usually determined by step etching and mechanical measurement of the thickness difference which has the inherent drawback of being a destructive, *ex-situ* measurement.

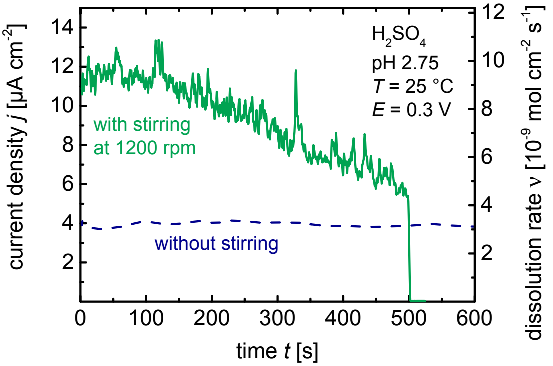

Fig. 5.5. Chronoamperometric measurements in 0.1549 M H_2SO_4 solution of *p*H 2.75 at T = 25 °C and E = 0.3 V vs. Ag|AgCl|3 M KCl. Comparison between a measurement without stirring (dashed) and with stirring at 1200 rpm by means of a magnetic stirrer introducing convection (solid). The current density translates via equation (5.2) in the rate of dissolution which is given on the right y-axis. With convection the current density, and thus the rate of dissolution, is distinctly higher. After approximately t = 500 s the ZnO:Al thin film is completely dissolved upon stirring while without stirring the dissolution of ZnO:Al continues at constant rate.

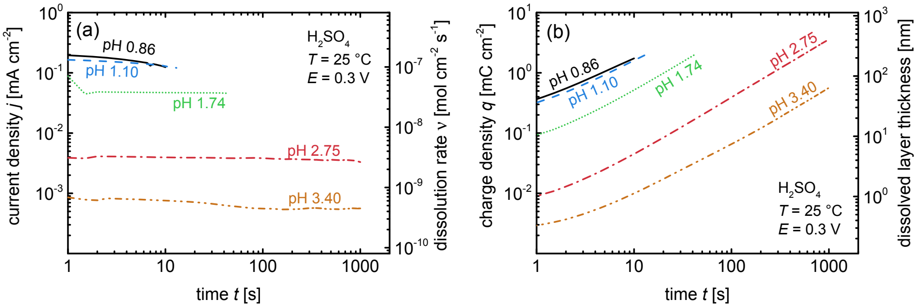

Fig. 5.6. (a) Chronoamperometric transients of ZnO:Al thin films at E = 0.3V vs. Ag|AgCl|3 M KCl and T = 25 °C in 0.1549 M H_2SO_4 solutions with differing *p*H values. The rate of dissolution given on the right y-axis was calculated via equation (5.2). In the *p*H range between 0.86 and 3.5 it varies by several orders of magnitude. (b) Charge density transients corresponding to the chronoamperometric measurements depicted in (a). By integrating equation (5.4) an effective thickness of the dissolved ZnO:Al layer was calculated which is given on the right y-axis.

Fig. 5.6(a) and Fig. 5.7(a) depict current density measurements during dissolution of zinc oxide thin films in 0.1549 M H_2SO_4 and HCl solutions, respectively, with differing *p*H values. A potential of $E = 0.3$ V was applied and the temperature was maintained at $T = 25$ °C. Due to the variation of the current density over several orders of magnitude a logarithmic scaling was chosen. This applies for the time scale as well because long treatment times were necessary at moderate *p*H values to provide sufficient layer removal allowing to measure thickness differences using a surface profiler. Via equation (5.2) the dissolution rate was calculated from the measured current density and is given on the right y-axis. For the calculation the charge carrier density of a reference sample from the same 10 cm × 10 cm substrate was used.

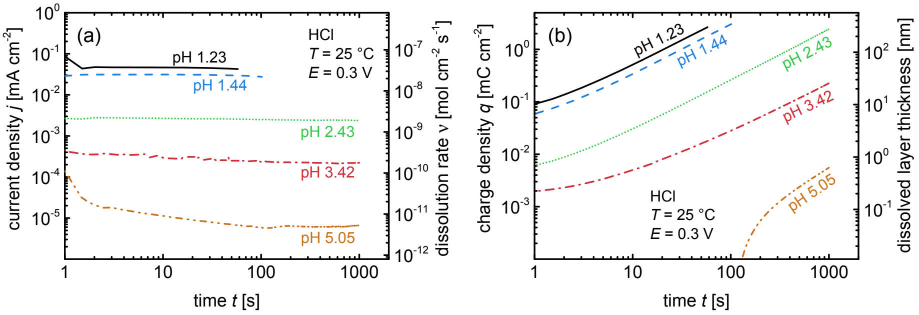

Fig. 5.7. (a) Chronoamperometric transients of ZnO:Al thin films at $E = 0.3$V vs. Ag|AgCl|3 M KCl and $T = 25$ °C in 0.1549 M HCl solutions with differing *p*H values. The rate of dissolution given on the right y-axis was calculated via equation (5.2). In the *p*H range between 1.23 and 5.05 it varies by several orders of magnitude. (b) Charge density transients corresponding to the chronoamperometric measurements depicted in (a). The effective layer thickness of dissolved ZnO:Al given on the right y-axis was calculated integrating equation (5.4).

In Fig. 5.6(b) and Fig. 5.7(b) the charge per surface area of the sample under test which was measured in the external circuit is plotter vs. treatment time. This charge density if simply the integrated current density. Thus, by integrating equation (5.2) over time it yields the amount of dissolved material. Assuming homogeneous dissolution and a density of $\rho = 5.673\,\mathrm{g\,cm^{-3}}$ which is reported in literature [278], an effective thickness of the dissolved layer can be estimated. This layer thickness is reported on the right y-axis in Fig. 5.6(b) and Fig. 5.7(b). Note that it takes 1000 s to dissolve 0.7 nm ZnO:Al in a HCl solution of *p*H 5.05. The method is thus very sensitive and able to determine dissolution rates in a broad range. In particular, the regime of moderate pH values with slow kinetics, where thickness measurements are time consuming, is fast and easily accessible.

This becomes clear in Fig. 5.8 which plots dissolution rates of zinc oxide thin films and crystals in dependence on the pH of the solution. Open symbols correspond to film thickness measurements while closed symbols refer to current density measurements.

Both methods are in good agreement except for the higher pH values, where the uncertainty of the thickness measurement is larger than the actual value. A linear relationship between pH and logarithmic dissolution rate was observed. The dissolution in H_2SO_4 was found to be faster than in HCl. This is in good agreement to the findings of Gerischer *et al.* [153, 284] on sintered zinc oxide pellets and zinc oxide single crystals. Data of the zinc-terminated (0001) face are included in Fig. 5.8. The pH dependence, *i.e.* the slope of the linear fit, for the polycrystalline films is the same for H_2SO_4 and HCl. This also applies to the (0001) crystal surface. However, the slope for single crystals is slightly less steep. This difference might be ascribed to the large degree of intrinsic heterogeneity in the polycrystalline films which is accompanied by a loss of significance of the individual etching behavior of different crystal orientations. The findings are consistent with those of Owen *et al.* [264] who observed similar dissolution rates for comparable thin films.

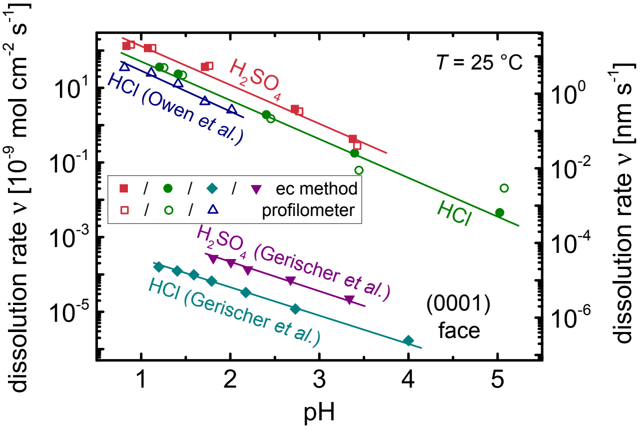

Fig. 5.8. Chemical dissolution rates in H_2SO_4 and HCl determined by current density measurements (closed symbols) and layer thickness measurements (open symbols), respectively, plotted vs. the *p*H of the respective solution. For reasons of clarity symbols are slightly shifted in case they overlap. Dissolution rates are given in $\mathrm{mol\,cm^{-2}\,s^{-1}}$ as well as in $\mathrm{nm\,s^{-1}}$. Besides the data from this work, dissolution rates of polycrystalline zinc oxide thin films determined by Owen *et al.* [264] and of (0001) oriented zinc oxide crystals by Gerischer *et al.* [153] are depicted for comparison.

5.2.3. Acetate Buffer

The chemical dissolution rates of ZnO:Al thin films in 0.1 M acetate buffer solutions of differing *p*H values were investigated by the method introduced in section 5.1. Fig. 5.9 depicts the results for two different doping concentrations. Fig. 5.9(a) and (b) provides data of thin films with a nominal Al_2O_3 target doping of 1 w/w % and Fig. 5.9(c) and (d) presents data of samples with 0.5 w/w % Al_2O_3 target doping. During the measurement an external potential of $E = 0.3$ V vs. Ag|AgCl|3 M KCl was applied and the temperature was maintained at $T = 25$ °C. In contrast to the measurements in unbuffered solutions current density variation was within one order of magnitude. Note that the measurements are therefore plotted without logarithmic scaling.

It can be seen from Fig. 5.9(a) and (c) that the current density in acetate buffer solutions also increases with increasing acid concentration. Hence the dissolution rate, which is linearly correlated to the current density (see equation (5.2), increases

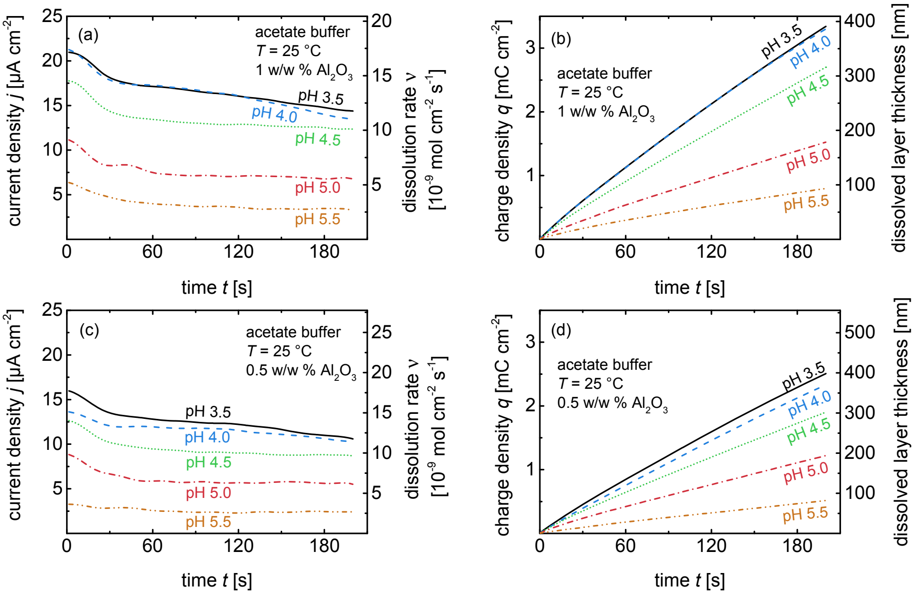

Fig. 5.9. Determination of the chemical dissolution rate via chronocoulometric measurement at $E = 0.3\,\mathrm{V}$ of ZnO:Al thin films in acetate buffer solutions of differing pH at a temperature of $T = 25\,°\mathrm{C}$ with (a) and (b) 1 w/w % Al_2O_3 target doping and (c) and (d) 0.5 w/w % Al_2O_3 target doping. The potential is referred to an Ag|AgCl|3 M KCl reference electrode.

with decreasing pH. Note that the dissolution rate depends on the carrier concentration (see equations (5.2) and (5.3)). As a consequence, the layers with different doping concentration exhibit very similar dissolution rates for the same pH value, despite the fact that the measured current densities were higher for higher carrier concentrations.

Average dissolution rates of the analyzed samples are illustrated in Fig. 5.10. Samples with nominal doping concentration of 1 w/w % are depicted as squares while 0.5 w/w % is figured as dots. Open symbols correspond to values determined by thickness measurements and closed symbols relate to current density measurements. It is apparent from this graph that the thickness measurements constantly give lower dissolution rates as compared to the electrochemical method. This is likely due to an underestimation of the removed layer thickness by the surface profiler. The craters developing during dissolution on the ZnO:Al surface usually have diameters of less than 500 nm up to 2 µm. Thus, the comparably large stylus of the surface profiler (approximately 12 µm) will penetrate only a few nanometers into the craters. On the other hand the as-deposited surface of ZnO:Al is relatively smooth. Hence, the initial thickness value is not overestimated. The surface profiler measurements thus give a lower limit for the removed thickness d_{diss}, given by the difference between the as-deposited d_0 and etched d_{etch} films ($d_{\mathrm{diss}} = d_0 - d_{\mathrm{etched}}$), and consequently a lower limit on the etch rate. Owen *et al.* found that the root mean square roughness of ZnO:Al layers after etching decreases with increasing pH [264]. This might explain why the deviation between the two methods diminishes for higher pH values.

Neither of the two methods showed a dependence of the dissolution rate on the doping concentration. Accordingly, the structural properties of the ZnO:Al thin films, which were very similar for all films, are more important for the dissolution process than deviations in the doping concentration.

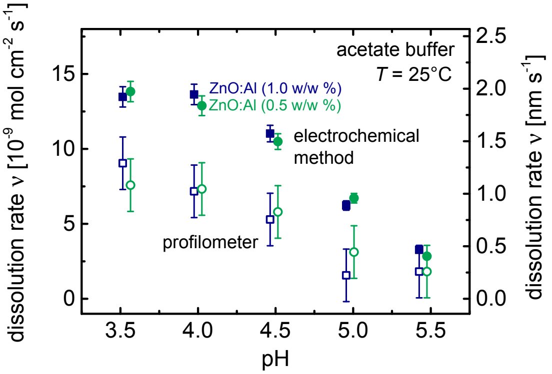

Fig. 5.10. Chemical dissolution rates of ZnO:Al thin films in 0.1 M acetate buffer solutions of differing pH at a temperature of $T = 25\,°\mathrm{C}$ with 1 w/w % and 0.5 w/w % Al_2O_3 target doping determined by the electrochemical method and by film thickness measurements, respectively. For reasons of clarity symbols are slightly shifted in case they overlap.

5.3. Discussion

In conclusion, it was shown that the method developed by Engell *et al.* [256] can be successfully applied to polycrystalline zinc oxide thin films. It allows for the *in-situ* determination of the chemical dissolution rate on the basis of current density measurements. Furthermore, it enables an active control of the etching process since it provides access to the thickness of the dissolved film during etching. Thus, the etching process can be stopped at any desired film thickness.

A comparison of the results with dissolution rates from the literature and from thickness measurements, performed on the same samples, shows very good agreement. However, in some cases thickness measurements by means of a surface profiler underestimate the dissolution rate depending on the surface roughness after etching.

For similar *p*H values the chemical dissolution of ZnO:Al thin films was observed to be slightly higher in H_2SO_4 solutions as compared to HCl. This is in good agreement with the literature [153]. A possible explanation might be the higher complex formation constant of sulfate ions [132, 285].

Fig. 5.11 reveals that the dissolution kinetics in acetate buffer solutions were considerably higher than in unbuffered HCl and H_2SO_4 solutions of the same pH. This can be attributed to the buffering effect which ensures a stable *p*H while the *p*H in unbuffered solutions might increase during etching due to the consumption of H^+ (see equation (5.1)). Furthermore, acetic acid is known to enhance zinc oxide dissolution [153, 284, 286].

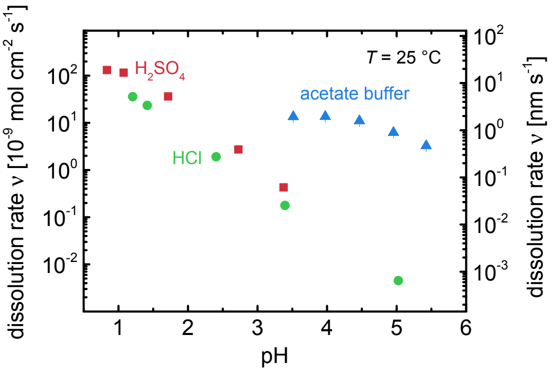

Fig. 5.11. Comparison between dissolution rates of ZnO:Al thin films in H_2SO_4, HCl, and acetate buffer solutions in the acidic *p*H regime at $T = 25\,°C$. Dissolution in acetate buffer solution is strikingly faster than in the unbuffered solutions of the same pH.

ZnO:Al layers with varying charge carrier concentration exhibited the same dissolution rates. Given the fact that the charge carrier density is essential for the calculation of the dissolution rate (see equation (5.2)), this is another proof of the reliability of the used method.

6. Electrochemical Dissolution of Zinc Oxide

This chapter is concerned with the anodic dissolution of polycrystalline aluminum-doped ZnO thin films. Even though anodic dissolution of passive oxide layers on metallic zinc electrodes and single crystalline zinc oxide electrodes has been studied for several decades, the dissolution of polycrystalline thin films has proven to deviate in several aspects. It turns out that the microstructure and inherent inhomogeneity, due to the abundance of grain boundaries in this material, crucially determine the dissolution process. The goal of this work is to increase the understanding of this dissolution process and to identify its major influencing factors. The focus is set on the resulting surface morphologies and the modification of the electrical and optical thin film properties aiming at the applicability of electrochemically textured ZnO:Al thin films in silicon thin-film solar cells. Furthermore, the selectivity of the dissolution process to the grain boundary regions is discussed on the basis of a charge transfer model. After a short introduction to the field (section 6.1) and details of the experimental conditions (section 6.2), results on the anodic dissolution of zinc oxide are presented in section 6.3. A comprehensive discussion of the observations which aim to understand the underlying mechanism can be found in section 6.4. The chapter is finally concluded in section 6.5.[1]

6.1. Introduction

Electrochemical investigations on the dissolution of ZnO started with the experimental and theoretical study of oxide layers on metals because of their importance for passivity in corrosion sience [287–290]. These passivating layers very often feature a polycrystalline structure comparable to the sputter deposited oxide layers investigated here. Gerischer [154] and Lohmann [6] investigated the anodic dissolution of ZnO

---

[1] Some of the results presented here were published in J.-P. Becker *et al.*, *Electrochim. Acta* (2013), 112, 976–982

single crystals under UV illumination already in the 1960s. It was stated that anodic dissolution of ZnO is only possible under UV illumination because the process was driven by charge transfer with holes in the valence band [5, 145]. Most studies were concerned with zinc oxide having charge carrier densities below $1 \times 10^{18}\,\mathrm{cm}^{-3}$. These electrodes show a blocking behavior in the anodic potential region up to several V vs. SHE. The electrochemical behavior of polycrystalline zinc oxide layers was reported for the first time in 1990 by de Wit *et al.* who used both cathodic and photo-anodic dissolution. Again anodic dissolution was observed only upon illumination. They observed preferential decomposition at the grain boundaries which was attributed to higher rate constants resulting from the disturbances of the lattice periodicity [146]. Although the interest in zinc oxide electrodes for applications such as dye sensitized solar cells has increased considerably and the long term stability of zinc oxide in solution remains a challenge, systematic studies of the electrochemically triggered dissolution are lacking. This chapter will show that anodic electrochemical dissolution of degenerately doped ZnO:Al thin films in aqueous electrolytes is feasible without illumination using anodic potentials of around 2 V vs. SHE are applied. This novel anodic dissolution process is studied in detail with special focus on the resulting surface textures and their opto-electronic properties in relation to their applicability in thin-film solar cells.

The anodic dissolution of zinc oxide is supposed to proceed via two competing reactions. The direct lattice decomposition (6.1) and the oxygen evolution reaction (OER, (6.2)) with subsequent chemical dissolution of the crystal lattice (6.3) [145, 150].

$$2\,\mathrm{ZnO} \rightarrow 2\,\mathrm{Zn}^{2+} + \mathrm{O}_2 + 4\,\mathrm{e}^- \tag{6.1}$$

$$2\,\mathrm{H_2O} \rightarrow 4\,\mathrm{H}^+ + \mathrm{O}_2 + 4\,\mathrm{e}^- \tag{6.2}$$

$$\mathrm{ZnO} + 2\,\mathrm{H}^+ \rightarrow [\mathrm{ZnOH}]^+ + \mathrm{H}^+ \rightarrow \mathrm{Zn}^{2+} + \mathrm{H_2O} \tag{6.3}$$

As reported in [291] the grain boundaries are highly preferred etch sites, whereas the grains remain relatively intact. Thus, during electrochemical dissolution, the overall film thickness persists, but grooves develop at the grain boundaries.

6.2. Experimental

The anodic dissolution of degenerately doped, polycrystalline zinc oxide thin films was studied using sputter-deposited ZnO:Al layers. If not stated otherwise the layers had a thickness of approximately $d = 850\,\mathrm{nm}$ and a sheet resistance of approximately $R_{\mathrm{sh}} = 3\,\Omega$. After deposition on 100 mm × 100 mm glass substrates, samples were cut into 50 mm × 25 mm or 50 mm × 11 mm pieces, respectively, depending on the further characterization. Each sample was then connected as the working electrode in a conventional three-electrode setup (see Fig. 3.2 in paragraph 3.2.1). The contact was established using a metallic clamp. A geometrical surface area of approximately $9\,\mathrm{cm}^2$ or $5\,\mathrm{cm}^2$, respectively, of the sample surface was exposed to the electrolyte and carefully measured after each treatment using a micrometer caliper. Furthermore, the treatment of 100 mm × 100 mm samples was feasible using an electrochemical cell developed for this sample size (see paragraph A.3). Currents and charges are reported normalized to the geometric sample area in order to account for small deviations in sample size. All potentials are referred to a Ag|AgCl|3 M KCl reference electrode. The temperature was maintained constant at 25 ± 0.5 °C during electrochemical experiments if not stated otherwise. Anodic polarization was done either potentiostatically or galvanostatically. Aqueous solutions of K_2SO_4, KCl, KNO_3, and $KClO_4$ or phosphate, acetate, and borax buffers were prepared from analytical grade chemicals and used as an electrolyte. After electrochemical treatment, the samples were carefully cleaned in hot, deionized water to remove salt residues originating from the electrolyte solution.

6.3. Results

An overview of the electrochemical behavior of a zinc oxide thin film electrode and the reactions, which take place upon application of a bias potential, can be obtained using cyclic voltammetry. The cyclic voltammograms depicted in Fig. 6.1 are recorded with a scan rate of 10 mV/s in 0.1 M NaCl and KCl solutions, respectively. The data indicates a potential window between approximately −0.6 V up to +1.3 V vs. Ag|AgCl|3 M KCl where ZnO:Al is electrochemically stable. In this blocking potential regime, no net current flow is observed in near neutral *p*H regimes. However, this potential range can be used to quantify the chemical dissolution rate as shown in chapter 5. At more cathodic potentials, a reduction to metallic zinc is observed (R_1) and at even higher cathodic potentials the hydrogen evolution reaction

(HER, reaction (3.11)) starts. This is discussed in chapter 4. In the anodic scanning direction an oxidation peak is observed (O_1) which corresponds to the stripping of the electrodeposited metallic zinc. Under anodic polarization, dissolution of ZnO:Al via equations (6.1) – (6.3) occurs. Both cyclic voltammograms exhibit exactly the same behavior. This suggests that the role of the cation is negligible, which is also observed for electrochemical deposition of ZnO [245].

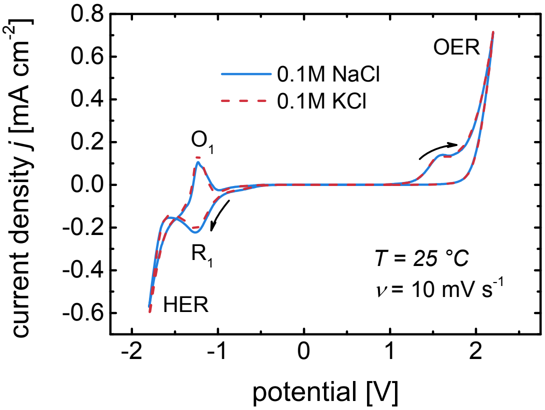

Fig. 6.1. Cyclic voltammograms in 0.1 M aqueous solutions of NaCl and KCl, respectively. The scan rate was 10 mV s^{-1} and the temperature was maintained at $T = 25$ °C. The peaks are discussed in the text. The potential is referred to a Ag|AgCl|3 M KCl reference.

The onset potential of anodic current in the dark was determined from a Tafel plot of a potential sweep in 0.1 M $KClO_4$ depicted in Fig. 6.2a. A value of 1.287 V vs. Ag|AgCl|3 M KCl was measured. Onset potentials in K_2SO_4, KCl, and KNO_3 did not deviate significantly from this value.

Furthermore, a Mott-Schottky analysis of electrochemical impedance spectroscopy (EIS) measurements was used to measure the charge carrier concentration and the flat band potential of the ZnO:Al/electrolyte interface (see section 3.3.1). EIS measurements were conducted in a propylene carbonate electrolyte containing 0.1 M $NaClO_4$ to avoid ZnO decomposition during the measurements [292]. Each measurement was performed applying a 10 mV ac sinusoidal signal over the constant applied bias in the frequency ranging between 1 MHz and 1 mHz. The impedance spectra were fitted using an equivalent circuit (see Fig. 6.3) consisting of a series resistance R_s (resistance of the leads and the electrolyte) and a constant phase

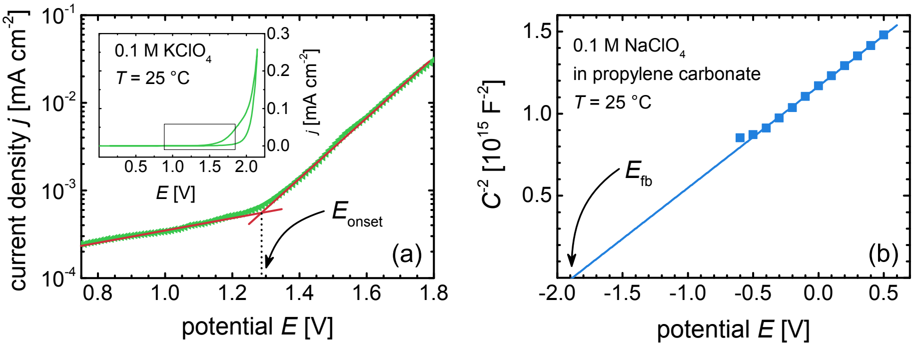

Fig. 6.2. (a) Tafel plot of a ZnO:Al thin film electrode in an aqueous 0.1 M $KClO_4$ solution. The onset potential E_{onset} of anodic current is determined by the point of intersection of the two linear fits of the data. In the case depicted here, $E_{\mathrm{onset}} = 1.287$ V. The inset plots the whole cyclic voltammogram from which the data were taken. (b) Mott-Schottky plot of a ZnO:Al thin film electrode in a propylene carbonate solution containing 0.1 M $NaClO_4$. The capacity was measured by fitting an equivalent circuit (see Fig. 6.3) comprising a resistance and a parallel connection of another resistance and a constant phase element in series to electrochemical impedance spectra in the frequency range between 10 mHz and 1 MHz. The intersection of the linear fit with the abscissa provides the flat band potential $E_{\mathrm{fb}} = -1.916$ V while the slope was used to calculate a charge carrier concentration of the ZnO:Al thin film of $N_{\mathrm{D}} = 9.6 \times 10^{20}\ \mathrm{cm}^{-3}$.

element (CPE) with a parallel resistance R_{ct} (charge transfer resistance). The CPE represents a non-ideal capacitor and is regularly used to fit EIS data of rough or inhomogeneous electrodes. The potential drop in the Helmholtz layer was assumed to be small. Thus, the total capacitance is dominated by the capacitance of the space charge layer. The measured impedance spectra did not show a full semicircle in the Nyquist representation, indicating a high charge transfer resistance. The capacity determined from the fits to the data is displayed in the Mott-Schottky plot depicted in Fig. 6.2. A linear dependence of C^{-2} vs. E was observed as predicted by the Mott-Schottky equation (3.9). From the slope of the linear fit a charge carrier concentration of $N_{\mathrm{D}} = 9.6 \times 10^{20}\ \mathrm{cm}^{-3}$ was determined. Within the measurement errors this corresponds well to the value measured using the van der Pauw method. The intercept of the fit with the potential axis yields the flat band potential $E_{\mathrm{fb}} = -1.916$ V vs. Ag|AgCl|3 M KCl. Compared to values reported for moderately doped ZnO crystals, this value is rather low [140–143]. However, it was reported by Van den Meerakker *et al.* [293] that for degenerately doped ITO films the flat band potential decreases with increasing carrier concentration. The situation for degenerately doped ZnO is expected to be similar.

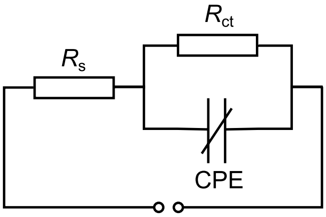

Fig. 6.3. Equivalent circuit used to fit electrochemical impedance spectra. The series resistance R_s and the parallel resistance R_{ct} represent the ohmic resistance of the leads and the electrolyte and the charge transfer resistance, respectively. The constant phase element corresponds to the non-ideal capacitance of the space charge layer.

6.3.1. Electrochemical Dissolution Rate

To trigger electrochemical dissolution at a reasonable rate, an anodic potential of approximately +2 V is necessary. Fig. 6.4a shows a current density transient during anodic polarization at a constant potential of $E = 2.1$ V in a 0.1 M K_2SO_4 solution. The current density drops in the beginning which can be ascribed to the formation of the electrochemical double layer. Subsequently, it increases until a maximum is reached and finally decreases to zero. The increase is probably due to the development of a surface texture which is accompanied by an increase of the active surface area. At the same time the sheet resistance of the ZnO:Al layer increases when material is dissolved, limiting the charge transport through the layer and consequently decreasing the current density. Thus, the drop of the current density represents a decrease of the conductivity of the zinc oxide layer.

The amount of dissolved ZnO n_{diss} can be calculated using Faraday's first law of electrolysis with the exchanged charge per surface area q by

$$n_{\text{diss}} = \frac{\eta_c}{2\,\mathrm{F}}\,q, \tag{6.4}$$

where F denotes the Faraday constant. The current efficiency η_c was measured as 88 % using chemical analysis of the products in the solution [294]. This was done for

ZnO:Al thin films deposited using the same deposition process as those used here. A rate of dissolution ν in mol cm^{-2} s^{-1} can be achieved by the time derivative of the equation (6.4),

$$\nu = \frac{dn_{\text{diss}}}{dt} = \frac{\eta_c}{2\,\mathrm{F}}\frac{dq}{dt} = \frac{\eta_c}{2\,\mathrm{F}}\,j. \tag{6.5}$$

This dissolution rate is displayed on the right-hand y-axis of Fig. 6.4a and allows for a comparison between the measurements and the chemical dissolution rates determined in chapter 5. The maximum dissolution rate measured in the depicted graph corresponds to a chemical dissolution in H_2SO_4 at approximately pH 3. The charge density which is forced through the zinc oxide/electrolyte interface by applying the anodic potential is plotted in Fig. 6.4b. When the current density vanishes, the charge density saturates at a plateau value of approximately $q = 175\,\mathrm{mC\,cm^{-2}}$. Assuming homogeneous dissolution of the ZnO:Al thin film, an effective thickness of the dissolved material d_{eff} can be calculated, giving a quantity allowing an estimation of how much of the initial layer is dissolved,

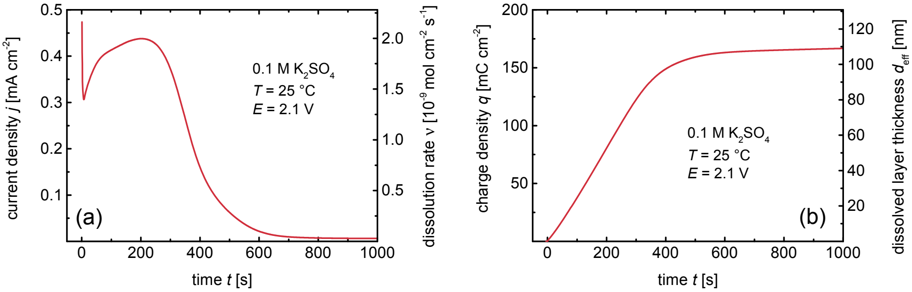

Fig. 6.4. Current density transient at $E = 2.1$ V vs. Ag|AgCl|3 M KCl in 0.1 M K_2SO_4 solution at $T = 25$ °C.

$$d_{\text{eff}} = \frac{\eta_c}{2\,\mathrm{F}}\frac{M}{\rho}\,q. \tag{6.6}$$

Here, ρ and M are the density and the molar mass of zinc oxide. The same numerical values as used for analog calculations in chapter 5 were applied. They can be found in Table 5.1 (page 55). This effectively dissolved layer thickness is displayed on the right-hand ordinate in Fig. 6.4b. Please note that the saturation value is at $d_{\mathrm{eff}} \approx 110\,\mathrm{nm}$ indicating that only a fraction of approximately 13% of the initial layer was dissolved. So if the reason for the decreasing current density in Fig. 6.4a is a drastically increasing sheet resistance of the thin film, the dissolution does not proceed homogeneously. Indeed, as already mentioned at the beginning, the electrochemical dissolution of polycrystalline zinc oxide thin films is very sensitive to the microstructure and preferentially starts at the grain boundaries.

6.3.2. Potential Dependence

The cyclic voltammogram in Fig. 6.1 suggests a drastic increase of the current density with increasing anodic potential. Further chronoamperometric measurements in 0.1 M K_2SO_4 conducted at differing anodic potentials are depicted in Fig. 6.5a. The current density transients are plotted in log-log scale because both the current density and the time vary by several orders of magnitude. As expected, the current density is drastically higher for higher potentials. Consequently, it takes shorter for the same amount of material to dissolve. Apart from the scaling, the current density transients have the same shape for each potential. Fig. 6.5b shows the corresponding charge densities plotted vs. time. A higher current density triggered by a higher applied potential results in a steeper slope of the charge density. In addition, the saturation value of the current decreases with increasing potentials. The inset of Fig. 6.5b plots the saturation values vs. the applied potential. Apparently, at higher dissolution rates less material can be dissolved before the current density vanishes.

Thus, at higher potentials less material must dissolve to obtain the same effect on the conductivity of the thin films. This can also be seen in Fig. 6.6 which shows the sheet resistance of ZnO:Al thin films anodized at differing potentials until a charge density of $q = 60\,\mathrm{mC\,cm^{-2}}$ was exchanged at the electrode. Consequently, the amount of dissolved material was the same for each sample. The measurements were conducted in both sulfate and chloride solutions and both series are plotted. The sheet resistance of the samples treated in sulfate solution increases with increasing applied potential. Thus, the expectations are met. However, in the potassium chloride solution no dependence of the sheet resistance on the applied potential was observed. Even though it also increased during the dissolution process. The sheet resistance of the as-deposited layers was $R_{\mathrm{sh}} = 2.9\,\Omega$. A similar dependence of the sheet resistance on the current density is observed when the anodic dissolution is conducted galvanostatically, *i.e.* at constant current density.

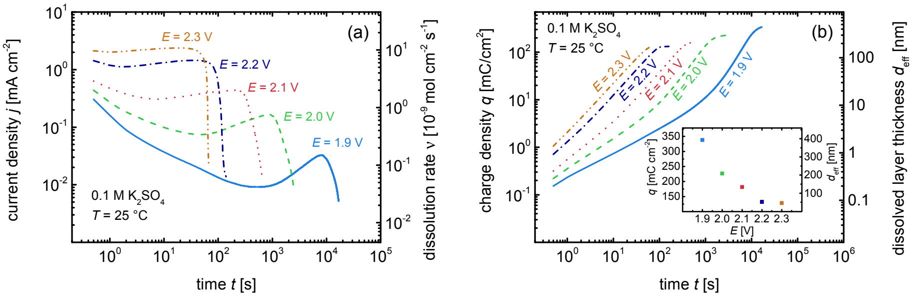

Fig. 6.5. Chronoamperometric anodic polarization of sputter-deposited ZnO:Al thin films in an aqueous 0.1 M K_2SO_4 solution at differing potentials E in the range between 1.9 and 2.3 V vs. Ag|AgCl|3 M KCl. The temperature was maintained at $T = 25$ °C. (a) shows the current density transient which is expressed as a dissolution rate via equation (6.5) on the right ordinate. (b) plots the charge density transferred at the electrode surface and the corresponding effectively dissolved layer thickness calculated via equation (6.6) is displayed on the right-hand ordinate. The saturation value of the charge density vs. the applied potential is plotted in the inset.

This impact of the electrolyte on the properties of electrochemically etched zinc oxide was observed for the first time and will be evaluated in detail in the following section. However, it has to be noted that the chemical nature of the electrolyte was reported to influence both the cathodic electrochemical deposition of ZnO thin films [164, 202, 244, 295–297] and the dissolution kinetics of zinc or ZnO in aqueous electrolytes [259, 285, 298, 299].

6.3.3. The Electrolyte

6.3.3.1. The Anion Species

Even if the anion species of the electrolyte does not participate in any of the reactions responsible for the dissolution, it apparently has a substantial influence on the resulting layer properties as Fig. 6.6 indicates. The influence of the electrolyte on the electrochemical dissolution of polycrystalline ZnO:Al thin films is investigated in detail to firstly improve the understanding of the electrochemical anodic dissolution of ZnO thin films and secondly to obtain possibilities to adjust the process to the requirements for thin-film solar cell front contacts. Therefore, the effect of the

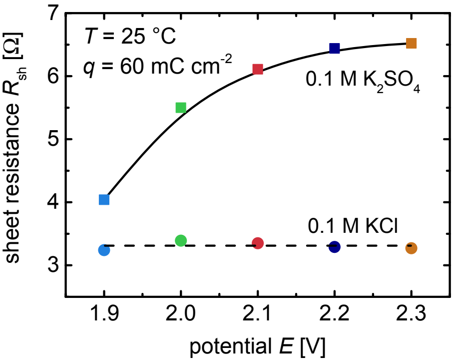

Fig. 6.6. Sheet resistance of ZnO:Al thin films after potentiostatic anodic polarization at differing potentials E in aqueous solutions of 0.1 M K_2SO_4 or KCl, respectively. The initial sheet resistance was $R_{sh} = 2.9\,\Omega$. The dissolution process was stopped when a charge density of $q = 60\,\mathrm{mC\,cm^{-2}}$ was exchanged. Approximately 4.5% of each ZnO:Al thin film was dissolved in this process. The temperature was maintained at $T = 25$ °C and the potential is referred to a Ag|AgCl|3 M KCl reference electrode.

anion species of common electrolytes such as K_2SO_4, KCl, KNO_3, and $KClO_4$ was investigated.

Fig. 6.7 compares chronoamperometric current density transients of four samples anodically polarized in 0.1 M solutions of the salts mentioned above. The initial pH values of the solutions were measured as 5.9, 5.6, 5.7, and 5.3 for K_2SO_4, KCl, and KNO_3, and $KClO_4$, respectively. However, chemical dissolution at significant rates was not observed when samples were stored in the solutions for more than 12 hours. The anodization was performed at a constant potential set to 2.1 V vs. Ag|AgCl|3 M KCl and the treatment was continued until the current density fell below 10 $\mu\mathrm{A\,cm^{-2}}$. Fig. 6.7 clearly shows differences in the dissolution behavior of the four samples, which are representative for the respective electrolyte. The initial drop of the current density in the beginning due to the formation of the electrochemical double layer was observed for each electrolyte. Also, a subsequent increase before the current density finally decreased to zero was found for all anion species. Thus, the conductivity of the ZnO:Al layer finally collapses independent of the electrolyte used. However, the shape of the current density evolution in the four solutions differed in some aspects. First of all the maximum current density was decreasing from K_2SO_4 over KCl and KNO_3 to $KClO_4$ corresponding to a decreasing dissolution rate. Consequently, the

ZnO:Al layer treated in K_2SO_4 breaks down electrically much faster, resulting in a diminishing conductivity, and hence, a drop of the current density to zero. The current density declined to zero in the other electrolytes as well, but the required time increased by a factor of approximately 4, 5.5, and 9 for chloride, nitrate, and perchlorate solutions, respectively. The intermediate increase of the current density was attributed to an enlargement of the active surface area during the local corrosion of the ZnO:Al layer.

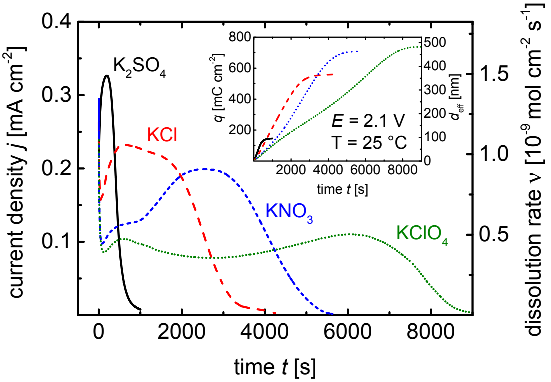

Fig. 6.7. Chronoamperometric anodization of ZnO:Al thin films in 0.1 M aqueous solutions of K_2SO_4, KCl, and KNO_3, respectively. A bias potential of $E = 2.1$ V vs. Ag|AgCl|3 M KCl was applied and the temperature was maintained at $T = 25$ °C. The right ordinate reports the dissolution rate ν corresponding to the measured current density. The inset shows the charge exchanged at the ZnO:Al/electrolyte interface q which corresponds to the altered material expressed as an effectively dissolved film thickness d_{eff} reported on the right ordinate of the inset.

The inset in Fig. 6.7 shows the charge per geometrical surface area that was exchanged at the ZnO:Al/electrolyte interface, which is linearly linked to the amount of altered material via Faraday's law (see equation (6.4)). The drastically lower saturation value in the case of the sulfate electrolyte illustrates that significantly less material was removed in K_2SO_4 before the current drops. Assuming a current efficiency of 88 % as was shown in Ref. [294] for the case of unbuffered aqueous solutions, approximately 11 %, 41 %, 52 %, and 56 % of the initial ZnO:Al layers were dissolved in K_2SO_4, KCl, KNO_3, and $KClO_4$, respectively.

Thus, the resulting surface textures evolving during the anodic treatment in the differing electrolytes must differ considerably. This was confirmed by SEM measurements of ZnO:Al layers after anodization in K_2SO_4 and KCl, respectively. Fig. 6.8a and Fig. 6.8b provide images of sample surfaces whereas Fig. 6.8c and Fig. 6.8d show cross sections of ZnO:Al layers after anodic treatment. Comparing the surface SEM pictures in Fig. 6.8a and Fig. 6.8b it is obvious that anodization in KCl removes a wider region around the grain boundaries than in K_2SO_4. Nonetheless, the grain boundaries are the initiation sites of the dissolution process in both cases. In K_2SO_4 (Fig. 6.8c) the grain boundaries were removed through the whole layer after an exchanged charge density of $q = 204\,\mathrm{mC\,cm^{-2}}$ whereas in KCl (Fig. 6.8d) the electrochemical etching process affected only the top part of the layer, even with $q = 320\,\mathrm{mC\,cm^{-2}}$. Please note that in the cross section images, particularly in Fig. 6.8d, some artifacts from the sample preparation using focused ion beam (FIB) are apparent. Namely the straight, vertical lines in the lower part of the layer are caused by the ion beam at points where either less or less dense material was in the layer above. Consequently, the ion beam was able to penetrate deeper into the layer. Hence, surface features or less compact material at the layer surface were propagated through the layer and cause these straight lines during preparation of the cross section. It is apparent from the cross sections that the total film thickness did not change and the interior of most grains remains unattached. This is particularly true for the samples etched in K_2SO_4, where the dissolution process proceeds much faster along the grain boundaries than in KCl. Thus, in a rather short time the ZnO:Al thin film consists of individual, isolated grains and the lateral resistance increases drastically. In contrast, the etching proceeds not exclusively vertical in KCl solutions but also some grains are attacked leading to a cavern-like porous structure with an intact layer underneath, which still provides lateral conductivity. This allows the anodic dissolution process, which depends on the current transport through the layer, to continue.

When a conductive and electrochemically stable layer is provided as a substrate, *e.g.* an indium tin oxide (ITO) thin film, then the anodic dissolution does not stop when the grains are separated by the dissolution of the grain boundaries. Instead the grooves widen up and the ZnO:Al grains are gradually dissolved completely. This can be seen in Fig. 6.9 which depicts SEM images taken at four stages of anodic dissolution in 0.1 M KCl, when charge densities of $q = 219.0\,\mathrm{mC\,cm^{-2}}$, $q = 309.8\,\mathrm{mC\,cm^{-2}}$, $q = 667.3\,\mathrm{mC\,cm^{-2}}$, and $q = 1326.3\,\mathrm{mC\,cm^{-2}}$ were transferred, respectively. In Fig. 6.9a the dissolved grain boundaries are clearly visible. During further anodic treatment the gaps between the grains increase (Fig. 6.9b) and in Fig. 6.9c, where approximately half of the initial material is dissolved, the grains are rarely recognized. Finally, the zinc oxide layer is completely dissolved and the clean ITO surface is left

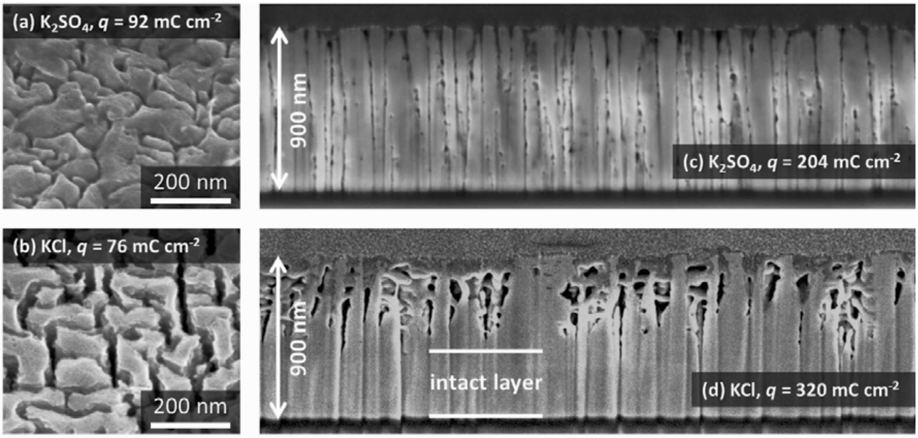

Fig. 6.8. (a) and (b) depict SEM images of ZnO:Al thin film surfaces after anodic treatment at a potenital of $E = 2.0$ V vs. Ag|AgCl|3 M KCl in K_2SO_4 and KCl, respectively. (c) and (d) show cross section SEM images of similar ZnO:Al thin films after prolonged anodic treatment in K_2SO_4 and KCl, respectively. The cross sections were prepared by means of focused ion beam (FIB). The charge density transferred during the anodic dissolution process is noted in the legend of each SEM image.

(Fig. 6.9d).

This behavior clearly indicates that the decrease of the current density for long treatment times is due to a decrease in lateral charge transport through the ZnO:Al thin films. Furthermore, Fig. 6.10 shows the evolution of the sheet resistance of ZnO:Al thin films anodized in the four electrolytes investigated here. A series of eight samples was anodically treated in each electrolyte for various times t. For each sample the sheet resistance R_{sh} after etching was determined *ex-situ* by means of a four-point probe measurement.

As expected, R_{sh} increased much faster during etching in K_2SO_4 as compared to KCl, KNO_3, and $KClO_4$, respectively. Please note that R_{sh} is not plotted versus the treatment time, but versus the exchanged charge or the effectively dissolved layer thickness d_{eff} displayed at the upper abscissa. Obviously, in K_2SO_4 less material has to be dissolved to increase R_{sh} drastically. Hence, this again shows that not only was the dissolution rate higher in the sulfate solution but also that the impact of the material dissolution on the electronic properties of the ZnO:Al layer was higher. This

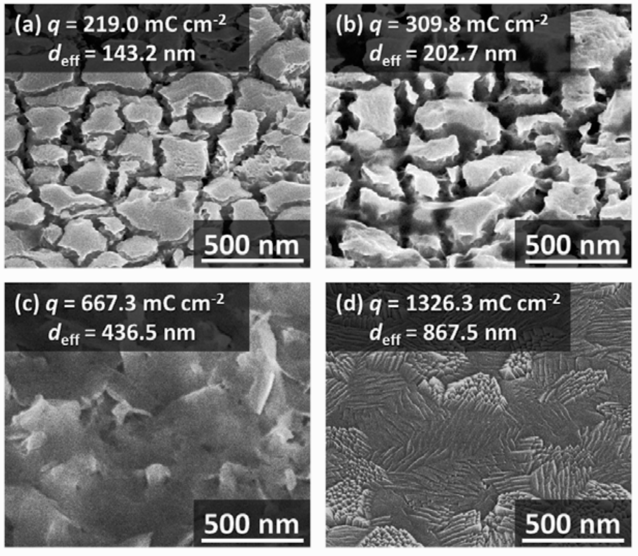

Fig. 6.9. SEM images of ZnO:Al thin films deposited on an ITO buffer layer and anodized in 0.1 M KCl at $E = 2.2$ V vs. Ag|AgCl|3 M KCl with a total exchanged charge of (a) 219.0 mC cm^{-2}, (b) 309.8 mC cm^{-2}, (c) 667.3 mC cm^{-2}, and (d) 1326.29 mC cm^{-2}. The ZnO:Al layer is gradually dissolved during the treatment. Dissolution starts at the grain boundaries (a) but finally the entire ZnO:Al layer is dissolved and the surface of the ITO substrate is exposed (d).

fits well to the structures observed in Fig. 6.9 and the interpretation of the current density transients during anodization. Specifically, the samples etched in K_2SO_4 exhibit features with a high aspect ratio, which effectively inhibit a lateral current transport through the layers and result in the observed high sheet resistance.

The different etched structures also provide differing optical properties. Fig. 6.11 depicts spectrally resolved optical absorption data of four ZnO:Al thin films on glass. The grey solid line represents the flat as-deposited state without any surface texturing. The other curves correspond to samples which were anodized in K_2SO_4, KCl, KNO_3, $KClO_4$ solutions at $E = 2.1$ V. All samples were treated with a total exchanged charge of approximately $q = 160$ mC cm^{-2}. Thus, the same amount of material was dissolved for all samples. Compared to the as-deposited state, the absoptance of the thin films treated in KCl, KNO_3, and $KClO_4$ decreases in the infrared but only a small shift of the plasma frequency was observed. In general, these three

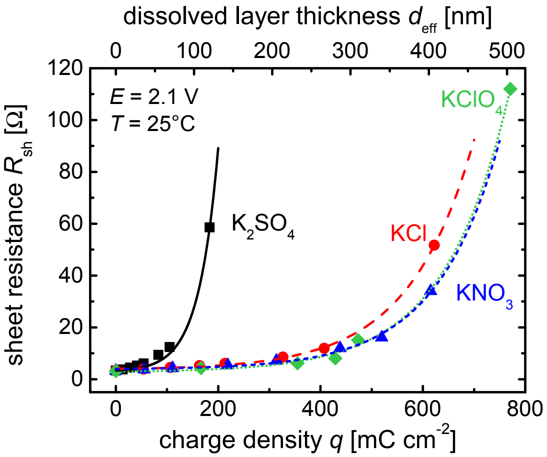

Fig. 6.10. Evolution of the sheet resistance of ZnO:Al thin films plotted against the charge density exchanged at the electrode as measured by van-der-Pauw setup during anodic dissolution at $E = 2.1$ V vs. Ag|AgCl|3 M KCl in 0.1 M K_2SO_4, KCl, KNO_3, and $KClO_4$, respectively. The upper abscissa reports the effective thickness of the dissolved material. The lines serve as a guide to the eye.

samples showed very similar absorption spectra. However, the sample anodized in K_2SO_4 showed a more pronounced decrease in the near infrared absorption, a drastic increase of the absorption above 1600 nm and a shift of the plasma frequency to higher wavelengths. It is worth noting that a similar treatment in a K_2SO_4 solution with a lower concentration of 0.06 M, exhibiting a conductance similar to the 0.1 M KCl and KNO_3 solutions, resulted in the same optical and electrical properties. Hence, the conductance of the solution, which was approximately twice as high as a similar concentration in K_2SO_4, had no relevant impact on the dissolution process. The decrease in the plasma peak can probably be ascribed to the removal of material whereas a shift of the plasma frequency to higher wavelengths may be attributed to a lower charge carrier density (see *e.g.* [300–302]). The inset in Fig. 6.11 shows only the short wavelength range around the band gap energy of zinc oxide. Apparently, the Burstein-Moss shift (see paragraph 2.2.3, page 15) exhibited by the as-deposited ZnO:Al thin film was reduced during anodic dissolution in all investigated electrolytes. However, the effect is most distinct for the treatment in K_2SO_4, which points to a more pronounced decrease of the charge carrier concentration. This is in agreement with the shift of the plasma peak in the infrared part of the spectrum [302].

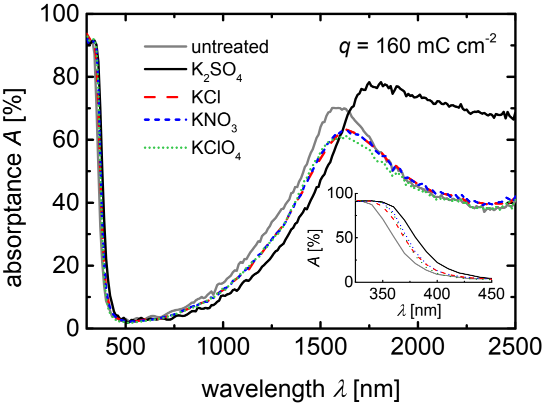

Fig. 6.11. Optical absorption spectra of ZnO:Al thin films on glass in the as-deposited state and after anodic treatment in aqueous solutions of K_2SO_4, KCl, KNO_3, and $KClO_4$. During anodization approximately 12 % of the initial layer was dissolved for each sample. The inset shows a closer view of the short wavelength range close to the band gap energy of ZnO:Al.

The decrease of the band gap during anodic polarization was examined in more detail on a series of samples treated in K_2SO_4 because the effect is most pronounced in sulfate solutions. Therefore the absorption coefficient was measured using photothermal deflection spectroscopy (PDS) and Tauc plots were prepared. The data of selected samples are depicted in Fig. 6.12. The onset of fundamental absorption, *i.e.* the band gap, apparently shifts to lower energies. The optical band gaps, as determined from the intersection of the fits of the linear part of the curves with the abscissa, are plotted agains the charge density exchanged during anodization in the inset of Fig. 6.12.

The band gap seems to decrease linearly with the amount of dissolved material until approximately 130 mC cm^{-2} were transferred at the ZnO:Al/electrolyte interface and the intrinsic band gap of zinc oxide, indicated by the dashed line in Fig. 6.12 is reached. Hence, the material is no longer degenerately doped and the charge carrier density is decreased drastically. Unfortunately, the determination of charge carrier densities using the van-der-Pauw method was not feasible for the anodically treated thin films because this method assumes compact and homogeneous layers. This requirement is evidently not fulfilled for the porous thin films obtained by anodic polarization presented here. However, the red shift of the band gap and the shift

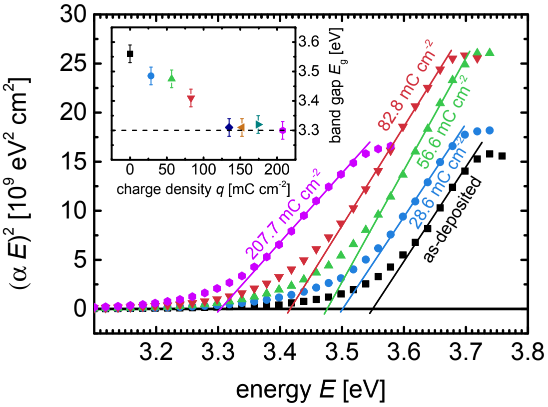

Fig. 6.12. Tauc plots of absorption data measured by PDS on ZnO:Al thin films after anodization in 0.1 M K_2SO_4 for different times. The corresponding charge density exchanged at the ZnO:Al/electrolyte interface is noted at each curve. The inset shows the corresponding optical band gap energies E_g as determined from the intersection of the linear fits with the abscissa. The dashed line corresponds to the band gap energies found in literature for ZnO without Burstein-Moss shift of approximately 3.3 eV [109, 303].

of the plasma peak in the near infra-red absorptance, clearly indicate a decreased charge carrier concentration. This decrease might originate from the drastically increasing surface area and corresponding surface states which are able to trap charge carriers and lead to a partial depletion of the grains. A further contribution to the red shift of the optical band gap may be the relaxation of compressive stress which is regularly observed in compact ZnO:Al thin films [304]. However, the red shift observed here seems too strong to be explained by relaxation of the material only. Charge carrier densities of the samples depicted in Fig. 6.12 were calculated based on the Burstein-Moss shift (equation (2.17)) and via the plasma frequency (equation (2.14)). Values in the range of $10^{19}\,\mathrm{cm}^{-3}$ were obtained for the longest treatment. A depletion of the whole grains is thus unlikely.

6.3.3.2. Buffered Electrolytes

The behavior of the anodic etching process in buffered solutions and its dependence on the pH value of the electrolyte solution was studied in phosphate buffer solutions in the range between pH 5.5 and 7.5 and in borax buffer solutions in the range between

pH 8 and 10.5. The buffer concentration was 0.1 M. Current density transients during anodic polarization in phosphate and borax buffer solutions of differing pH at $E = 2.1\,\mathrm{V}$ are depicted in Fig. 6.13a and Fig. 6.13b, respectively. The current density in all measurements decreases during the whole treatment however with decreasing slope so that it levels off at comparably low values as against measurements in unbuffered solutions with otherwise similar parameters. Also during considerably longer treatment times, no increase of the current density was observed in contrast to the findings in unbuffered solutions. The current efficiency of the anodic dissolution process in buffered solutions was measured as 62 % using chemical analysis of the products in the solution [294]. This efficiency is considerably lower than the efficiency of 88 % found for unbuffered solutions. The difference can be ascribed to the influence of the buffer on the proton induced etching subsequent to the OER by scavenging H^+ in the vicinity of the interface. For purely electrochemical lattice decomposition via reaction (6.1), *i.e.* without contribution of protons, no effect of the buffer would be expected.

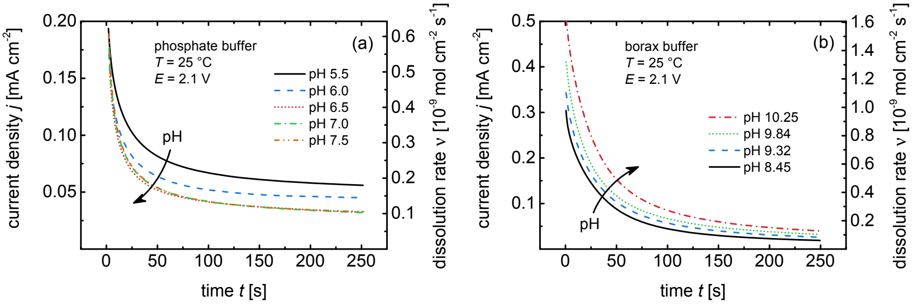

Fig. 6.13. Current density transients as recorded at an applied potential of $E = 2.1$ V vs. Ag|AgCl|3 M KCl in 0.1 M phosphate buffer solutions (a) and borax buffer solutions, respectively of differing pH. Measurements were conducted at constant temperature of $T = 25\,°\mathrm{C}$. The right ordinate of each plot reports the corresponding dissolution rate.

The electrochemical dissolution rates as determined from the measured current densities with the current efficiency of 62 % are displayed on the right-hand ordinate of Fig. 6.13a and Fig. 6.13b. Apparently, the electrochemical dissolution rate decreases when the pH is increased from 5.5 to 6.5 in phosphate buffer solutions. In the regime between pH 6.5 to 7.5 all current density transients exhibit a surprising conformity. The electrochemical dissolution rate in borax buffer solutions increases with increasingly alkaline pH. Please keep in mind that the chemical dissolution due to pH is not detected here, but only processes which involve charge transfer at the ZnO:Al/electrolyte interface, *i.e.* reactions (6.1) and (6.2).

To visualize the pH dependence, the charge density exchanged during 250 s of anodic dissolution in buffer solutions was plotted vs. the pH value of the solution in Fig. 6.14. The data were extracted from the measurements depicted in Fig. 6.13. Apparently, the dissolution rate has a minimum at near neutral pH and increases for both acidic and alkaline pH. This is in good agreement with the Pourbaix diagram discussed in section 3.4 which predicts a relative stability of zinc oxide in the range between approximately pH 6 and 11 and the dominant presence of dissolved zinc species for more acidic and alkaline pH values, respectively.

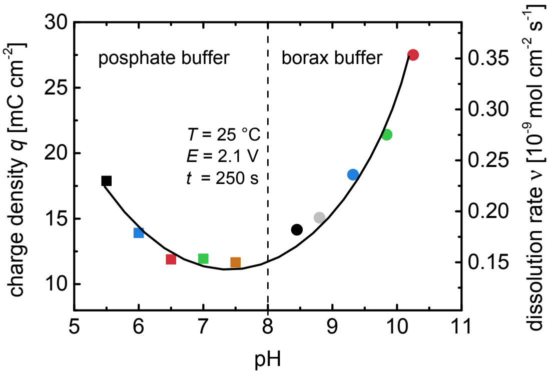

Fig. 6.14. Exchanged charge after t = 250 s of anodic polarization at a potential of E = 2.1 V vs. Ag|Ag|Cl3 M KCl in phosphate and borax buffer solutions of differing pH. The average rate of dissolution during the initial t = 250 s of treatment are displayed on the right-hand ordinate.

6.3.4. Photo-anodic Dissolution of ZnO:Al

The photo-dissolution of zinc oxide was reported in several studies [6,146,154,155,305]. It was found that illumination with light of a photon energy above the band gap of zinc oxide triggers the dissolution process by the generation of minority charge carriers. Thereby, charge transfer with the valence band is enabled which consequently leads to photo-decomposition of zinc oxide in contact with an electrolyte. To identify the impact of this pathway for dissolution of polycrystalline ZnO:Al thin films, samples were anodically treated in 0.1 M aqueous solutions of K_2SO_4 with and without illumination of the sample through the electrolyte. A UV lamp (*UV-4 S*, Herolab GmbH, Wiesloch, Germany) was used providing a power density $0.5\,\mathrm{mW\,cm^{-2}}$ of photons with a wavelength of $\lambda = 254\,\mathrm{nm}$ ($E_{\mathrm{photon}} = 4.88\,\mathrm{eV}$). The two current density transients are plotted in Fig. 6.15a and the corresponding charge densities are shown in Fig. 6.15b. The solid curves represent the measurement performed in the dark while the dashed curves show the behavior upon illumination. Apparently, the general shape of the curves is very similar. However, an elevated current density is observed initially upon illumination which is accompanied by an earlier decrease. Thus, the total charge density exchanged during the anodic dissolution is the same for both measurements. Overall, these findings point to a similar mechanism, albeit with an increased rate upon illumination.

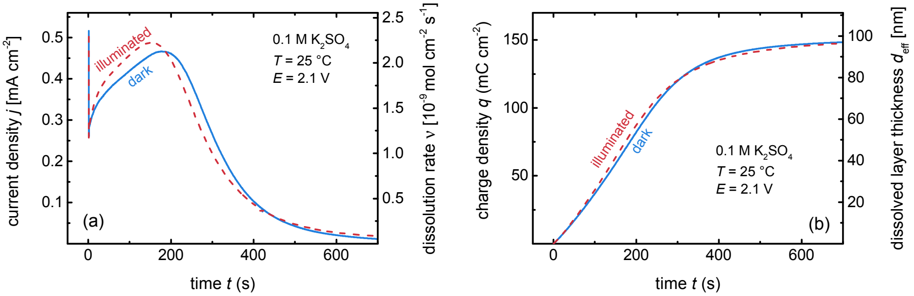

Fig. 6.15. Chronoamperometric anodic dissolution of ZnO:Al thin films in a 0.1 M aqueous solution of K_2SO_4 at a bias potential of $E = 2.1\,\mathrm{V}$ vs. Ag|AgCl|3 M KCl in the dark (solid lines) and upon illumination with UV light of a photon energy well above the zinc oxide band gap (dashed lines). The temperature was maintained at $T = 25$ °C. (a) Current density transients and corresponding dissolution rate ν (on the right-hand ordinate). (b) Evolution of the charge density exchanged at the ZnO:Al/electrolyte interface. The corresponding calculated effective thickness of the dissolved material is displayed on the right-hand ordinate.

Fig. 6.16 shows a similar experiment, however in this case the sample was illuminated with UV light pulses of only 10 s in different stages of the anodic dissolution process at $E = 2.1\,\mathrm{V}$ vs. Ag|AgCl|3 M KCl. The light was switched on at $t = 100\,\mathrm{s}$, $t = 250\,\mathrm{s}$, and $t = 450\,\mathrm{s}$, respectively, for ten seconds each. The current density response to the illumination is very rapid. A magnification of the photocurrent pulse is depicted in the inset of Fig. 6.16. The current density contribution due to illumination is approximately $j_{\mathrm{photo}} = 10\,\mathrm{\mu A\,cm^{-2}}$. An estimation of the space charge layer thickness based on the photo-current was unfortunately not possible since the exact light intensity on the sample surface was not known in the used setup. However, the enhancement of the dissolution rate upon illumination with UV light provides clear evidence that the anodic dissolution process of zinc oxide is limited by the charge transfer at the zinc oxide/electrolyte interface. This is in contrast to the diffusion limited process of chemical dissolution investigated in chapter 5. Here, by generating additional minority charge carriers upon illumination with light of a suitable wavelength, the charge transfer with the valence band is enhanced resulting in a higher current density. The increase of the majority charge carrier density is probably due to degenerate doping.

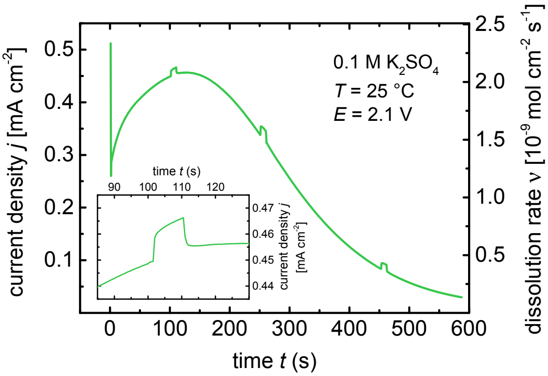

Fig. 6.16. Current density transient during anodic polarization of a ZnO:Al thin film electrode at a potential of $E = 2.1\,\mathrm{V}$ vs. Ag|AgCl|3 M KCl in 0.1 M K_2SO_4 solution at $T = 25\,°\mathrm{C}$. During the anodic dissolution process the sample was illuminated with UV light for ten seconds at $t = 100\,\mathrm{s}$, $t = 250\,\mathrm{s}$, and $t = 450\,\mathrm{s}$, respectively. The inset shows a magnification of the curve during the first light pulse.

6.3.5. Detection of the Aluminum Dopant

Considering the unique ability of the anodic dissolution process to selectively dissolve the material in the vicinity of the grain boundaries, it in principle enables the separate characterization of the bulk and the grain boundary material. An interesting question might be whether the aluminum dopants are homogeneously distributed throughout the thin films or if accumulation or clustering at the grain boundaries occurs. The simple idea is to utilize the selectivity of the anodic dissolution process to the grain boundaries to allow for a separate analysis of the chemical composition of the grain boundaries and the bulk material.

The electrochemical experiments were performed with a microelectrochemical flow cell developed in the frame of the thesis of Klemm [271]. The setup uses an 1 mm O-ring to confine the surface under investigation by pressing a capillary cell on the substrate with a well-defined force of 50 mN as monitored by a force sensor. The capillary itself is divided by a separating wall where one compartment holds the electrolyte supply channel and a Ag|AgCl reference electrode (205 mV vs. SHE) [306], whereas the other holds the electrolyte drain and the Pt counter electrode. The cylindrical space created by the O-ring above the substrate provides the pathway for the electrolyte to flow from one compartment to the other (at $190\,\mu l\,s^{-1}$). A detailed description of the scanning flow cell setup can be found elsewhere [271, 307]. The electrolyte including dissolution products is analyzed *in-situ* by means of inductively coupled plasma mass spectrometry (ICP-MS). This method ionizes the solution in a plasma and then a mass spectrometer is used to separate and quantify the ions. Each experiment was carried out at an individual location on the substrate to ensure that the initial surface properties were identical for all measurements.

Fig. 6.17 depicts the results of two measurements performed in 0.5 mM HCl (pH 3.3) under galvanostatic and potentiostatic control, respectively. The diagram depicted in Fig. 6.17a shows the dissolution of a polycrystalline ZnO:Al thin film under galvanostatic conditions. The concentration of zinc [Zn] and aluminum [Al] in the electrolyte were measured. Furthermore the ratio between dissolved Al and Zn is plotted in percent ([Al]/[Zn]). Initially, the current density was maintained at $j = 0$. Thus, purely chemical dissolution at OCP was observed. The measured aluminum to zinc ratio was approximately 0.6 %. Please note that the investigated ZnO:Al thin films were sputter-deposited from a target containing 1 w/w% alumina. This corresponds to [Al]/[Zn]$\approx$ 0.4 %. However, at deposition temperatures above $T = 100\,°C$, it was found that Zn desorbs during sputtering which leads to higher aluminum contents [308]. This is apparently the case for the ZnO:Al thin films investigated here which were sputter-deposited at $T = 200\,°C$. Thus, the observed ratio of aluminum to zinc is well in the expected range.

The application of a comparably high anodic current density of $j = 1.27\text{mA}\,\text{cm}^{-2}$ results in additional anodic dissolution of the ZnO:Al thin film which finds expression in an increased concentration of Zn in the solution. In contrast, less Al was detected at this current density. Consequently the ratio between Al and Zn was much lower.

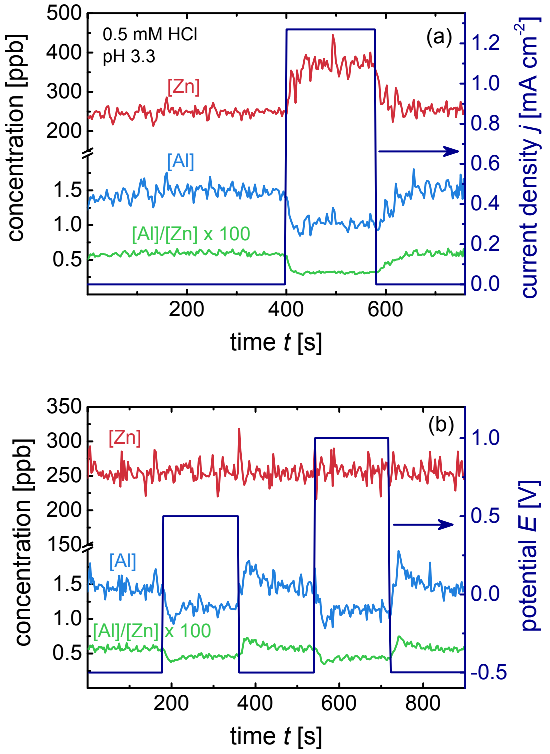

Fig. 6.17. Zinc and aluminum dissolution profiles during dissolution of ZnO:Al thin films in 0.5 mM HCl (pH 3.3) under differing galvanostatic and potentiostatic conditions. The left-hand y-axes display the concentration of dissolved zinc and aluminum in the solution as measured by ICP-MS. Furthermore, the ratio of dissolved aluminum to zinc in solution is plotted in percent. (a) Initially the potential was kept at open circuit potential (OCP), *i.e.* $j = 0$. At $t = 400\,\mathrm{s}$ the anodic current density was set to $j = 1.27\,\mathrm{mA\,cm^{-2}}$ and from $t = 580$ s the cell was again maintained at OCP until the flow cell was detached from the sample surface. The measurement depicted in (b) was conducted under potentiostatic control. The applied potential is displayed on the right-hand ordinate. Chronoamperometric steps were performed between $E = -0.5$ V (approx. OCP) and $E = +0.5$ V or $E = +1$ V, respectively. All potentials are referred to a Ag|AgCl reference electrode.

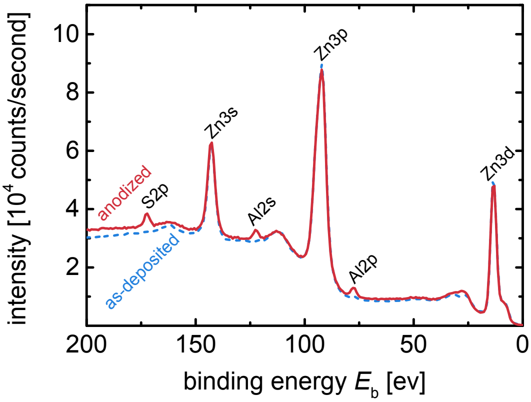

Fig. 6.18. XPS spectra of an as-deposited and an anodized ZnO:Al thin film. Electrochemical anodization was performed in 0.1 M K_2SO_4 at $E = 2.1$ V vs. Ag|AgCl|3 M KCl. The peaks are labeled with the corresponding orbitals. In the as-deposited state, peaks corresponding to Zn, O, Al, and C were detected. After anodization S and Cl lines were additionally measured. Relative quantitation is listed in Table 6.1.

When the anodic current was switched off again, the concentration of Al and Zn leveled off at the same values as initially observed at OCP. The suppressed Al dissolution is surprising at first glance. Fig. 6.17b depicts a measurement with potential steps between -0.5 V ($\approx OCP$) and moderate anodic potentials of 0.5 and 1.0 V, respectively, where no electrochemical zinc oxide decomposition was observed. This is confirmed by the constant [Zn] signal. Still, the Al dissolution is suppressed even at these comparably low bias potentials. However, after returning to a potential close to OCP more Al is dissolved than initially observed. This observation indicates that Al was initially dissolved with the ZnO matrix but precipitated at the samples surface when an anodic bias was applied, presumably as an oxidized compound, and was thus not found in the solution. However, at OCP it seems to be soluble.

X-ray photoelectron spectroscopy (XPS), a surface sensitive method allowing for the determination of the chemical composition of a sample was used to prove the hypothesis of Al precipitation at the surface. An as-deposited ZnO:Al thin film was compared to a sample, which was electrochemically anodized in 0.1 M K_2SO_4 at $E = 2.1$ V vs. Ag|AgCl|3 M KCl until a charge of $q = 119\,\mathrm{mC\,cm^{-3}}$ was exchanged. The measured spectra are plotted in Fig. 6.18. The measurement of the as-deposited ZnO:Al thin film is displayed as a dashed line while the anodized samples is plotted as a solid line. Apparently, the peak intensities changed slightly upon anodization. The Zn peaks decreased while the Al peaks increased and an S2p peak is introduced. A relative quantification of the elemental composition of the sample surfaces was performed by fitting Gaussian shaped functions into the spectrum at known binding energies [309]. The results in atomic percent are listed in Table 6.1.

Table 6.1. Relative quantification of the chemical composition of ZnO:Al surface layers determined by fitting Gaußcurves into XPS peaks for an as-deposited sample and a sample which was anodized in 0.1 M K_2SO_4 at a potential of $E = 2.1$ V vs. Ag|AgCl|3 M KCl until a charge of 118.5 mC cm^{-2} was exchanged. The chemical composition changes upon anodization. Further discussion can be found in the text.

Peak (Orbital)	as-deposited ZnO:Al at. %	anodized ZnO:Al at. %
O1s	41.1	53.0
Zn2p	45.6	34.2
C1s	12.7	9.2
Al2p	0.6	2.2
S2p	-	1.2
Cl2p	-	0.2

Indeed, the suggested enrichment of Al at the surface during electrochemical anodization was confirmed by the results. The Zn concentration decreased while O and Al concentration increased. Additionally carbon, presumably adsorbed from ambient air, was found on both samples. Sulfur and chlodine on the anodized sample stem from the K_2SO_4 electrolyte and the Ag|AgCl|3 M KCl reference electrode. Further measurements using secondary ion mass spectroscopy (SIMS) confirmed an accumulation of Al on the anodized ZnO:Al surface (not shown here).

6.4. Discussion

The anodic dissolution of ZnO proceeds via electrochemical lattice decomposition (reaction (6.1)) and via OER (reaction (6.2)) and subsequent chemical dissolution (reaction (6.3)). The share of the individual pathways is experimentally not easily accessible. However, close to the onset potential of anodic current the significance of direct lattice decomposition is probably highest while the OER becomes more important with increasing potential. This is due to the fact that the potential for decomposition is below the standard potential of water oxidation [155].

To understand the underlying mechanism of the dissolution process, it is useful to study the electronic states in the ZnO and at the ZnO/electrolyte interface, since they play a decisive role in the process [5]. The observation that holes control anodic processes at semiconductor electrodes was already stated in one of the first papers on the electrochemical behavior of semiconductors by Brattain and Garret [310]. They found that *p*-type Ge is easily oxidized in contact with electrolytes while *n*-type Ge needs illumination. Indeed, the concentration of holes at the surface controls the anodic reaction rate on various semiconductors such as Si [311], GaAs [312], GaP [313], CdS [314] and ZnO [5, 6, 154]. From a chemical point of view, a hole at the semiconductor surface entails a missing electron in a bonding orbital and hence a weakened or broken bond. Consequently, semiconductors tend to dissolve when holes are present at the surface. The increased anodic current density upon illumination with light of a frequency ν with h$\nu \geq E_\mathrm{g}$ (see Fig. 6.16) is clear evidence of this process. A schematic illustration of the ZnO:Al under illumination is depicted in Fig. 6.19. Electrons are excited to the conduction band by light absorption leaving

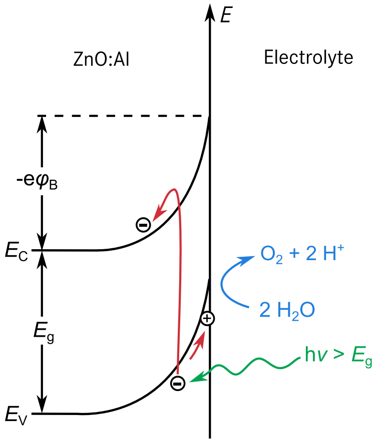

Fig. 6.19. Schematical energy diagram of the ZnO:Al/electrolyte interface under illumination with photon energies $E_\mathrm{phot} > E_\mathrm{g}$. The band bending in the space charge region separates the generated charge carriers and prevents recombination. Due to the electric field the holes drift to the ZnO:Al/electrolyte interface where they can trigger electrochemical lattice decomposition or the OER.

behind holes in the valence band. The generated charge carriers are separated by the electric field present in the space charge layer. Thus, recombination is prevented. In the depletion layer in the ZnO the electrons will move towards the ZnO bulk, while the holes will drift to the ZnO/electrolyte interface where they can accept electrons from a reduced species with suitable energy. Consequently, the dissolution of the ZnO lattice proceeds via reactions (6.1 - 6.3).

Further details on the dissolution of compound semiconductors can be found in the literature [5]. As mentioned before, for *n*-type semiconductors only anodic dissolution under illumination is reported to be possible due to the mentioned lack of holes at the surface in the dark. In contrast, the investigations reported in this thesis show, that anodic dissolution of degenerately doped ZnO:Al is possible without illumination at anodic potentials above $E \approx 1.2\,\mathrm{V}$ vs. Ag|AgCl|3 M KCl. Thus, the origin of holes at the ZnO:Al/electrolyte interface has to be clarified. Furthermore, the reason for the selectivity of the dissolution process to the grain boundaries needs explanation. Therefore, the charge transfer at the polycrystalline ZnO:Al/electrolyte interface will be discussed in detail.

6.4.1. Charge Transfer

It was observed in Fig. 6.1, that ZnO:Al thin films exhibit a blocking character over an extended potential region. Pettinger *et al.* found that this blocking behavior of zinc oxide crystals decreases for increasing doping concentration [145]. For crystals with doping concentrations as low as $N_\mathrm{D} = 10^{16}\,\mathrm{cm}^{-3}$, the blocking region can extend up to 30 V vs. SHE and higher. In principle, the onset potential of the anodic current depends on the electric field strength F_s at the surface of the electrode. This field should be proportional to the square root of the product of the donor density N_D and the potential drop φ_sc in the space charge layer of the semiconductor [315],

$$F_\mathrm{s} = \sqrt{\frac{2\,\mathrm{e}\,N_\mathrm{D}}{\varepsilon_0\varepsilon_\mathrm{r}}\left(\varphi_\mathrm{sc} - \frac{\mathrm{k_B}T}{e}\right)}. \tag{6.7}$$

Thus, for higher donor concentrations, N_D, a lower potential drop is needed to provide the field strength sufficient for the onset of anodic currents.

Since both anodic onset potential and flat band potential were measured (see Fig. 6.2), the electronic conditions at the ZnO/electrolyte interface are determined. The potential drop and thus the band bending in the semiconductor $|\mathrm{e}\,\varphi_\mathrm{sc}|$ can be calculated from the difference between the electrode potential E and the flat band potential E_{fb} [150]. Hence, at the onset potential E_{onset} a band bending of

$$|\mathrm{e}\,\varphi_{\mathrm{sc}}| = \mathrm{e}\,(E_{\mathrm{onset}} - E_{\mathrm{fb}}) = 1.287\,\mathrm{eV} + 1.916\,\mathrm{eV} = 3.203\,\mathrm{eV} \tag{6.8}$$

is present. Within the measurement error this value corresponds well to the band gap of ZnO. Please note that the flat band potential of ZnO depends on the pH value of the electrolyte [6, 145]. Thus the flat band potential which was determined in a $NaClO_4$ solution containing propylene carbonate as an electrolyte might deviate slightly from the value in an aqueous electrolyte. This result is in accordance with the findings of Pettinger *et al.* [145] that the anodic current beyond the onset starts when the band bending exceeds the band gap of ZnO. Thus, hole generation by band to band tunneling is suspected to be responsible for the charge transfer and consequent dissolution of the ZnO:Al thin film via reactions (6.1 - 6.3). This is schematically illustrated in Fig. 6.20. Direct band to band tunneling (3) is possible

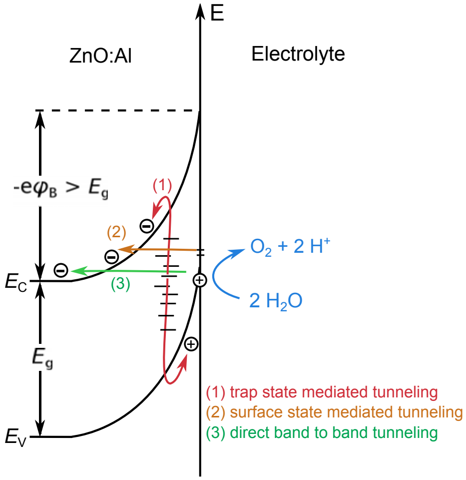

Fig. 6.20. Band diagram of the ZnO:Al/electrolyte interface under anodic polarization. The band bending in the space charge region exceeds the band gap of ZnO, $-\mathrm{e}\varphi_{\mathrm{B}} > E_{\mathrm{g}}$. This enables band to band tunneling (3). Further processes allowing electron injection into the conduction band are tunneling via trap states in the space charge region (2) and surface state mediated tunneling (1). Each of the processes provides holes at the ZnO:Al/electrolyte interface which are able to drive direct lattice decomposition or oxygen evolution.

for highly doped semiconductors when the band bending exceeds the band gap of the semiconductor. Additionally, hole generation via trap states in the space charge layer (1) and surface states (2) might contribute to the anodic current. Each of the described tunneling processes provides holes at the ZnO:Al/electrolyte interface for oxidation reactions.

Defect state mediated processes are more likely to play a role at the grain boundaries due to a higher concentration of trap states at these sites. Furthermore, trap states may alter the electric field strength at the sites where the grain boundaries encounter the ZnO/electrolyte interface. This can be understood on the basis of a model developed by Seto for polycrystalline semiconductors [90]. The band diagram of polycrystalline, degenerately doped ZnO in x-direction (perpendicular to the surface normal) according to Seto's model is depicted in Fig. 6.21a. The trap state density N_t at the grain boundaries introduces a symmetrical potential barrier Φ_{gb} at each grain boundary. The Fermi level E_F (dashed line) lies above the conduction band edge E_C in the grain interior but is pinned at the grain boundaries due to the trap states leading to a depletion layer in the vicinity of the grain boundaries. This is depicted in Fig. 6.21b showing the ZnO:Al/electrolyte interface. The pinning of the Fermi level at the grain boundaries dashed lines results in a narrower space charge region and an enhanced electric field at the interface. This is in accordance with the findings of Rau and Werner who showed, by analytical calculations, that tunneling across a Schottky barrier is enhanced by grain boundaries [317] in the

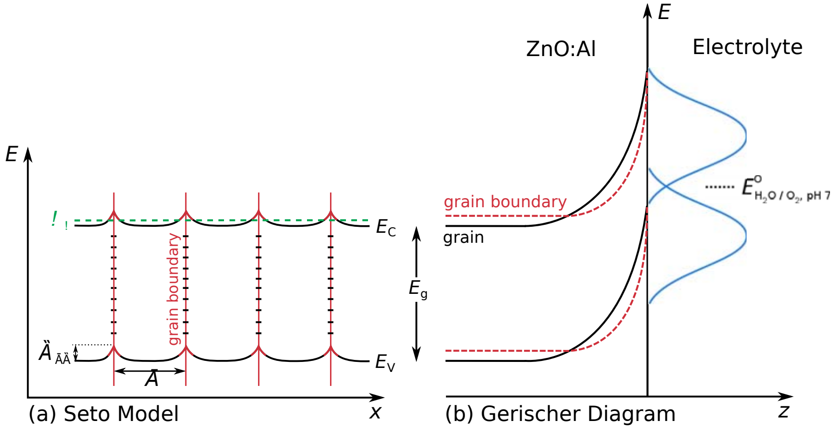

(a) Seto Model (b) Gerischer Diagram

Fig. 6.21. (a) Seto model for polycrystalline ZnO:Al [90]. (b) Gerischer diagram [316] of the ZnO:Al/electrolyte interface.

case of completely depleted grains. They found that the maximum electric field at the rectifying contact is present at the grain boundaries. Consequently, the charge transfer by tunneling occurs mainly at the grain boundaries. This equally applies to other rectifying contacts such as the polycrystalline semiconductor/electrolyte contact investigated here and explains the observed pronounced selectivity of the dissolution process to the grain boundaries.

6.4.2. Influence of the Anion Species

The preferred conditions for charge transfer and hence anodic dissolution are independent of the used electrolyte species. However, after the initial dissolution event, the etching progresses differently, depending on the present anion, as reflected in the current density transients during anodization (Fig. 6.7), the etched structures (Fig. 6.8), and the electrical and optical properties (Fig. 6.10 and Fig. 6.11) of the anodized ZnO:Al films. Deviating densities of defect states and differing resulting electric fields can hardly explain the effect of the different anion species. However, the anodic dissolution in K_2SO_4 clearly deviated from the other electrolytes use. Abd El Aal *et al.* [285] reported that sulfate ions, which are electrochemically inert under the applied potentials, act as destabilizing species for passive films on zinc electrodes. This is also confirmed by Klemm *et al.* [294]. The higher anodic current densities at equal bias potentials observed in K_2SO_4 (see Fig. 6.7) might be related to the fact that the SO_4^{2-} ions adsorb on the electrode surface and subsequently participate in the active dissolution process [295]. Adsorption of SO_4^{2-} anions on the oxide film creates an additional electrostatic field across the ZnO/electrolyte interface [318]. In passive films on zinc electrodes, adsorbed anions are suggested to penetrate the oxide film when the electric field is sufficiently strong, especially at defects, and to promote local anodic dissolution [319]. In general, adsorption of ions on the ZnO:Al surface can establish surface dipoles which might influence the space charge region close to the semiconductor-electrolyte interface. Also formation or compensation of surface defects by adsorbed ions is conceivable [320]. However, the polycrystalline nature of the investigated thin films makes quantitative statements about the adsorption of different species difficult. An effect of the chemical nature of the anions on electrochemical deposition of ZnO is also observed on the electrochemical deposition of zinc oxide [244]. It is found that the aspect ratio of electrodeposited nanorods is significantly lower in Cl^- than in SO_4^{2-} solutions. This is attributed to an even higher ability of the chloride ions to adsorb at the ZnO surface. Furthermore, Zn^{2+} ions probably form ion pairs with SO_4^{2-} [321] which are assumed to decrease the activation energy for zinc dissolution and thus increase the dissolution current [298]. However, also NO_3^- and Cl^- containing solutions are known to enhance pitting corrosion [260, 322].

Moreover, the polycrystalline structure of ZnO:Al thin films requires to take into account that the dissolution proceeds in grooves of growing depth along the grain boundaries. Thus, local saturation of the solution and as a result, inhibition of dissolution might become an issue. However, this effect is not expected to be of major influence because, even in solutions saturated with the zinc salt, the dissolution process continues [153]. Nevertheless, a high aspect ratio between the depth and the width of the grooves limits transport processes and leads to a significant enrichment of dissolved zinc during etching. However, the complex interplay between pore formation and diffusion in the evolving porous material goes beyond the scope of this work. As reported by Gerischer and Sorg [153] the influence of the anion on the chemical dissolution rate of ZnO single crystals follows the tendency to form complexes with Zn^{2+} ions and increases from NO_3^- to Cl^- and then SO_4^{2-}. Thus, the dissolution rate is probably influenced by the rate at which zinc complexes diffuse away from the electrode surface [321]. This trend is in accordance with the present experiments. However, this explanation cannot account for the different structures and the higher lateral dissolution rate that was observed in Cl^-, NO_3^-, and ClO_4^- containing solutions as compared to ${SO_4}^{2-}$. One aspect could be that some electrolyte constituents are week electrolytes, with protons involved in the dissociation process. A buffer effect therefore results from the ability to liberate or consume protons in the pH dependent chemical equilibrium. In fact, we suggest different pH values in the direct vicinity of the electrode to be the reason for the differing evolving structures. As a result of the OER, the acids corresponding to the salts are formed directly at the ZnO:Al surface according to equations (6.9) - (6.13). The corresponding pK_a values were taken from Ref. [323] and [57].

$$
\begin{aligned}
{ClO_4}^- + H^+ &\rightleftharpoons HClO_4 & pK_a &= -10 & (6.9)\\
Cl^- + H^+ &\rightleftharpoons HCl & pK_a &= -7 & (6.10)\\
{NO_3}^- + H^+ &\rightleftharpoons HNO_3 & pK_a &= -1.4 & (6.11)\\
{SO_4}^{2-} + H^+ &\rightleftharpoons {HSO_4}^- & pK_a &= +1.987 & (6.12)\\
{HSO_4}^- + H^+ &\rightleftharpoons H_2SO_4 & pK_a &= -3 & (6.13)
\end{aligned}
$$

The chemical behavior of the respective acids is different. First of all, H_2SO_4 is a diprotic acid in contrast to $HClO_4$, HCl, and HNO_3. In the sulfate solution HSO_4^- is formed as a first step and a buffer of SO_4^{2-}/HSO_4^- builds up. A reasonable buffering concentration of 10^{-2} M is already sufficient to maintain the local *p*H at the electrode at the bulk value at reaction rates up to $1\,\mathrm{mA\,m^{-2}}$ whereas in unbuffered systems the local *p*H can deviate from the bulk value by several numbers [324]. The *p*H shift might be even more pronounced during the course of the dissolution process due to the confinement in the dissolved grain boundaries. However, the buffering effect of the SO_4^{2-}/HSO_4^- system may lead to a less acidic local *p*H at the interface as compared to the unbuffered systems. Therefore, the dissolution process in the etch pits propagates along the grain boundaries because the potential for OER is present, while the chemical dissolution of the grains due to a further *p*H shift is inhibited. This explains the observation of deep and narrow etching features in K_2SO_4 containing solutions whereas in KCl, KNO_3, and $KClO_4$, where no buffer effect is present, the local *p*H in the etched grain boundaries probably undergoes much stronger shifts. Thus, additional chemical etching occurs in the channel leading to a collateral dissolution of the ZnO:Al grains.

6.4.3. Influence of the solution pH

The decreasing dissolution rate in phosphate buffer solutions when the *p*H is increased from 5.5 to 6.5 and the low relatively stable dissolution rate between 6.5 and 7.5 (see Fig. 6.13a and Fig. 6.14) is in accordance with expectations with respect to the thermodynamic stability of zinc oxide which is graphically represented in the Pourbaix diagram (Fig. 3.5).

In contrast, the increasing dissolution rate in alkaline solutions of *p*H 8.45 to 10.25 (see Fig. 6.13b and Fig. 6.14) is surprising at first glance because thermodynamics predict relative stability of ZnO in this *p*H range. However, in alkaline solutions oxidation of hydroxide via

$$4\ \mathrm{OH^-} \rightleftharpoons \mathrm{H_2O} + \mathrm{O_2} + 4\ \mathrm{e^-} \tag{6.14}$$

may compete with lattice decomposition and OER. This reaction has a standard potential of $E^\circ = 0.178\,\mathrm{V}$ vs. Ag|AgCl|3 Molar KCl. In contrast to the OER, protons are not produced. Thus, the reaction discriminates both chemical dissolution and electrochemically triggered dissolution by consumption of OH^- and holes, respectively. Therefore, the increasing charge density with increasing *p*H in borax buffer solutions may not necessarily reflect an increased amount of decomposed zinc oxide.

6.4.4. Applicability of Electrochemically Anodized ZnO:Al to Solar Cells

The opto-electronic properties of anodically surface textured ZnO:Al thin films were studied. The surface texture exhibits very fine surface features which are not sufficient for light scattering purposes in thin-film solar cells. However, the absorptance in the wavelength range $\lambda > 600\,\mathrm{nm}$ decreased considerably upon anodic treatment. This effect was ascribed to a decreased charge carrier concentration which also expresses itself in a decreased Burstein-Moss shift. The sheet resistance of the thin films increased during the dissolution process. However, comparably short anodic polarization led to acceptable R_{sh} values below $10\,\Omega$ and a considerable decrease of the near infrared absorptance. Therefore, the combined approach of traditional chemical texturing with the presented anodic treatment might offer a promising method to benefit from the light scattering of the chemical texture and the improved transmittance of the anodic texture. This approach is pursued in the following chapter.

6.5. Summary

Anodic dissolution was utilized to deliberately introduce a new type of surface texture to polycrystalline ZnO:Al thin films exhibiting fine surface features along the grain boundaries. The mechanistic understanding of the anodic dissolution of polycrystalline ZnO thin films was extended considerably. The mechanism of the charge transfer via band to band tunneling, which might be enhanced by trap or interface states, was found to be responsible for the breakdown of the anodic blocking behavior of highly doped ZnO thin films. The generation of minority charge carriers within the space charge region of the ZnO:Al electrode clearly support the suggestion that charge transfer occurs between the valence band and reduced species in the electrolyte. The origin of the selective dissolution of the grain boundaries was explained by a field enhancement at these sites due to the presence of defect states.

The observed effect of the anion species and the pH of the electrolyte were studied and explained based on the interfacial pH in the close vicinity of the electrode.

Furthermore, the opto-electronic properties of the anodically treated ZnO:Al thin films were comprehensively investigated and an increase of the transmittance in the infrared range was found. This findings provide a basis for an improvement of the light management in Si thin-film solar cells.

7. Integration of Electrochemically Textured ZnO:Al Layers into Thin-Film Silicon Solar Cells

In chapter 6 promising trends upon electrochemical anodization of ZnO:Al thin films in terms of their optical properties were observed. These findings encouraged the application of the electrochemical anodic texturing to front contacts used in silicon thin-film solar cells. However, sufficient light scattering is not provided by the purely electrochemically textured ZnO:Al surfaces. Thus, this chapter reports results on sequential texturing processes that combine chemical and electrochemical texturing. The experimental conditions are described in section 7.1. Section 7.2 provides results on a surface texture with features of two lateral sizes and section 7.3 presents an approach to tune the feature size of surface textured ZnO:Al thin films. Both types of surface textures were investigated in terms of their usability for microcrystalline silicon single junction solar cells.[1]

7.1. Experimental

Approximately 800 nm thick, polycrystalline ZnO:Al thin films were deposited on cleaned 10 cm × 10 cm glass substrates (Corning Eagle XG) using radio frequency (RF) magnetron sputtering. Details on the deposition system and process can be found in section A.1.1.

The ZnO:Al-covered substrates were cut into 5 cm × 5 cm pieces, which were then textured. In the case of anodic texturing the samples were connected as the working electrode in an electrochemical cell. The temperature was kept constant at 25 °C during all electrochemical and chemical experiments. Details on the electrochemical setup are reported in section A.3. After the electrochemical treatment the samples

---

[1] Some of the results presented in this chapter were published in S. E. Pust, J.-P. Becker *et al.*, *J. Electrochem. Soc.* (2011), 158(7), D413-D419

were cleaned in hot, deionized water to remove salt residues originating from the electrolyte solution.
Characterization of the ZnO:Al thin films was performed using a surface profiler (section A.4.1), scanning electron microscopy (section A.4.5), van der Pauw measurements (section A.4.4), and UV-VIS-NIR Photospectroscopy (section A.4.2).

Silicon films were prepared by plasma enhanced chemical vapor deposition (PECVD). Details can be found in section A.2. The crystalline volume fraction was determined evaluating Raman spectra as reported in Ref. [325–327]. Therefore, a blue laser ($\lambda = 488\,\mathrm{nm}$) was used to probe the silicon layer through the glass/ZnO:Al substrate providing a small penetration depth and thus probing the silicon close to the front contact, in the initial growth regime.

The solar cell back contact consisted of an approximately 80 nm thick ZnO:Al layer, sputter-deposited at room temperature in the same system as the front contacts, and 700 nm silver, deposited by thermal evaporation through a mask to determine cells of 1 cm × 1 cm. Thereby, six solar cells were defined on each sample for further characterization. A schematic illustration of the solar cell layer stack is depicted in Fig. 7.1. Solar cells were characterized under standard test conditions with a solar simulator described in section A.5.2. Quantum efficiencies were measured by differential spectral response (DSR) at zero bias (section A.5.1).

7.2. Combined Texturing

Surface texturing by means of electrochemical anodization was found to decrease the absorptance of ZnO:Al thin films in the near infrared spectral range (see chapter 6). However, the small features located in the close vicinity of the grain boundaries are lacking efficient light scattering, which is crucial for thin-film solar cells to enhance the optical path length through the silicon absorber material and consequently increase the probability of light absorption and generation of charge carriers. Light scattering is particularly important in the long wavelength range because the absorption of Si layers is low in this range. Therefore, this work introduces a sequential process, combining chemical and electrochemical etching to conjoin the advantages of both kinds of surface textures.

The surface texture achieved by purely chemical etching in diluted HCl represents a high quality reference within this study. It is optimized and known to be well suited for light scattering purposes in Si thin-film solar cells [22, 29]. Fig. 7.2a shows

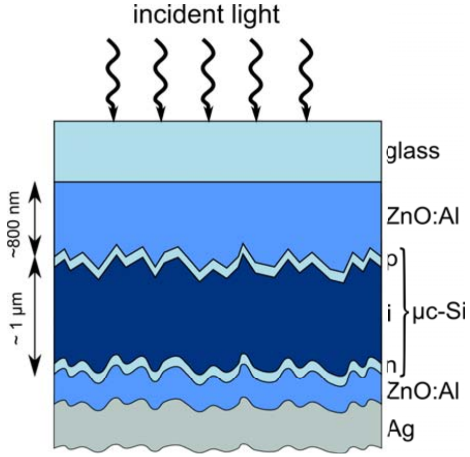

Fig. 7.1. Schematic illustration of a microcrystalline silicon thin-film solar cell. The deposition of the depicted material stack is performed from top to bottom. The ZnO:Al thin film is sputter-deposited on the glass substrate and subsequently textured. The doped and intrinsic microcrystalline silicon layers were deposited by plasma enhanced chemical vapor deposition. The back contact is again sputter-deposited and consists of an approximately 80 nm thick ZnO:Al layer and an approximately 700 nm thick silver layer. Please note that the layer thicknesses are not in scale.

an SEM image of a typical surface texture obtained by an optimized etching step in 0.154 M HCl for 40 s. The surface texture depicted in Fig. 7.2b was prepared by the same chemical etching process but with additional electrochemical polarization at $E = +2.0\,\mathrm{V}$ vs. Ag|AgCl|3 M KCl in 0.1 M KCl subsequent to the conventional chemical etching step. Both treatments were performed at $T = 25\,°\mathrm{C}$. The two step process apparently led to the superposition of the crater-shaped features resulting from the chemical etching and the fine grain boundary texture from electrochemical anodization. We will thus call it combined texture hereafter. During chemical etching the sheet resistance increased from $R_{\text{sh,as-depo.}} = 3.1\,\Omega$ to $R_{\text{sh,ref.}} = 6.5\,\Omega$. After additional anodization the sheet resistance was measured as $R_{\text{sh,dual}} = 9.2\,\Omega$. Interestingly, the high selectivity of the anodic dissolution process to the grain boundaries is not influenced by the chemical pretreatment of the ZnO:Al layer.

For prolonged anodic treatment the sheet resistance of the combined textured ZnO:Al thin films increased similar to those without a chemical pretreatment, as described in chapter 6. The evolution of the sheet resistance of combined textured

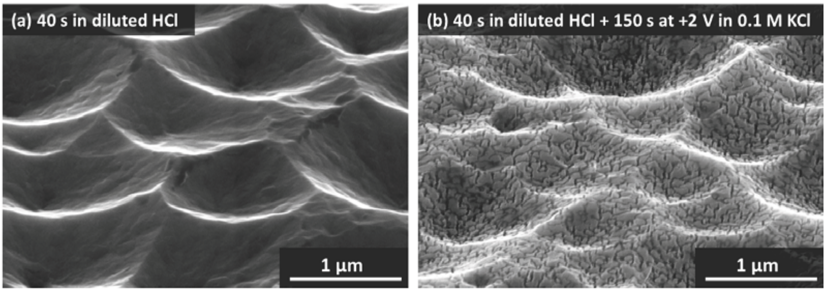

Fig. 7.2. SEM images of ZnO:Al surfaces recorded with a tilt of the surface normal of 50°. The sample depicted in (a) was chemically etched for $t = 40\,\mathrm{s}$ in $0.154\,\mathrm{M}$ HCl (0.5 w/w%). The sheet resistance after etching was $R_{\mathrm{sh}} = 6.5\,\Omega$. The combined texture depicted in (b) was achieved by a similar treatment for $t = 40$ s in $0.154\,\mathrm{M}$ HCl and subsequent anodization in $0.1\,\mathrm{M}$ KCl at $E = +2.0$ V vs. Ag|AgCl|3 M KCl until a charge of $q = 73\,\mathrm{mC\,cm^{-2}}$ was exchanged at the electrode. Thereby the sheet resistance was increased to $R_{\mathrm{sh}} = 9.2\,\Omega$. During texturing the temperature was maintained constant at $T = 25\,°\mathrm{C}$.

ZnO:Al, as measured using van der Pauw measurements, is plotted vs. the exchanged charge in Fig. 7.3a. The effective layer thickness of the material dissolved during anodization is displayed at the upper x-axis. The impact of further anodic etching on the resistance of the layer increases during the process.

At the same time the transmittance in the spectral range relevant for Si thin-film solar cells ($\lambda \approx 300 - 1100\,\mathrm{nm}$) is increased significantly. This can be observed in Fig. 7.3b which shows the total and diffuse transmittance of combined textured ZnO:Al thin films. The color coding is the same as in Fig. 7.3a. The total transmittance T_{t} of the sample exposed to the longest anodic treatment (◆/dotted) increased more than 10 % over the whole spectral range with respect to the reference. But a comparatively short anodic treatment with little effect on the sheet resistance (●/dashed) already enhanced the transmittance considerably. A large portion of the increase in the wavelength range from 400 - 800 nm is due to the increasing diffuse transmittance. In contrast, the increased transmittance in the long wavelength range is mainly caused by direct transmittance. Thus, the surface features introduced by electrochemical anodization mainly interact with light of short wavelengths due to their small dimensions while the increased transmittance in the long wavelength range is presumably due to removal of material and a reduced charge carrier concentration due to partially depleted grains resulting from the formation of surface defects.

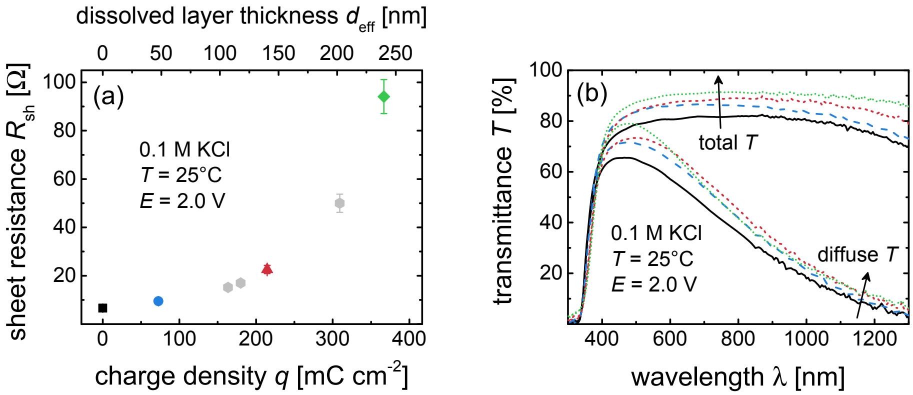

Fig. 7.3. (a) Sheet resistance of combined textured ZnO:Al thin films plotted vs. charge exchanged during anodization in 0.1 M KCl at constant potential of $E = +2.0$ V vs. Ag|AgCl|3 M KCl in 0.1 M KCl. Before anodization all samples were chemically textured by etching for 40 s in 0.154 M HCl. The temperature during both texturing steps was maintained at $T = 25$ °C. Sheet resistances were determined using van der Pauw measurements. (b) Transmittance spectra of four ZnO:Al thin films combined textured by sequential etching. First chemical etching in 0.154 M HCl for $t = 40$ s and subsequential electrochemical anodization at a potential of $E = +2.0$ V vs. Ag|AgCl|3 M KCl in 0.1 M KCl. The temperature during etching was $T = 25$ °C. The total and diffuse transmittances are displayed. The solid lines represent the reference which was not electrochemically treated. The other lines are color coded with respect to (a) and Fig. 7.4 ($q = 73,\ 214,\ 367\,\mathrm{mC\,cm^{-2}}$).

The spectrally resolved absorptance of combined textured ZnO:Al thin films is depicted in Fig. 7.4a. Diidomethane was used as an index matching solution (see section A.4.2) and the absorptance was calculated via equation (2.12) from reflectance and transmittance data. A strong decrease in the near infrared spectral range with increasing exchanged charge q during anodization is apparent. This is in accordance with the behavior observed in chapter 6 and is ascribed to a decreased charge carrier concentration because the absorptance decreases faster than the removal of material suggests. Another indication for a decreasing charge carrier concentration is the decrease in the optical band gap E_g from 3.61 eV to 3.38 eV as depicted in Fig. 7.4b. This behavior cannot be explained by the removal of material but by a reduced Burstein-Moss shift due to a decreased charge carrier concentration in the ZnO:Al films (see section 2.2.3). This was also observed for electrochemically anodized ZnO:Al thin films (chapter 6).

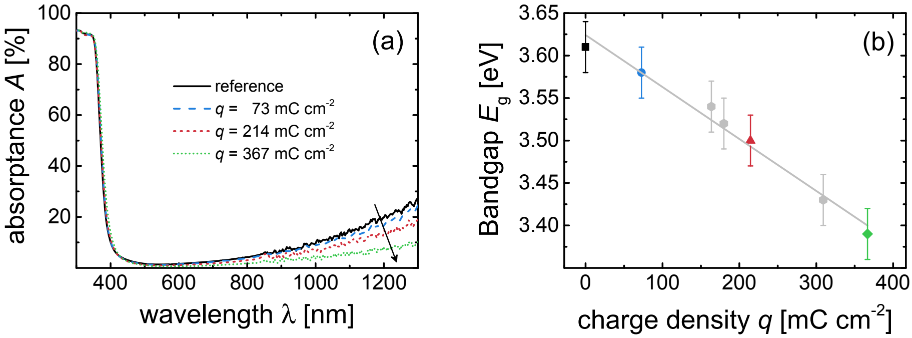

Fig. 7.4. (a) Spectrally resolved absorptance of combined textured ZnO:Al thin films. The absorptance was calculated via equation (2.12) from reflectance and transmittance data measured by means of a photospectrometer. The measurements were conducted using diiodomethane as an index matching medium to prevent light trapping in the glass substrate. All samples were initially etched in 0.154 M HCl for $t = 40$s. Exept for the reference sample (solid line) a subsequent anodic polarization step at $E = +2.0$ V vs. Ag|AgCl|3 M KCl was applied with differing exchanged charges (see legend). The color coding is the same as in (a) and in Fig. 7.3. The temperature during both etching steps was maintained at $T = 25$ °C. (b) Optical band gap energies E_g of ZnO:Al thin films after a two step treatment consisting of a chemical texturing step of 40 s in 0.154 M HCl and a subsequent anodization step in 0.1 M KCl. Both treatments were conducted at $T = 25$ °C. The color coding is the same as used in Fig. 7.3.

In general, the observed properties of the combined textured ZnO:Al thin films, are promising with regard to the application in silicon thin-film solar cells. An exception is the higher sheet resistance with respect to the reference which might result in an increased series resistance in solar cells. To test if the optical improvements translate into enhanced solar cell performance, microcrystalline silicon (µc-Si:H) solar cells were fabricated using combined textured ZnO:Al thin films as front contacts. The electrochemical anodization was kept relatively short to minimize ohmic losses due to an excessive increase of the sheet resistance. The solar cell stack used in this investigation is schematically illustrated in Fig. 7.1.

Optical losses in solar cells mainly affect their current density. The quantum efficiency allows to study the current density in spectral resolution. Fig. 7.5a depicts both external quantum efficiencies EQE and absorptances $(1 - R)$ of four solar cells featuring combined textured ZnO:Al front contacts. All solar cells were deposited in one run. The only variable is the exchanged charge during anodic surface texturing. An improved light incoupling by the small surface features was expected due to an effective refractive index grading between ZnO:Al and Si. Furthermore, a higher quantum efficiency in the long wavelength range due to the lower absorptance of the ZnO:Al might be expected. Both trends are visible in the EQE. However, the solar cell absorptance is relatively unaffected by the anodic texturing over a wide spectral range. A relevant deviation from the reference (solid line) was only observed in the near infrared range. Moreover, the solar cells deposited on ZnO:Al front contacts with a longer anodic treatment seem to reflect more light in this wavelength range. Nevertheless, more charge carriers are generated and separated.

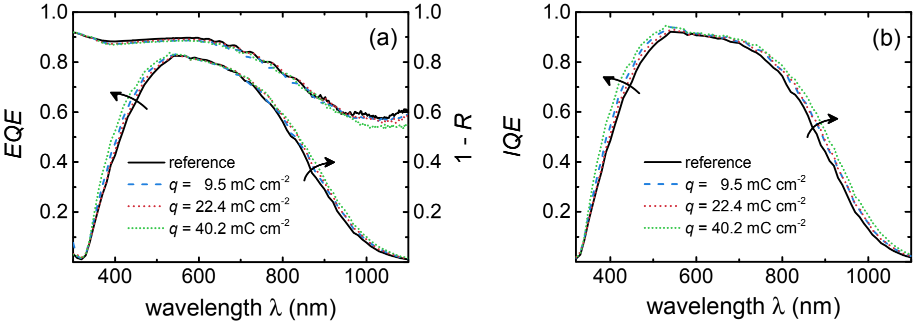

Fig. 7.5. (a) External quantum efficiencies and reflectances of microcrystalline Si thin-film solar cells deposited on ZnO:Al front contacts with differing combined textures achieved by sequential chemical and electrochemical texturing in 0.154 M HCl and 0.1 M K_2SO_4, respectively. The anodic treatment time was varied such that charges of 9.5, 22.4, and 40.2 $\mathrm{mC\,cm^{-2}}$ were exchanged. (b) Corresponding internal quantum efficiencies IQE.

This trend is even more pronounced when the internal quantum efficiency $IQE = EQE/(1 - R)$, as plotted in Fig. 7.5b, is considered. The IQE only takes into account photons which are absorbed in the solar cell, *i.e.* light incoupling and reflection losses are not considered. The fact that anodic texturing results in a globally increased IQE without a decrease in the solar cell reflectance indicates differences in the silicon layer properties. Therefore, Raman spectroscopy was used to determine the crystalline volume fraction of the silicon layers close to the ZnO:Al/Si interface, *i.e.* where the Si growth initiates. Indeed, the crystallinity of the silicon phase increased from 50.9 % for the reference to 65.9 % for the longest anodic treatment. The values are plotted in Fig. 7.6b.

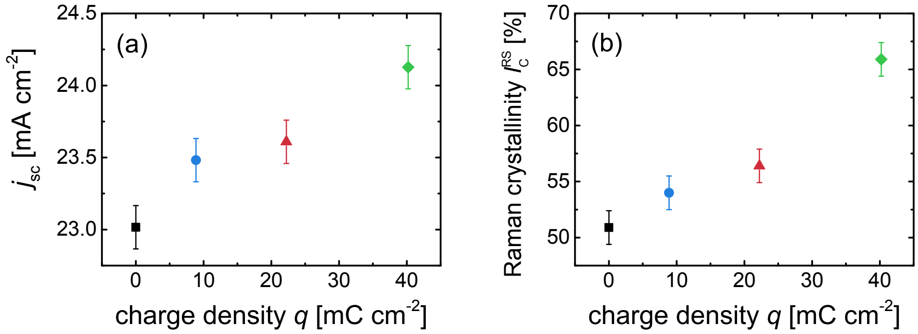

Fig. 7.6. (a) Short-circuit current density j_{sc} of μc-Si:H single junction solar cells vs. charge density exchanged during electrochemical anodization of the ZnO:Al front contacts. The values were calculated by convolution of quantum efficiencies plotted in Fig. 7.5 with the AM1.5g solar spectrum. (b) Raman crystallinity I_C^{RS} of the silicon layers in the vicinity of the ZnO:Al/μc-Si:H interface vs. charge density exchanged during electrochemical anodization of the ZnO:Al front contacts.

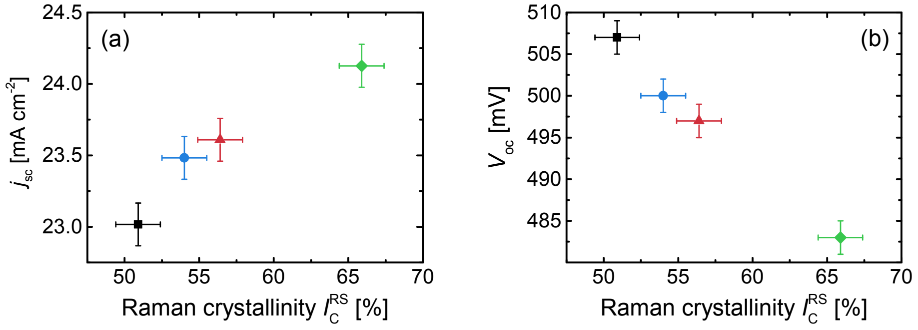

Fig. 7.7. Short-circuit current densities j_{sc} as determined from EQE (a) and open-circuit voltages V_{oc} (b) of μc-Si:H single junction solar cells plotted vs. the crystalline volume fraction of the silicon layer close to the combined textured ZnO:Al front contact. V_{oc} values were extracted from current-voltage measurements under an AM1.5g solar spectrum.

Additionally, the short-circuit current densities j_{sc} of the solar cells obtained by convolution of the EQE with the solar spectrum are plotted in Fig. 7.6a. An approximately linear increase with prolonged anodic treatment was observed for both current density and crystallinity of the silicon layers. Thus, the reason for the observed variation of the short-circuit current density and the quantum efficiency may be the higher crystallinity of the silicon layers. Fig. 7.7 supports this presumption. It plots short-circuit current density j_{sc} and open-circuit voltage of µc-Si:H single junction solar cells featuring combined textured ZnO:Al front contacts vs. the transferred charge during anodization. In contrast to the short-circuit current density, the open-circuit voltage decreases as the silicon crystalline volume fraction increases.

This behavior can be understood considering the dependence of V_{oc} on the band gap E_{g} of the silicon,

$$V_{\mathrm{oc}} \approx \frac{n_{\mathrm{id}}\,\mathrm{k_B}\,T}{\mathrm{e}} \ln\left(\frac{j_{\mathrm{sc}}}{j_0}\right) = \frac{E_{\mathrm{g}}}{\mathrm{e}} - \frac{\mathrm{k_B}\,T}{\mathrm{e}} \ln\left(\frac{j_{00}}{j_{\mathrm{sc}}}\right). \tag{7.1}$$

Here $\mathrm{n_{id}}$ is the ideality factor of the diode, $\mathrm{k_B}$ is the Boltzmann constant, T is the temperature, e is the elementary charge, j_0 is the dark saturation current density, and j_{00} is a prefactor of the dark saturation current according to

$$j_0 = j_{00} \exp\left(-\frac{E_{\mathrm{g}}}{\mathrm{k_B} T}\right). \tag{7.2}$$

The crystallinity of Si thin films can be altered by the silane to hydrogen ratio in the plasma chamber during deposition. Optimum solar cell performance is usually obtained for µc-Si:H grown in a narrow process window close to the phase transition to amorphous silicon [328]. This material is composed of a crystalline phase embedded in an amorphous matrix. The amorphous silicon phase (a-Si:H) has a band gap of approximately 1.7 eV while µc-Si:H possesses a band gap of approximately 1.12 eV. Thus, when the crystalline fraction increases the band gap of the composed material decreases. Slight changes of the conditions during the initial silicon growth phase, *e.g.* a changed surface texture of the substrate which might ultimately introduces an altered temperature or potential distribution on the surface, may shift the process window for the optimal material. A higher surface roughness of textured ZnO:Al substrates was in fact reported to result in an increased crystallinity of silicon thin films [329, 330]. This is in accordance with the findings presented here.

The decrease in V_{oc} can be understood on the basis of equation (7.1). The increase of the quantum efficiency in the long wavelength range is also ascribed to the decreasing band gap of the absorber material because the band gap determines the long wavelength limit of band to band excitation of electrons from the valence band into the conduction band. Thus, the probability for absorption of long wavelength photons is increasing with decreasing band gap. This effect is presumably the reason for the observed improvement of the quantum efficiency (Fig. 7.5) in the near infrared spectral range. On the other hand the increased quantum efficiency in the short wavelength range may be due to the increased transmittance of the combined textured ZnO:Al front contact. To clarify the sole impact of the front contact surface texture, isolated from the influence of absorber material, further effort is necessary. The adjustment of the silicon deposition process, such that a constant crystallinity is obtained on each surface texture, would be desired. This is intended as a further study.

7.3. Tuning the Surface Texture Size

Another approach to use the unique locally limited effect of the electrochemical anodization is the reversed process sequence as applied in section 7.2, *i.e.* first an anodic polarization step and then a traditional chemical etching step. This allows to tune the surface structures with respect to their light scattering ability. In contrast to the combined texture introduced in section 7.2 the surface textures obtained here feature only one lateral size. To distinguish between the two processes the latter (anodic pretreatment and subsequent chemical etching) will be called *two-step single texture* hereafter.

The electrochemical pretreatment widens the grain boundaries and generates a significant number of new sites for the attack by acidic etching. By changing the etching time in HCl after anodization in K_2SO_4, the morphology gradually shifts from extremely small craters to sizes being closer to those after purely chemical etching as for the reference (Fig. 7.8). Since the etch pits are not only generated at some peculiar grain boundaries as in the purely chemical treatment [263], the density of craters is higher, their diameter is smaller, and the shapes are more regular than those of the reference.

As reported in chapter 6 the composition of the electrolyte has an effect on the features developing upon anodic dissolution. In particular, the anodization in K_2SO_4 containing solutions led to very selective dissolution of the grain boundaries while KCl containing solutions additionally led to partial dissolution of the grains. This is also reflected in the surface morphologies of the two-step single textured ZnO thin films. In contrast to anodization in K_2SO_4, the influence of the electrochemical

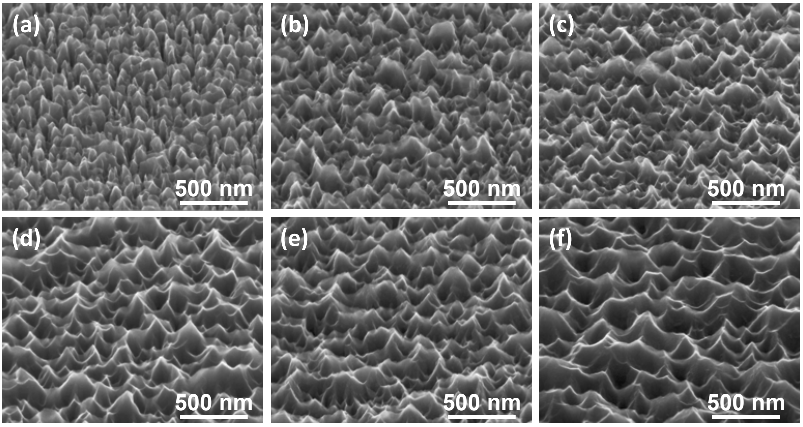

Fig. 7.8. SEM images of ZnO:Al thin films after biasing at +2.0 V vs. Ag|AgCl|3 M KCl for 600 s in 0.1 M K_2SO_4 and subsequent etching in 0.154 M HCl for (a) a short dip, (b) 5 s, (c) 10 s, (d) 20 s, (e) 30 s, (f) 40 s. Reproduced by permission of The Electrochemical Society from [291].

pretreatment in KCl as electrolyte on the surface morphology seems to be less pronounced, and the resulting structures are markedly different (Fig. 7.9). Initially, *e.g.*, after a short dip in HCl (Fig. 7.9a), the accentuation of the grain boundaries is still visible in terms of an increased density of craters. This however vanishes almost completely after prolonged etching (Fig. 7.9b - d), so that after 30 or 40 s of etching (Fig. 7.9e - f) the morphology is similar to that of a reference substrate. Furthermore, the increase in crater diameter is not as gradual as observed after anodization in K_2SO_4 (Fig. 7.8), although it is still visible.

The aforementioned effects of sulfate ions on the ZnO:Al thin film are considered as reasons for the observed difference. During the electrochemical anodization for 600 s the dissolution of the grain boundaries proceed deeper into the ZnO:Al thin films in K_2SO_4 as compared to KCl. This becomes especially evident after the etching step in HCl.

Although the surface structure obtained by the electrochemical pretreatment is clearly depending on the electrolyte, the electrical properties of the textured ZnO:Al thin films are not significantly different. Hall measurements of the resistivity ρ, charge carrier concentration n, mobility μ, and sheet resistance R_{sh} are plotted in Fig. 7.10 as a function of etching time of K_2SO_4-pretreated samples in 0.154 M HCl.

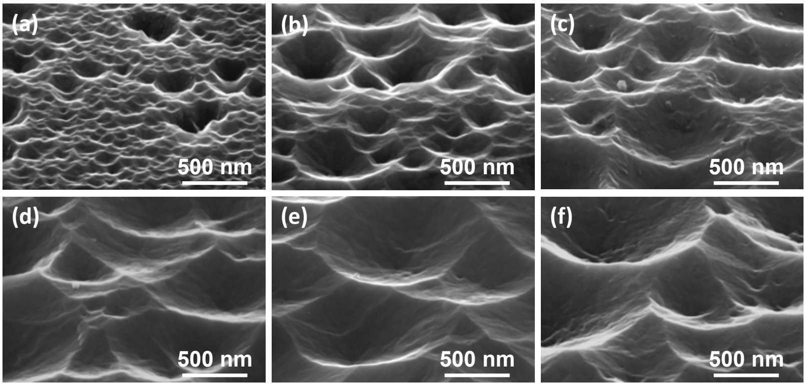

Fig. 7.9. SEM images of ZnO:Al thin films after biasing at +2.0 V vs. Ag|AgCl|3 M KCl for 600 s in 0.1 M KCl and subsequent etching in 0.154 M HCl for (a) a short dip, (b) 5 s, (c) 10 s, (d) 20 s, (e) 30 s, (f) 40 s. Reproduced by permission of The Electrochemical Society from [291].

The sheet resistance increases from $(3.3 \pm 0.2)\,\Omega$ in the as-deposited state (shown at 0 s) to $(13.0 \pm 0.6)\,\Omega$ after electrochemical pretreatment and 40 s of etching in diluted HCl. The latter value is also significantly higher than those of the reference ZnO:Al thin films ($(5.1 \pm 0.3)\ \Omega$, displayed as ×). A very similar trend is observed for the resistivity. The increase for the two-step single textured substrates compared to the reference substrate indicates that the chemical etching step is accelerated by the electrochemical pretreatment. This supports the assumption that new points of attack for the etchant are generated by the anodization step. This observation illustrates the necessity for carefully trading off the improved optical properties, originating from optimized surface morphologies, against a lowered conductivity, which is not desirable for an application of these films in solar cells.

The mobility and carrier concentration are not influenced significantly by the electrochemical treatment. The values remain almost constant within the measurement uncertainty. It is interesting to note that the carrier concentration in the reference thin film etched for 40 s in HCl without electrochemical pretreatment is approximately $2.5 \times 10^{20}\,\mathrm{cm}^{-3}$ higher than that after anodization and etching in HCl for 40 s. However, the measurement error in film thickness measurements has to be considered for the determination of the carrier concentration because the carrier concentration, as measured by the van der Pauw method (see section A.4.4), is

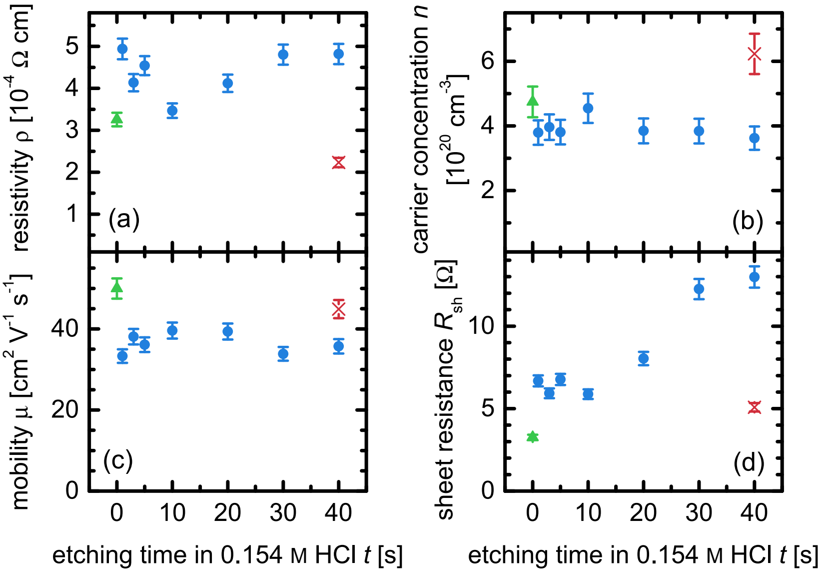

Fig. 7.10. Electrical properties of two-step single textured, RF-sputtered ZnO:Al thin films derived from Hall measurements. All films were firstly biased at +2 V for 600 s in 0.1 M K_2SO_4 and secondly etched in 0.154 M HCl for different etching times. The values at 0 s etching time (open triangles)show the properties of the untreated, as-deposited film. The reference (ZnO:Al etched in 0.154 M HCl for 40 s without electrochemical pretreatment) is shown in gray (open circles). Relative errors of ±10 % for the carrier concentration and ±5 % for the mobility, sheet resistance, and resistivity are estimated and shown as error bars. Adapted from [291].

inversely proportional to the film thickness. This error clearly dominates the total measurement error on rough films. The same is true for the resistivity which is directly proportional to the film thickness.

The combination of electrochemical treatment in different electrolytes and chemical etching opens up new ways to change the electrical and optical properties of ZnO thin films. This substantially extends the already high number of accessible structures that could be obtained by varying sputtering conditions together with purely chemical etching [3, 263]. By selectively tuning the crater size and (ir-)regularity, a material may thus be optimized for the needs of the Si absorber that is being deposited on top of it. This could, for example, allow a better adaption of the light scattering in different regions of the spectrum of light to single junction and tandem solar cells. Furthermore, the high aspect ratios of the grain boundaries will also affect the Si deposition process and the TCO/p-Si contact as already observed on the combined textured ZnO:Al front contacts in the last section.

To check the quality of the two-step single textured ZnO films in terms of their light scattering ability and electrical contact to the p-doped layer of the Si absorber, 1 cm × 1 cm µc-Si:H single junction thin film solar cells have been prepared using the two-step single textured ZnO:Al thin film as front contact. The solar cell design was again according to Fig. 7.1. To evaluate the influence of the electrochemical pretreatment and the crater diameter, solar cell deposition was carried out on all the films with KCl pretreatment shown in Fig. 5 and, in addition to that, on a reference substrate etched in 0.154 M HCl for 50 s only. The characteristic parameters of these solar cells, namely the initial efficiency η_{init}, fill factor FF, open circuit voltage V_{oc}, and short circuit current density j_{sc}, are shown in Fig. 7.11 as a function of the etching time in 0.154 M HCl. Please note that, other than in Fig. 7.10, the data set at 0 s etching time does not represent the as-deposited ZnO:Al thin film, but the film after anodization without any etching step in HCl. The results of the best solar cells for each time step are collected in Table 7.1.

The most obvious finding of this investigation is the fact that η_{init} as well as j_{sc} increase as a function of the etching time in HCl. As the craters grow in diameter and in depth, the light scattering ability of the ZnO:Al thin film is enhanced. This increases the probability of light absorption in the Si absorber and thus the current density due to a prolongation of the optical path length and an improved light trapping [29]. The highest current density values reached are in the range of (23.2 ± 0.1) mA cm^{-2} for the two-step single textured films. This corresponds well to j_{sc} of the reference film, however it does not exceed it. This is consistent with the observation that the morphology of the film (Fig. 7.9f) is very similar to that of the reference with crater diameters in the range of a few 100 nm.

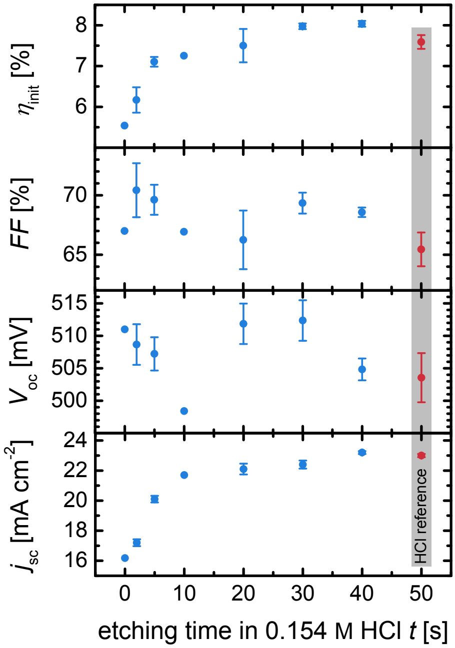

Fig. 7.11. Initial efficiency η_{init}, fill factor FF, open circuit voltage V_{oc}, and short circuit current density j_{sc} of µc-Si:H solar cells on two-step single textured, RF-sputtered ZnO:Al films. All films were first biased at +2 V vs. Ag|AgCl|3 M KCl for 300 s in 0.1 M KCl and subsequently etched in 0.154 M HCl for different etching times before Si deposition. The data set marked as HCl reference (shown in gray, open circles) is a solar cell with reference ZnO:Al etched in 0.154 M HCl for 50 s without electrochemical pretreatment. Adapted from [291].

The same trend can be observed as a function of the wavelength in DSR measurements (Fig. 7.12). As expected, non-optimized ZnO:Al thin film morphologies translate into lower EQE values than the reference front contact over the whole spectral range (Fig. 7.12a, solid line). Especially for the very short etching times in HCl (hence an almost smooth film surface), optical interferences at wavelengths λ of approximately 500 nm and above are observed due to Fabry-Pérot oscillations. These originate from reflection at the front and the back side of the ZnO:Al front contact (for $\lambda < 600$ nm or Si (for $\lambda > 600$ nm). In agreement with the j_{sc} data

Table 7.1. j-V characteristics of best solar cells ($1\,\mathrm{cm}^2$) on two-step single textured, RF-sputtered ZnO:Al films with anodic pretreatment for 300 s at +2.0 V vs. Ag|AgCl|3 M KCl in 0.1 M KCl.

Etch duration in 0.154 M HCl after pretreatment [s]	η_init [%]	FF [%]	V_oc [mV]	j_sc $\left[\mathrm{mA\ cm^{-2}}\right]$
0	5.54	67.0	511	16.18
2	6.49	72.6	512	17.48
5	7.19	70.9	509	19.92
10	7.25	66.9	498	21.74
20	7.93	69.3	514	22.23
30	8.08	70.5	517	22.16
40	8.13	68.9	506	23.30
50 (reference; no pretreatment)	7.83	67.6	505	22.93

(Fig. 7.11), the EQE values of the solar cells on the two-step single textured ZnO reach the level of the reference (Fig. 7.12a, cf. solid vs. dotted line), but do not exceed it. An improvement of the light trapping ability is thus not observed for the two-step single textured ZnO:Al thin films. The electrochemically introduced craters apparently possess slightly too low diameters for a more efficient overall light scattering. However, a closer look at the short wavelength range from 370 to 550 nm (Fig. 7.12b) implicates a gain for the film etched for 40 s in HCl after electrochemical pretreatment (dotted line) compared to the reference (solid line). Such an effect could be explained by craters with a diameter slightly below the ones of the reference and a stronger effect on the short wavelengths. Its significance however still needs to be verified.

The initial efficiency η_init shows the same tendency as j_sc. The maximum value of $(8.0 \pm 0.1)\,\%$ for the film etched for 40 s in 0.154 M HCl after electrochemical pretreatment (Fig. 7.11) is however approximately 0.4 % higher than the reference solar cell. This surprising effect cannot be explained by an improved light trapping, as this would have an effect on j_sc as well. It seems that the enhanced cell efficiency mainly originates from an improved FF and V_oc, despite the significant scatter of the data of these two parameters. Especially V_oc is up to 10 mV higher for the pretreated samples compared to the reference ZnO:Al thin film. This could be an indication for an improved electrical matching in terms of work function between the ZnO:Al front contact and the Si absorber. A different growth of Si due to the different morphology

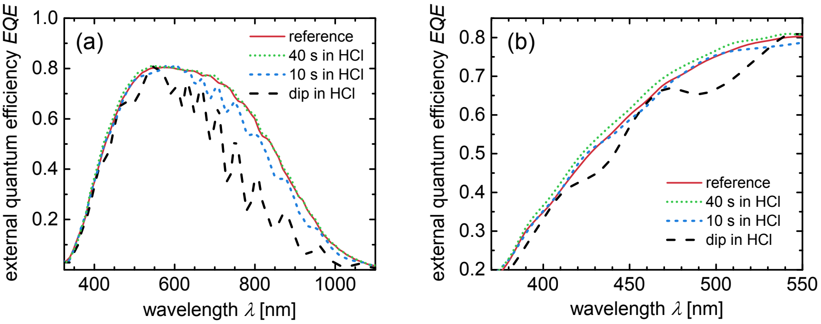

Fig. 7.12. (a) External quantum efficiencies of µc-Si:H solar cells on two-step single textured, RF-sputtered ZnO:Al films. All films were first biased at +2.0 V vs. Ag|AgCl|3 M KCl for 300 s in 0.1 M KCl and subsequently etched in 0.154 M HCl for a short dip (dashed line), 10 s (short dashed line), and 40 s (dotted), respectively, before Si deposition. The reference (solar cell with ZnO:Al etched in 0.154 M HCl for 50 s without electrochemical pretreatment) is plotted as a solid line. (b) Same EQE curves but only in the short wavelength range. Adapted from [291].

or surface chemistry might also contribute to this improvement since all solar cells have been prepared in one co-deposition step.

The best solar cell results for two-step single textured ZnO:Al films electrochemically pretreated in K_2SO_4 (as seen in Fig. 7.8) are summarized in Table 7.2. While the electrolyte has a major influence on the film morphology (Fig. 7.8 and Fig. 7.9), the single junction solar cell performance is quite similar. Overall, the observations of the results of the previously shown solar cells with KCl pretreatment are confirmed in the solar cell deposition on K_2SO_4-pretreated films: (i) j_{sc} is maximum for the solar cell on the reference ZnO:Al thin film without electrochemical pretreatment; (ii) η_{init} can be brought close to the reference by the anodization process with a maximum value of 8.35 % for a solar cell on a two-step single textured ZnO:Al thin film; (iii) V_{oc} is more than 10 mV higher for the solar cells on the two-step single textured ZnO:Al thin films; (iv) no clear trend is observed for the FF.

Table 7.2. *j-V* characteristics of best solar cells (1 cm^2) on two-step single textured, RF-sputtered ZnO:Al films with anodic pretreatment for 300 s at +2.0 V vs. Ag|AgCl|3 M KCl in 0.1 M K_2SO_4.

Etch duration in 0.154 M HCl after pretreatment [s]	η_{init} [%]	FF [%]	V_{oc} [mV]	j_{sc} [mA cm^{-2}]
10	7.23	68.9	540	19.45
30	8.35	73.0	543	21.09
50 (reference; no pretreatment)	8.41	73.2	526	22.90

7.4. Conclusion

Two novel approaches were presented to change the surface morphology of RF-sputtered ZnO:Al thin films by means of combining anodic electrochemical treatment with conventional etching in diluted HCl. The interfacial reaction of the anodic treatment is distinctly limited to the grain boundaries of the thin film, leading to unique surface structures that cannot be achieved by any other solution-based technique. The combination of this electrochemical approach with chemical etching in diluted HCl allows to either prepare a combined texture exhibiting a fine structure superposed on the crater-shaped surface texture obtained by chemical etching or to tune the feature size of the surface morphology of ZnO:Al thin films such.

The application of such films in µc-Si:H single junction solar cells has proven their usability for Si thin-film photovoltaic applications. It was observed that the tuning of the ZnO film surface morphology can contribute to an improved light trapping in the solar cell. However, optimum structures still strongly depend on the experimental parameters of the surface treatment (electrochemical as well as chemical) and on the physical properties of the ZnO film. Furthermore, the combined texture was found to influence the growth of the µc-Si:H such that the crystalline volume fraction, as measured by Raman spectroscopy, increased with longer anodic treatment. An improvement of the light incouling ability was suspected, however, an adapted Si deposition process, leading to a comparable Si crystallinity for all textures, is necessary to clarify the optical influence of the surface texture on the solar cell performance. This is, however, a considerable effort dealing with the challenge to optimize PECVD processes for each individual, gradually changed surface texture. Still, it is the only way to prove the real potential of the combined texture for optimization of the light management in Si thin-film solar cells. Thus, it is a topic of ongoing work.

The results reported in this chapter are an initial step towards an optimization of the etching procedure. The potential of the electrochemical treatment for an improvement of sputter-deposited ZnO front contact layers has been demonstrated. However, further work has to be done to understand and systemize the influence of the electrochemical treatment of the ZnO:Al front contact on the resulting solar cells performance. Especially for films with excellent electrical and optical properties derived from slightly different deposition conditions, which cannot be etched easily in the established processes [3], the electrochemical treatment might be key to the application as front contacts in Si thin-film solar cells. This might ultimately lead to an increased overall solar cell performance.

8. Conclusion and Future Prospects

The aim of this work has been to further the understanding of the stability of polycrystalline zinc oxide thin films in aqueous solutions with the intention to open new ways to create light scattering surface textures for the application in thin-film solar cells.

Development in this field is required because thin-film solar cells depend crucially on the ability to introduce suitable surface morphologies for light scattering. Conventional chemical texturing of zinc oxide thin films, however, shows a strong dependence on the deposition process. Thus, electrochemical methods were chosen in this work to investigate both deposition and dissolution of zinc oxide thin films. This approach adds the electrode potential as a new parameter to the texturing process, enabling a broader range of accessible surface textures. Furthermore, this allows for the *in-situ* monitoring of the process. Additionally, the same experimental setup can be used to deposit zinc oxide from aqueous solutions.

The interplay between electrochemical deposition and dissolution are largely determined by the local pH at the electrode. The application of a bias potential to zinc oxide electrodes in a suitable electrolyte allows for the specific manipulation of the interfacial pH. Thereby, the precipitation-dissolution equilibrium can be shifted in either direction. Cathodic potentials can be used to reduce suitable precursors, such as molecular oxygen or nitrate in a Zn^{2+} containing solution, to form hydroxide ions locally at the electrode surface. Consequently the interfacial pH value increases. Ultimately, this results in the precipitation of zinc oxide. In contrast, the anodic potential range allows for the dissolution of zinc oxide either by direct anodic decomposition of the crystal lattice or again by intentional manipulation of the interfacial pH. However, in this case the oxygen evolution reaction is used to provide protons which shifts the pH locally into the acidic range where zinc oxide is no longer stable and thus dissolves.

The cathodic deposition of zinc oxide is a dynamically developing research field since the pioneering works by Peulon and Lincot [156] and Izaki and Omi [42]. The utilization of this approach at the IEK-5 (Forschungszentrum Jülich) started with this thesis. Hence, the results presented in chapter 4 are first trials to deposit zinc oxide using a solution based technique. The dependence of the zinc oxide precipitation and crystallization on several parameters such as the deposition potential, the bath temperature, the substrate, and the composition of the electrolyte were investigated. The temperature was found to play an important role for the crystallization. A minimum temperature of 50 °C was found to be necessary to deposit crystalline zinc oxide structures. Higher temperatures generally lead to a more pronounced formation of well defined hexagonal crystals. The reduction of nitrate turned out to be catalyzed by the Zn^{2+} ions present. Thus, when using nitrate solutions for electrodeposition of zinc oxide the Zn^{2+} concentration must be carefully adjusted. For Zn^{2+} concentrations above 25 mM the probability for the precipitation of flake-like zinc compounds increases. The comparison of electrochemical depositions on ITO and zinc oxide thin films under otherwise identical conditions revealed the fundamental influence of the substrate. While the growth on ITO led to hexagonally shaped crystals with random orientation of the c-axis, the growth on zinc oxide thin films appears to proceed epitaxially, conserving the grain size and preferential c-axis orientation parallel to the surface normal. The optical characterization of a closed electrochemically deposited zinc oxide thin film revealed a Burstein-Moss shift suggesting degenerate doping due to intrinsic defects, hydrogen, or chloride incorporated in the film.

As mentioned above, chemical texturing is a common tool to achieve rough surface morphologies. Studies on the chemical dissolution of polycrystalline zinc oxide thin films in several acidic and alkaline solutions are plentiful. However, the determination of the dissolution rate was, so far, only accessible after the actual etching process. Furthermore, the measured dissolution rates contain a considerable measurement error since the measurement relies on thickness measurements on rough surfaces. In chapter 5 an elegant electrochemical method is used to measure the dissolution rate instantaneously during chemical etching. The dissolution rate was monitored in several buffered and unbuffered acidic solutions and a high degree of accordance to values found in literature was observed. Thus, an easy to implement approach for an active control of the etching process is enabled, allowing to stop the etching when a desired film thickness is removed.

The electrochemical dissolution of zinc oxide, which is investigated in chapter 6, goes one step beyond. Here, electrochemical methods are used not only to observe, but to actively control the dissolution of polycrystalline zinc oxide thin films. In contrast to moderately doped zinc oxide crystals anodic dissolution was found to be possible for degenerately doped zinc oxide thin films at potentials exceeding an anodic onset potential of approximately 1.3 V. The anodic dissolution process selectively dissolved the material in the close vicinity of the grain boundaries. This led to a novel surface texture which is not accessible by any other method. The opto-electronic properties of anodically treated zinc oxide thin films were comprehensively studied. A shift of the optical band gap and a decrease in the near infrared absorptance were ascribed to a decrease of the charge carrier concentration due to the formation of surface states. The effect of several electrolytes was examined. This allowed to vary the degree of selectivity of the dissolution process to the grain boundaries. Sulfate solutions showed the highest selectivity, probably due to a buffering effect on the interfacial pH. Enhanced dissolution under illumination showed that the dissolution kinetics was limited by the presence of holes at the zinc oxide/electrolyte interface. The determination of the flat band potential enabled access to the band alignment at this interface and revealed band to band tunneling as the dominant charge transfer process. The field enhancement at the grain boundaries was suspected to be the reason for the preferred dissolution of the grain boundaries.

The lateral dimensions of surface morphologies obtained by anodic dissolution are below the wavelength of light in the visible wavelength range. Thus, they do not provide efficient light scattering, even though a beneficial effect on the transmittance was observed. To provide both increased transmittance and light scattering, the novel anodic texture was combined with conventional chemical texturing. This two-step approach allows to either obtain a superposition of two textures or to adjust the surface feature size depending on the sequence. The application of such thin films as front contacts in microcystalline silicon solar cells has proven their usability for silicon thin-film photovoltaic applications.

In conclusion, this work examines the stability of the interface between the large band gap, n-type semiconductor zinc oxide and an aqueous electrolyte. Both the cathodic and the anodic branch were studied giving rise to either electrochemical deposition or dissolution of zinc oxide. Several results such as the charge transfer mechanism are transferable to other semiconductor/electrolyte interfaces.

The applications for solar cell improvements from the knowledge gained within this work are far from exhausted. For instance a proper texturing of ZnO:Al thin films, sputter-deposited at high temperature and low pressure ($T \gtrsim 200°\mathrm{C}$, $p \gtrsim 1 \times 10^{-6}\mathrm{bar}$) or low temperature and high pressure ($T \lesssim 100\,°\mathrm{C}$, $p \gtrsim 30 \times 10^{-6}\,\mathrm{bar}$), is to date not available on a purely chemical route due to either too few or too many etching sites [2]. Also the target doping concentration strongly determines the feasibility to achieve a suitable surface texture [3]. Electrochemical texturing might be able to overcome these limitations.

Furthermore, the fact that electrochemical deposition and dissolution are limited by charge transfer reactions could be utilized to locally grow or dissolve zinc oxide. It was shown by Könenkamp *et al.* that electrochemical deposition of zinc oxide on n-type and p-type silicon wafers is feasible [224, 331]. However, for low electron concentrations occurring in weakly n-type and in p-type silicon, growth is inhibited. Hence, selective growth in certain areas of higher doping concentration can be achieved. Furthermore, illumination of the substrate leads to an increased electron concentration and consequently facilitates electrochemical deposition. This again allows for local zinc oxide deposition [331].

In contrast, electrochemical dissolution of zinc oxide depends on the abundance of holes at the surface, as was shown in chapter 6. Thus, local illumination of a zinc oxide thin film, *e.g.* with a UV laser, would allow for local dissolution of zinc oxide. Similarly, local structuring of zinc oxide can be achieved by scanning probe methods as was recently demonstrated by Tang *et al.* [332]. They used a scanning electrochemical microscope featuring a microelectrode to pattern zinc oxide thin films on a microscopic scale.

Also, the combination of electrochemical deposition and subsequent etching can reveal new ways to achieve specialized materials such as hexagonal nanowires [161,163]. Furthermore, electrochemical methods provide new possibilities for the preparation of highly porous electrodes that allow for large active surface areas. They can be produced by electrochemical etching, as shown in chapter 6, or by the incorporation of organic additives during electrochemical deposition [296] and are well suited for the application in organic solar cells.

In principle, upscaling of electrochemical processes is feasible which was demonstrated by *Canon* (Japan) who used a roll-to-roll process for the cathodic electrodeposition of zinc oxide [235]. However, further work is needed to verify the applicability of the electrochemical texturing investigated in this work on a large scale.

Due to low cost of solution based deposition processes the preparation of solar cells using solely electrochemical processes would be highly desirable. Although, in principle, previous work has shown that it is possible to produce copper indium diselenide solar cells on an entirely electrochemical basis [234], their performance is, so far, not competitive to solar cells deposited using vacuum processes.

These few examples show that the employment of electrochemical methods for the preparation of new zinc oxide structures entails numerous possibilities beyond the light management in thin-film solar cells. However, a fundamental understanding of the semiconductor/electrolyte interface and its stability is crucial for all these applications.

Bibliography

[1] J. Müller, B. Rech, J. Springer, and M. Vanecek, *TCO and light trapping in silicon thin film solar cells*, Sol. Energy **77** (2004), 917–930.

[2] O. Kluth, G. Schöpe, J. Hüpkes, C. Agashe, J. Müller, and B. Rech, *Modified Thornton model for magnetron sputtered zinc oxide: film structure and etching behaviour*, Thin Solid Films **442** (2003), 80–85.

[3] M. Berginski, J. Hüpkes, M. Schulte, G. Schöpe, H. Stiebig, B. Rech, and M. Wuttig, *The effect of front ZnO:Al surface texture and optical transparency on efficient light trapping in silicon thin-film solar cells*, J. Appl. Phys. **101** (2007), 074903.

[4] J. I. Owen, J. Hüpkes, H. Zhu, E. Bunte, and S. E. Pust, *Novel etch process to tune crater size on magnetron sputtered ZnO:Al*, Phys. Status Solidi A **208** (2011), 109–113.

[5] H. Gerischer and W. Mindt, *The mechanisms of the decomposition of semiconductors by electrochemical oxidation and reduction*, Electrochim. Acta **13** (1968), 1329–1341.

[6] F. Lohmann, *Elektrochemische Reaktionen an UV-bestrahlten Zinkoxidelektroden*, Ber. Bunsen. phys. Chem. **70** (1966), 87–92.

[7] X. Wang, L. Zhi, and K. Mullen, *Transparent, Conductive Graphene Electrodes for Dye-Sensitized Solar Cells*, Nano Lett. **8** (2008), 323–327.

[8] G. Eda, G. Fanchini, and M. Chhowalla, *Large-area ultrathin films of reduced graphene oxide as a transparent and flexible electronic material*, Nat. Nanotechnol. **3** (2008), 270–274.

[9] Z. Wu, Z. Chen, X. Du, J. M. Logan, J. Sippel, M. Nikolou, K. Kamaras, J. R. Reynolds, D. B. Tanner, A. F. Hebard, and A. G. Rinzler, *Transparent, Conductive Carbon Nanotube Films*, Science **305** (2004), 1273–1276.

[10] L. Groenendaal, F. Jonas, D. Freitag, H. Pielartzik, and J. R. Reynolds, *Poly(3,4-ethylenedioxythiophene) and Its Derivatives: Past, Present, and Future*, Adv. Mater. **12** (2000), 481–494.

[11] S. Kirchmeyer and K. Reuter, *Scientific importance, properties and growing applications of poly(3,4-ethylenedioxythiophene)*, J. Mater. Chem. **15** (2005), 2077–2088.

[12] L. Hu, H. S. Kim, J.-Y. Lee, P. Peumans, and Y. Cui, *Scalable Coating and Properties of Transparent, Flexible, Silver Nanowire Electrodes*, ACS Nano **4** (2010), 2955–2963.

[13] S. De, T. M. Higgins, P. E. Lyons, E. M. Doherty, P. N. Nirmalraj, W. J. Blau, J. J. Boland, and J. N. Coleman, *Silver Nanowire Networks as Flexible, Transparent, Conducting Films: Extremely High DC to Optical Conductivity Ratios*, ACS Nano **3** (2009), 1767–1774.

[14] A. J. Freeman, K. R. Poeppelmeier, T. O. Mason, R. P. H. Chang, and T. J. Marks, *Chemical and Thin-Film Strategies for New Transparent Conducting Oxides*, MRS Bulletin **25** (2000), 45–51.

[15] R. Gordon, *Criteria for choosing transparent conductors*, MRS Bulletin **25** (2000), 52–57.

[16] T. Minami, *Transparent conducting oxide semiconductors for transparent electrodes*, Semicond. Sci. Tech. **20** (2005), S35.

[17] E. Fortunato, D. Ginley, H. Hosono, and D. C. Paine, *Transparent Conducting Oxides for Photovoltaics*, MRS Bulletin **32** (2007), 242–247.

[18] A. Feltrin and A. Freundlich, *Material considerations for terawatt level deployment of photovoltaics*, Renew. Energ. **33** (2008), 180 – 185.

[19] K. Sato, Y. Gotoh, Y. Wakayama, Y. Hayashi, K. Adachi, and H. Nishimura, *Highly Textured* SnO_2*:F TCO Films for a-Si Solar Cells*, Rep. Res. Lab. Asahi Glass Co., Ltd. **42** (1992), 129–137.

[20] W. Beyer, J. Hüpkes, and H. Stiebig, *Transparent conducting oxide films for thin film silicon photovoltaics*, Thin Solid Films **516** (2007), 147–154.

[21] K. Ding, T. Kirchartz, B. E. Pieters, C. Ulbrich, A. M. Ermes, S. Schicho, A. Lambertz, R. Carius, and U. Rau, *Characterization and simulation of a-Si:H/*μ*c-Si:H tandem solar cells*, Sol. Energy Mater. Sol. Cells **95** (2011), 3318–3327.

[22] J. Müller, O. Kluth, S. Wieder, H. Siekmann, G. Schöpe, W. Reetz, O. Vetterl, D. Lundszien, A. Lambertz, F. Finger, B. Rech, and H. Wagner, *Development of highly efficient thin film silicon solar cells on texture-etched zinc oxide-coated glass substrates*, Sol. Energy Mater. Sol. Cells **66** (2001), 275 – 281.

[23] S. Faÿ, J. Steinhauser, S. Nicolay, and C. Ballif, *Polycrystalline ZnO:B grown by LPCVD as TCO for thin film silicon solar cells*, Thin Solid Films **518** (2010), 2961 – 2966.

[24] S. Major, S. Kumar, M. Bhatnagar, and K. L. Chopra, *Effect of hydrogen plasma treatment on transparent conducting oxides*, Appl. Phys. Lett. **49** (1986), 394–396.

[25] T. Minami, H. Sato, H. Nanto, and S. Takata, *Heat treatment in hydrogen gas and plasma for transparent conducting oxide films such as ZnO, SnO_2 and indium tin oxide*, Thin Solid Films **176** (1989), 277 – 282.

[26] L. M. Levinson and H. R. Philipp, *Zinc-oxide Varistors - A Review*, Am. Cheram. Soc. Bull. **65** (1986), 639–646.

[27] P. Mitra, A. Chatterjee, and H. Maiti, *ZnO thin film sensor*, Mater. Lett. **35** (1998), 33–38.

[28] D.-K. Hwang, M.-S. Oh, J.-H. Lim, and S.-J. Park, *ZnO thin films and light-emitting diodes*, J. Phys. D: Appl. Phys. **40** (2007), R387.

[29] J. Hüpkes, J. Müller, and B. Rech, *Texture Etched ZnO:Al for Silicon Thin Film Solar Cells*, Transparent Conductive Zinc Oxide: Basics and Applications in Thin Film Solar Cells (K. Ellmer, A. Klein, and B. Rech, eds.), Springer, Berlin, 2008, pp. 359–414.

[30] S. Nicolay, M. Despeisse, F.-J. Haug, and C. Ballif, *Control of LPCVD ZnO growth modes for improved light trapping in thin film silicon solar cells*, Sol. Energy Mater. Sol. Cells **95** (2011), 1031–1034.

[31] H. Kim, J. Horwitz, S. Qadri, and D. Chrisey, *Epitaxial growth of Al-doped ZnO thin films grown by pulsed laser deposition*, Thin Solid Films **420-421** (2002), 107–111.

[32] A. Suzuki, T. Matsushita, Y. Sakamoto, N. Wada, T. Fukuda, H. Fujiwara, and M. Okuda, *Surface Flatness of Transparent Conducting ZnO:Ga Thin Films Grown by Pulsed Laser Deposition*, Jpn. J. Appl. Phys. **35** (1996), 5457–5461.

[33] E. M. Kaidashev, M. Lorenz, H. von Wenckstern, A. Rahm, H.-C. Semmelhack, K.-H. Han, G. Benndorf, C. Bundesmann, H. Hochmuth, and M. Grundmann, *High electron mobility of epitaxial ZnO thin films on c-plane sapphire grown by multistep pulsed-laser deposition*, Appl. Phys. Lett. **82** (2003), 3901–3903.

[34] J. Hu and R. G. Gordon, *Textured fluorine-doped ZnO films by atmospheric pressure chemical vapor deposition and their use in amorphous silicon solar cells*, Sol. Cells **30** (1991), 437–450.

[35] K. Saito, Y. Watanabe, K. Takahashi, T. Matsuzawa, B. Sang, and M. Konagai, *Photo atomic layer deposition of transparent conductive ZnO films*, Sol. Energy Mater. Sol. Cells **49** (1997), 187–193.

[36] K. Ellmer, *Magnetron sputtering of transparent conductive zinc oxide: relation between the sputtering parameters and the electronic properties*, J. Phys. D: Appl. Phys. **33** (2000), R17–R32.

[37] J. B. Webb, D. F. Williams, and M. Buchanan, *Transparent and highly conductive films of ZnO prepared by rf reactive magnetron sputtering*, Appl. Phys. Lett. **39** (1981), 640–642.

[38] G. Harding, B. Window, and E. Horrigan, *Aluminium- and indium-doped zinc oxide thin films prepared by DC magnetron reactive sputtering*, Sol. Energy Mater. **22** (1991), 69–91.

[39] W. Tang and D. Cameron, *Aluminum-doped zinc oxide transparent conductors deposited by the sol-gel process*, Thin Solid Films **238** (1994), 83–87.

[40] T. Okamura, Y. Seki, S. Nagakari, and H. Okushi, *Junction Properties and Gap States of Zno Thin-film Prepared By Sol-gel Process*, Jpn. J. Appl. Phys., Part 1 **31** (1992), 3218–3220.

[41] T. Nagase, T. Ooie, and J. Sakakibara, *A novel approach to prepare zinc oxide films: excimer laser irradiation of sol-gel derived precursor films*, Thin Solid Films **357** (1999), 151–158.

[42] M. Izaki and T. Omi, *Transparent zinc oxide films prepared by electrochemical reaction*, Appl. Phys. Lett. **68** (1996), 2439–2440.

[43] S. Peulon and D. Lincot, *Mechanistic Study of Cathodic Electrodeposition of Zinc Oxide and Zinc Hydroxychloride Films from Oxygenated Aqueous Zinc Chloride Solutions*, J. Electrochem. Soc. **145** (1998), 864–874.

[44] S. Major, A. Banerjee, and K. Chopra, *Highly transparent and conducting indium-doped zinc oxide films by spray pyrolysis*, Thin Solid Films **108** (1983), 333–340.

[45] D. R. Acosta, O. Lovera, A. Maldonaldo, R. Asomoza, H. Gomez, A. Palafox, M. D. L. L. Olvera, and J. Palaciosgomez, *ZnO:In thin films prepared with different precursor salts by spray pyrolysis and studied by electron microscopy*, Mater. Res. Soc. Symp. Proc. **355** (1995), 587–592.

[46] K. Ellmer, A. Klein, and B. Rech (eds.), *Transparent Conductive Zinc Oxide - Basics and Applications in Thin Film Solar Cells*, Springer, Berlin, 2008.

[47] C. Jagadish and S. J. Pearton (eds.), *Zink Oxide Bulk, Thin Films and Nanostructures: Processing, Properties ans Applications*, Elsevier, Oxford, Amsterdam, 2006.

[48] N. H. Nickel and E. Terukov (eds.), *Zinc Oxide – A Material for Micro- and Optoelectronic Applications*, Nato Science Series, Vol. 194, Springer, 2005.

[49] C. F. Klingshirn, *Zinc Oxide: from fundamental properties towards novel applications*, Springer series in materials science, Vol. 120, Springer, Heidelberg, 2010.

[50] H. Morkoç and U. Özgür, *Zinc Oxide: Fundamentals, Materials, and Device Technology*, Wiley, Weinheim, 2009.

[51] C. Bundesmann, R. Schmidt-Grund, and M. Schubert, *Optical Properties of ZnO and Related Compounds*, Transparent Conductive Zinc Oxide: Basics and Applications in Thin Film Solar Cells (K. Ellmer, A. Klein, and B. Rech, eds.), Springer, Berlin, 2008, pp. 79–124.

[52] S. Desgreniers, *High-density phases of ZnO: Structural and compressive parameters*, Phys. Rev. B **58** (1998), 14102–14105.

[53] F. Decremps, J. Pellicer-Porres, A. M. Saitta, J.-C. Chervin, and A. Polian, *High-pressure Raman spectroscopy study of wurtzite ZnO*, Phys. Rev. B **65** (2002), 092101.

[54] E. H. Kisi and M. M. Elcombe, *u Parameters for the Wurtzite Structure of ZnS and ZnO using Powder Neutron Diffraction*, Acta Crystallogr. C **45** (1989), 1867–1870.

[55] F. A. Cotton, *Chemical Applications of Group Theory*, John Wiley & Sons, New York, 1990.

[56] O. Dulub, L. A. Boatner, and U. Diebold, *STM study of the geometric and electronic structure of ZnO(0001)-Zn, ($000\bar{1}$)-O, ($10\bar{1}0$), and ($11\bar{2}0$) surfaces*, Surf. Sci. **519** (2002), 201 – 217.

[57] W. M. Haynes, *CRC Handbook of Chemistry and Physics*, 93^{rd} ed., Taylor and Francis, Boca Raton, USA, 2012.

[58] J. I. Owen, *Growth, Etching, and Stability of Sputtered ZnO:Al for Thin-Film Silicon Solar Cells*, Ph.D. thesis, RWTH Aachen, 2011.

[59] S. Pearton, D. Norton, K. Ip, Y. Heo, and T. Steiner, *Recent progress in processing and properties of ZnO*, Prog. Mater. Sci. **50** (2005), 293 – 340.

[60] N. F. Mott, *Metal-Insulator Transitions*, Contemp. Phys. **14** (1973), 401–413.

[61] F. A. Kröger, *The Chemistry of Imperfect Crystals*, North Holland Pub. Co., Amsterdam, 1964.

[62] Y.-M. Chiang, D. P. Birnie, and W. D. Kingery, *Physical Ceramics*, Wiley, New York, 1997.

[63] D. M. Smyth, *The Defect Chemistry of Metal Oxides*, Oxford University Press, New York, 2000.

[64] S. B. Zhang, S.-H. Wei, and A. Zunger, *Intrinsic n-type versus p-type doping asymmetry and the defect physics of ZnO*, Phys. Rev. B **63** (2001), 075205.

[65] Y. S. Avadhut, J. Weber, E. Hammarberg, C. Feldmann, and J. Schmedt auf der Gunne, *Structural investigation of aluminium doped ZnO nanoparticles by solid-state NMR spectroscopy*, Phys. Chem. Chem. Phys. **14** (2012), 11610–11625.

[66] C. R. A. Catlow, A. A. Sokol, and A. Walsh, *Microscopic origins of electron and hole stability in ZnO*, Chem. Commun. **47** (2011), 3386–3388.

[67] R. van de Krol and M. Grätzel (eds.), *Photoelectrochemical hydrogen production*, Electronic Materials: Science & Technology, Vol. 102, Springer, 2012.

[68] T. Minami, H. Nanto, and S. Takata, *Highly Conductive and Transparent Aluminum Doped Zinc Oxide Thin Films Prepared by RF Magnetron Sputtering*, Jpn. J. Appl. Phys. **23** (1984), L280–L282.

[69] T. Minami, H. Sato, H. Nanto, and S. Takata, *Group III Impurity Doped Zinc Oxide Thin Films Prepared by RF Magnetron Sputtering*, Jpn. J. Appl. Phys. **24** (1985), L781–L784.

[70] V. Bhosle, A. Tiwari, and J. Narayan, *Electrical properties of transparent and conducting Ga doped ZnO*, J. Appl. Phys. **100** (2006), 033713.

[71] P. J. Cannard and R. J. D. Tilley, *New Intergrowth Phases in the ZnO-ln_2O_3 System*, J. Solid State Chem. **73** (1988), 418–426.

[72] H. Y. Xu, Y. C. Liu, R. Mu, C. L. Shao, Y. M. Lu, D. Z. Shen, and X. W. Fan, *F-doping effects on electrical and optical properties of ZnO nanocrystalline films*, Appl. Phys. Lett. **86** (2005), 123107.

[73] B. Choi, I. Kim, D. Kim, K. Lee, T. Lee, B. Cheong, Y.-J. Baik, and W. Kim, *Electrical, optical and structural properties of transparent and conducting ZnO thin films doped with Al and F by rf magnetron sputter*, J. Eur. Ceram. Soc. **25** (2005), 2161 – 2165.

[74] E. Chikoidze, M. Nolan, M. Modreanu, V. Sallet, and P. Galtier, *Effect of chlorine doping on electrical and optical properties of ZnO thin films*, Thin Solid Films **516** (2008), 8146 – 8149.

[75] B. K. Meyer, J. Sann, D. M. Hofmann, C. Neumann, and A. Zeuner, *Shallow donors and acceptors in ZnO*, Semicond. Sci. Tech. **20** (2005), S62.

[76] O. Kluth, G. Schöpe, B. Rech, R. Menner, M. Oertel, K. Orgassa, and H. W. Schock, *Comparative material study on RF and DC magnetron sputtered ZnO:Al films*, Thin Solid Films **502** (2006), 311 – 316.

[77] H. J. Ko, Y. F. Chen, S. K. Hong, H. Wenisch, T. Yao, and D. C. Look, *Ga-doped ZnO films grown on GaN templates by plasma-assisted molecular-beam epitaxy*, Appl. Phys. Lett. **77** (2000), 3761–3763.

[78] S. B. Zhang, S.-H. Wei, and A. Zunger, *A phenomenological model for systematization and prediction of doping limits in II–VI and I–III–VI_2 compounds*, J. Appl. Phys. **83** (1998), 3192–3196.

[79] K. Ellmer, *Past achievements and future challenges in the development of optically transparent electrodes*, Nat. Photonics **6** (2012), 809–817.

[80] C. G. Van de Walle, *Hydrogen as a Cause of Doping in Zinc Oxide*, Phys. Rev. Lett. **85** (2000), 1012–1015.

[81] D. M. Hofmann, A. Hofstaetter, F. Leiter, H. Zhou, F. Henecker, B. K. Meyer, S. B. Orlinskii, J. Schmidt, and P. G. Baranov, *Hydrogen: A Relevant Shallow Donor in Zinc Oxide*, Phys. Rev. Lett. **88** (2002), 045504.

[82] S. H. Lee, T. S. Lee, K. S. Lee, B. Cheong, Y. D. Kim, and W. M. Kim, *Characteristics of hydrogen co-doped ZnO:Al thin films*, J. Phys. D: Appl. Phys. **41** (2008), 095303.

[83] D. Look, D. Reynolds, J. Sizelove, R. Jones, C. Litton, G. Cantwell, and W. Harsch, *Electrical properties of bulk ZnO*, Solid State Commun. **105** (1998), 399 – 401.

[84] C. Agashe, O. Kluth, J. Hüpkes, U. Zastrow, B. Rech, and M. Wuttig, *Efforts to improve carrier mobility in radio frequency sputtered aluminum doped zinc oxide films*, J. Appl. Phys. **95** (2004), 1911–1917.

[85] P. Drude, *On the electron theory of metals*, Ann. Phys. **1** (1900), 566–613.

[86] J. M. Luttinger and W. Kohn, *Motion of Electrons and Holes in Perturbed Periodic Fields*, Phys. Rev. **97** (1955), 869–883.

[87] G. Masetti, M. Severi, and S. Solmi, *Modeling of carrier mobility against carrier concentration in arsenic-, phosphorus-, and boron-doped silicon*, IEEE Trans. Electron Devices **30** (1983), 764–769.

[88] T. Pisarkiewicz, K. Zakrzewska, and E. Leja, *Scattering of charge carriers in transparent and conducting thin oxide films with a non-parabolic conduction band*, Thin Solid Films **174, Part 1** (1989), 217 – 223.

[89] K. Ellmer and R. Mientus, *Carrier transport in polycrystalline transparent conductive oxides: A comparative study of zinc oxide and indium oxide*, Thin Solid Films **516** (2008), 4620 – 4627.

[90] J. Y. W. Seto, *Electrical Properties of Polycrystalline Silicon Films*, J. Appl. Phys. **46** (1975), 5247–5254.

[91] G. Baccarani, B. Riccò, and G. Spadini, *Transport properties of polycrystalline silicon films*, J. Appl. Phys. **49** (1978), 5565–5570.

[92] K. Ellmer, *Resistivity of polycrystalline zinc oxide films: current status and physical limit*, J. Phys. D: Appl. Phys. **34** (2001), 3097.

[93] K. Ellmer and R. Mientus, *Carrier transport in polycrystalline ITO and ZnO:Al II: The influence of grain barriers and boundaries*, Thin Solid Films **516** (2008), 5829–5835.

[94] K. Ellmer and A. Klein, *ZnO and Its Applications*, Transparent Conductive Zinc Oxide (K. Ellmer, A. Klein, and B. Rech, eds.), Springer Series in Materials Science, Vol. 104, Springer, Berlin, Heidelberg, 2008, pp. 1–33.

[95] S. S. Devlin, Physics and Chemistry of II-VI Compounds (M. Aven and J. S. Prener, eds.), North Holland Pub. Co., Amsterdam, 1967, p. 549.

[96] J. Bardeen and W. Shockley, *Deformation Potentials and Mobilities in Non-Polar Crystals*, Phys. Rev. **80** (1950), 72–80.

[97] D. L. Rode, Semiconductors and Semimetals (R. K. Willardson and A. Beer, eds.), Academic Press, New York, 1975, p. 1.

[98] J. D. Zook, *Piezoelectric Scattering in Semiconductors*, Phys. Rev. **136** (1964), A869–A878.

[99] P. Wagner and R. Helbig, *Halleffekt und anisotropie der beweglichkeit der elektronen in ZnO*, J. Phys.Chem. Solids **35** (1974), 327 – 335.

[100] C. Erginsoy, *Neutral Impurity Scattering in Semiconductors*, Phys. Rev. **79** (1950), 1013–1014.

[101] H. L. Hartnagel, A. L. Dawar, A. K. Jain, and C. Jagadish, *Semiconducting Transparent Thin Films*, Institute of Physics Publishing, 1995.

[102] C. Kittel, *Introduction to solid state physics*, 8th ed. ed., Wiley, New York, 2005.

[103] F. Ruske, M. Roczen, K. Lee, S. Gall, J. Hüpkes, D. Hrunski, and B. Rech, *Improved electrical transport in Al-doped zinc oxide by thermal treatment*, J. Appl. Phys. **107** (2010), 013708.

[104] B. E. Sernelius, K.-F. Berggren, Z.-C. Jin, I. Hamberg, and C. G. Granqvist, *Band-gap tailoring of ZnO by means of heavy Al doping*, Phys. Rev. B **37** (1988), 10244–10248.

[105] E. Burstein, *Anomalous Optical Absorption Limit in InSb*, Phys. Rev. **93** (1954), 632–633.

[106] T. S. Moss, *The Interpretation of the Properties of Indium Antimonide*, Proc. Phys. Soc. B **67** (1954), 775.

[107] I. Hamberg, C. G. Granqvist, K. F. Berggren, B. E. Sernelius, and L. Engström, *Band-gap widening in heavily Sn-doped* In_2O_3, Phys. Rev. B **30** (1984), 3240–3249.

[108] J. Tauc, R. Grigorovici, and A. Vancu, *Optical Properties and Electronic Structure of Amorphous Germanium*, Phys. Status Solidi B **15** (1966), 627–637.

[109] V. Srikant and D. R. Clarke, *On the optical band gap of zinc oxide*, J. Appl. Phys. **83** (1998), 5447–5451.

[110] A. Ohtomo, M. Kawasaki, T. Koida, K. Masubuchi, H. Koinuma, Y. Sakurai, Y. Yoshida, T. Yasuda, and Y. Segawa, $Mg_xZn_{1-x}O$ *as a II–VI widegap semiconductor alloy*, Appl. Phys. Lett. **72** (1998), 2466–2468.

[111] S. A. Studenikin, N. Golego, and M. Cocivera, *Optical and electrical properties of undoped ZnO films grown by spray pyrolysis of zinc nitrate solution*, J. Appl. Phys. **83** (1998), 2104–2111.

[112] F. Paraguay, W. Estrada, D. Acosta, E. Andrade, and M. Miki-Yoshida, *Growth, structure and optical characterization of high quality ZnO thin films obtained by spray pyrolysis*, Thin Solid Films **350** (1999), 192 – 202.

[113] X. Meng, W. Zhen, J. Guo, and X. Fan, *Structural, optical and electrical properties of ZnO and ZnO-*Al_2O_3 *films prepared by dc magnetron sputtering*, Appl. Phys. A - Mater. **70** (2000), 421–424.

[114] T. Minemoto, T. Negami, S. Nishiwaki, H. Takakura, and Y. Hamakawa, *Preparation of* $Zn_{1-x}Mg_xO$ *films by radio frequency magnetron sputtering*, Thin Solid Films **372** (2000), 173 – 176.

[115] K. Postava, H. Sueki, M. Aoyama, T. Yamaguchi, C. Ino, Y. Igasaki, and M. Horie, *Spectroscopic ellipsometry of epitaxial ZnO layer on sapphire substrate*, J. Appl. Phys. **87** (2000), 7820–7824.

[116] G. Santana, A. Morales-Acevedo, O. Vigil, L. Vaillant, F. Cruz, and G. Contreras-Puente, *Structural and optical properties of* ZnO_xCdO_{1-x} *thin films obtained by spray pyrolysis*, Thin Solid Films **373** (2000), 235 – 238.

[117] Y. R. Park and K. J. Kim, *Optical and electrical properties of Ti-doped ZnO films: observation of semiconductor-metal transition*, Solid State Commun. **123** (2002), 147 – 150.

[118] M. Tokumoto, A. Smith, C. Santilli, S. Pulcinelli, A. Craievich, E. Elkaim, A. Traverse, and V. Briois, *Structural electrical and optical properties of undoped and indium doped ZnO thin films prepared by the pyrosol process at different temperatures*, Thin Solid Films **416** (2002), 284 – 293.

[119] I. Takeuchi, W. Yang, K.-S. Chang, M. A. Aronova, T. Venkatesan, R. D. Vispute, and L. A. Bendersky, *Monolithic multichannel ultraviolet detector arrays and continuous phase evolution in* $Mg_xZn_{1-x}O$ *composition spreads*, J. Appl. Phys. **94** (2003), 7336–7340.

[120] J. Chen, W. Z. Shen, N. B. Chen, D. J. Qiu, and H. Z. Wu, *The study of composition non-uniformity in ternary* $Mg_xZn_{1-x}O$ *thin films*, J. Phys.: Condens. Matter **15** (2003), L475.

[121] F. Shan and Y. Yu, *Optical properties of pure and Al doped ZnO thin films fabricated with plasma produced by excimer laser*, Thin Solid Films **435** (2003), 174 – 178.

[122] P. Misra, P. Sahoo, P. Tripathi, V. Kulkarni, R. Nandedkar, and L. Kukreja, *Sequential pulsed laser deposition of* $Cd_xZn_{1-x}O$ *alloy thin films for engineering ZnO band gap*, Appl. Phys. A - Mater. **78** (2004), 37–40.

[123] F. K. Shan, B. I. Kim, G. X. Liu, Z. F. Liu, J. Y. Sohn, W. J. Lee, B. C. Shin, and Y. S. Yu, *Blueshift of near band edge emission in Mg doped ZnO thin films and aging*, J. Appl. Phys. **95** (2004), 4772–4776.

[124] J.-L. Zhao, X.-M. Li, J.-M. Bian, W.-D. Yu, and X.-D. Gao, *Structural, optical and electrical properties of ZnO films grown by pulsed laser deposition (PLD)*, J. Cryst. Growth **276** (2005), 507 – 512.

[125] A. J. Bard, R. Parsons, and J. Jordan (eds.), *Standard Potentials in Aqueous Solutions*, Dekker, New York, 1985.

[126] D. J. G. Ives and G. J. Janz (eds.), *Reference Electrodes*, Academic Press, New York, 1961.

[127] M. A. Butler and D. S. Ginley, *Prediction of Flatband Potentials at Semiconductor-Electrolyte Interfaces from Atomic Electronegativities*, J. Electrochem. Soc. **125** (1978), 228–232.

[128] C. A. Koval and J. N. Howard, *Electron transfer at semiconductor electrode-liquid electrolyte interfaces*, Chem. Rev. **92** (1992), 411–433.

[129] A. D. McNaught and A. Wilkinson, *IUPAC Compendium of Chemical Terminology*, 2nd ed., Blackwell Scientific Publications, Oxford, 1997, http://goldbook.iupac.org/S05917.html.

[130] W. Schmickler and E. Santos, *Interfacial electrochemistry*, 2nd ed., Springer, Heidelberg, 2010.

[131] J. R. Vilche, K. Jüttner, W. J. Lorenz, W. Kautek, W. Paatsch, M. H. Dean, and U. Stimming, *Semiconductor Properties of Passive Films on Zn, Zn-Co, and Zn-Ni Substrates*, J. Electrochem. Soc. **136** (1989), 3773–3779.

[132] X. G. Zhang, *Corrosion and Electrochemistry of Zinc*, Springer, New York, 1996.

[133] S. R. Morrison, *Electrochemistry at Semiconductor and Oxidized Metal Electrodes*, Plenum Press, New York, 1980.

[134] Y. V. Pleskov and Y. Y. Gurevch, *Semiconductor Photoelectrochemistry*, Consultants Bureau, New York, 1986.

[135] R. Memming, *Semiconductor electrochemistry*, Weinheim, Wiley-VCH, 2001.

[136] L. Blok and P. L. D. Bruyn, *The ionic double layer at the ZnOsolution interface: I. The experimental point of zero charge*, J. Colloid Interface Sci. **32** (1970), 518 – 526.

[137] G. A. Parks, *The Isoelectric Points of Solid Oxides, Solid Hydroxides, and Aqueous Hydroxo Complex Systems*, Chem. Rev. **65** (1965), 177–198.

[138] J. O. M. Bockris, A. K. N. Reddy, and M. E. Galboa-Aldeco, *Modern Electrochemistry 2A - Fundamentals of Electrodics*, Springer, New York, 2001.

[139] C. Hamann, A. Hamnett, and W. Vielstrich, *Electrochemistry*, 2nd ed., Wiley, 2007.

[140] Y. Matsumoto, T. Yoshikawa, and E.-i. Sato, *Dependence of the Band Bending of the Oxide Semiconductors on pH*, J.Electrochem. Soc. **136** (1989), 1389–1391.

[141] T. Freund and S. Roy Morrison, *Mechanism of cathodic processes on the semiconductor zinc oxide*, Surf. Sci. **9** (1968), 119–132.

[142] R. Vanden Berghe, F. Cardon, and W. Gomes, *On the electrochemical reactivity of the redox couple Fe(CN)63-/Fe(CN)64- at the single crystal zinc oxide electrode*, Surf. Sci. **39** (1973), 368–384.

[143] J. Dewald, *The charge distribution at the zinc oxide-electrolyte interface*, J. Physics Chem. Solids **14** (1960), 155 – 161.

[144] F. Lohmann, *Der Einfluß des pH auf die elektrischen und chemischen Eigenschaften von Zinkoxidelektroden*, Ber. Bunsen. phys. Chem. **70** (1966), 428–434.

[145] B. Pettinger, H.-R. Schöppel, T. Yokoyama, and H. Gerischer, *Tunnelling Processes at Highly Doped ZnO-Electrodes in Aqueous Electrolytes Part II: Electron Exchange with the Valence Band*, Ber. Bunsen. phys. Chem. **78** (1974), 1024–1030.

[146] A. R. de Wit, M. D. Janssen, and J. J. Kelly, *Electrochemical characterization of polycrystalline ZnO layers*, Appl. Surf. Sci. **45** (1990), 21 – 27.

[147] S. Morrison and T. Freund, *Chemical reactions of electrons and holes at the ZnO/electrolyte-solution interface*, Electrochim. Acta **13** (1968), 1343 – 1349.

[148] S. R. Morrison and T. Freund, *Chemical Role of Holes and Electrons in ZnO Photocatalysis*, J. Chem. Phys. **47** (1967), 1543–1551.

[149] S. R. Morrison, *Electron capture by ions at the ZnO/solution interface*, Surf. Sci. **15** (1969), 363 – 379.

[150] B. Pettinger, H.-R. Schöppel, and H. Gerischer, *Tunnelling Processes at Highly Doped ZnO Electrodes in Contact with Aqueous Electrolytes. I. Electron Exchange with the Conduction Band*, Ber. Bunsen. phys. Chem. **78** (1974), 450–455.

[151] S. Fletcher, *The theory of electron transfer*, J. Solid State Electrochem. **14** (2010), 705–739.

[152] M. Pourbaix, *Atlas of Electrochemical Equilibria in Aqueous Solutions*, 2 ed., National Association of Corrosion Engineers, Houston, 1974.

[153] H. Gerischer and N. Sorg, *Chemical dissolution of zinc oxide crystals in aqueous electrolytes–An analysis of the kinetics*, Electrochim. Acta **37** (1992), 827 – 835.

[154] H. Gerischer, *Electrochemical Behavior of Semiconductors under Illumination*, J. Electrochem. Soc. **113** (1966), 1174–1182.

[155] H. Gerischer, *On the stability of semiconductor electrodes against photodecomposition*, J. Electroanal. Chem. **82** (1977), 133–143.

[156] S. Peulon and D. Lincot, *Cathodic electrodeposition from aqueous solution of dense or open-structured zinc oxide films*, Adv. Mater. **8** (1996), 166–170.

[157] M. Izaki and T. Omi, *Electrolyte Optimization for Cathodic Growth of Zinc Oxide Films*, J. Electrochem. Soc. **143** (1996), L53–L55.

[158] H. El Belghiti, T. Pauporté, and D. Lincot, *Mechanistic study of ZnO nanorod array electrodeposition*, Phys. Status Solidi A **205** (2008), 2360–2364.

[159] Z. Jehl, J. Rousset, F. Donsanti, G. Renou, N. Naghavi, and D. Lincot, *Electrodeposition of ZnO nanorod arrays on ZnO substrate with tunable orientation and optical properties*, Nanotechnology **21** (2010), 395603.

[160] M. D. R. Tolosa, J. Orozco-Messana, A. N. C. Lima, R. Camaratta, M. Pascual, and M. A. Hernandez-Fenollosa, *Electrochemical Deposition Mechanism for ZnO Nanorods: Diffusion Coefficient and Growth Models*, J. Electrochem. Soc. **158** (2011), E107–E110.

[161] G. She, X. Zhang, W. Shi, X. Fan, and J. C. Chang, *Electrochemical/chemical synthesis of highly-oriented single-crystal ZnO nanotube arrays on transparent conductive substrates*, Electrochem. Commun. **9** (2007), 2784–2788.

[162] J. Elias, R. Tena-Zaera, G.-Y. Wang, and C. Lévy-Clément, *Conversion of ZnO Nanowires into Nanotubes with Tailored Dimensions*, Chem. Mater. **20** (2008), 6633–6637.

[163] F. Xu, J. Chen, L. Guo, S. Lei, and Y. Ni, *In situ electrochemically etching-derived ZnO nanotube arrays for highly efficient and facilely recyclable photocatalyst*, Appl. Surf. Sci. **258** (2012), 8160–8165.

[164] T. Yoshida, M. Tochimoto, D. Schlettwein, D. Wöhrle, T. Sugiura, and H. Minoura, *Self-Assembly of Zinc Oxide Thin Films Modified with Tetrasulfonated Metallophthalocyanines by One-Step Electrodeposition*, Chem. Mater. **11** (1999), 2657–2667.

[165] A. Goux, T. Pauporté, T. Yoshida, and D. Lincot, *Mechanistic Study of the Electrodeposition of Nanoporous Self-Assembled ZnO/Eosin Y Hybrid Thin Films: Effect of Eosin Concentration*, Langmuir **22** (2006), 10545–10553.

[166] T. Oekermann, *Electrodeposition of nanostructured ZnO films and their photoelectrochemical properties*, On solar hydrogen & nanotechnology (L. Vayssieres, ed.), Wiley, 2009, pp. 291–328.

[167] C. Dunkel, F. Lüttich, H. Graaf, T. Oekermann, and M. Wark, *Investigation of the pulsed electrochemical deposition of ZnO*, Electrochim. Acta **80** (2012), 60–67.

[168] M. Fu, J. Cui, M. Yang, R. Jiang, D. He, and Y. Wang, *Template effects on the morphology of ZnO via colloidal crystals with different functional groups*, Cryst. Res. Technol. **47** (2012), 1249–1254.

[169] T. Pauporté and D. Lincot, *Heteroepitaxial electrodeposition of zinc oxide films on gallium nitride*, Appl. Phys. Lett. **75** (1999), 3817–3819.

[170] B. Canava and D. Lincot, *Nucleation effects on structural and optical properties of electrodeposited zinc oxide on tin oxide*, J. Appl. Electrochem. **30** (2000), 711–716.

[171] T. Pauporté, D. Lincot, B. Viana, and F. Pellé, *Toward laser emission of epitaxial nanorod arrays of ZnO grown by electrodeposition*, Appl. Phys. Lett. **89** (2006), 233112.

[172] Z. H. Gu and T. Z. Fahidy, *Electrochemical Deposition of ZnO Thin Films on Tin-Coated Glasses*, J. Electrochem. Soc. **146** (1999), 156–159.

[173] T. Shinagawa, M. Chigane, K. Murase, and M. Izaki, *Drastic Change in Electrical Properties of Electrodeposited ZnO: Systematic Study by Hall Effect Measurements*, J. Phys. Chem. C **116** (2012), 15925–15931.

[174] T. Pauporté and D. Lincot, *Hydrogen peroxide oxygen precursor for zinc oxide electrodeposition II–Mechanistic aspects*, J. Electroanal. Chem. **517** (2001), 54–62.

[175] A. El Hichou, N. Stein, C. Boulanger, and L. Johann, *Structural and spectroscopic ellipsometry characterization for electrodeposited ZnO growth at different hydrogen peroxide concentration*, Thin Solid Films **518** (2010), 4150–4155.

[176] A. Ashida, N. Nouzu, and N. Fujimura, *Initial Growth Process in Electrochemical Deposition of ZnO*, Jpn. J. Appl. Phys. **50** (2011), 05FB12.

[177] A. Goux, T. Pauporte, J. Chivot, and D. Lincot, *Temperature effects on ZnO electrodeposition*, Electrochim. Acta **50** (2005), 2239–2248.

[178] B. Prasad, P. Kamath, and S. Ranganath, *Electrodeposition of ZnO coatings from aqueous Zn(NO$_3$)$_2$ baths: effect of Zn concentration, deposition temperature, and time on orientation*, J. Solid State Electrochem. **16** (2012), 3715–3722.

[179] S. Otani, J. Katayama, H. Umemoto, and M. Matsuoka, *Effect of bath temperature on the electrodeposition mechanism of zinc oxide film from zinc nitrate solution*, J. Electrochem. Soc. **153** (2006), C551–C556.

[180] E. Elsayed, F. Harraz, and A. Saba, *Nanocrystalline zinc oxide thin films prepared by electrochemical technique for advanced applications*, Inter. J. Nanoparticles **5** (2012), 136–148.

[181] R. Salazar, C. Lévy-Clément, and V. Ivanova, *Galvanostatic deposition of ZnO thin films*, Electrochim. Acta **78** (2012), 547–556.

[182] J. A. Cox and A. Brajter, *Mechanisms of Zr(IV) and La(III) catalysis of the reduction of nitrate at mercury*, Electrochim. Acta **24** (1979), 517 – 520.

[183] N. Ogawa and S. Ikeda, *On the electrochemical reduction of nitrate ion in the presence of varius metal ions*, Anal. Sci. **7** (1991), 1681–1684.

[184] T. Yoshida, D. Komatsu, N. Shimokawa, and H. Minoura, *Mechanism of cathodic electrodeposition of zinc oxide thin films from aqueous zinc nitrate baths*, Thin Solid Films **451-452** (2004), 166–169.

[185] M. R. Khajavi, D. J. Blackwood, G. Cabanero, and R. Tena-Zaera, *New insight into growth mechanism of ZnO nanowires electrodeposited from nitrate-based solutions*, Electrochim. Acta **69** (2012), 181 – 189.

[186] M. Izaki, *Preparation of Transparent and Conductive Zinc Oxide Films by Optimization of the Two-Step Electrolysis Technique*, J. Electrochem. Soc. **146** (1999), 4517–4521.

[187] J. Wellings, N. Chaure, S. Heavens, and I. Dharmadasa, *Growth and characterisation of electrodeposited ZnO thin films*, Thin Solid Films **516** (2008), 3893–3898.

[188] X.-D. Gao, F. Peng, X.-M. Li, W.-D. Yu, and J.-J. Qiu, *Growth of highly oriented ZnO films by the two-step electrodeposition technique*, J. Mater. Sci. **42** (2007), 9638–9644.

[189] B. N. Illy, A. C. Cruickshank, S. Schumann, R. Da Campo, T. S. Jones, S. Heutz, M. A. McLachlan, D. W. McComb, D. J. Riley, and M. P. Ryan, *Electrodeposition of ZnO layers for photovoltaic applications: controlling film thickness and orientation*, J. Mater. Chem. **21** (2011), 12949–12957.

[190] M. A. Thomas and J. B. Cui, *Highly Uniform 2D Growth, Substrate Transfer, and Electrical Characterization of Electrodeposited ZnO Thin Films*, J. Electrochem. Soc. **160** (2013), D218–D225.

[191] T. Sumida, Y. Wada, T. Kitamura, and S. Yanagida, *Macroporous ZnO Films Electrochemically Prepared by Templating of Opal Films*, Chemistry Letters **30** (2001), 38–39.

[192] Z. Liu, Z. Jin, J. Qiu, X. Liu, W. Wu, and W. Li, *Preparation and characteristics of ordered porous ZnO films by a electrodeposition method using PS array templates*, Semicond. Sci. Tech. **21** (2006), 60–66.

[193] M. Fu, J. Zhou, X. G. Huang, D. W. He, and Y. S. Wang, *The Electrodeposition of Zinc Oxide Two-Dimensional Nanomesh and Three-Dimensional Inverse Opal Complex Connected Structures*, J. Nanosci. Nanotechnol. **10** (2010), 1928–1933.

[194] Y.-J. Huang, C.-H. Liao, B.-H. Huang, W.-Y. Chen, and P.-W. Wu, *Facile Electrochemical Fabrication of Large-Area ZnO Inverse Opals with Reduced Defects*, J. Electrochem. Soc. **158** (2011), P45–P49.

[195] C. V. D'Alkaine and M. N. Boucherit, *Potentiostatic Growth of ZnO on Zn: Application of an Ohmic Model*, J. Electrochem. Soc. **144** (1997), 3331–3336.

[196] M. Nobial, O. Devos, and B. Tribollet, *Electrochemical and in situ optical investigations of ZnO deposition*, J. Cryst. Growth **327** (2011), 173–181.

[197] S. Sanchez, C. Chappaz-Gillot, R. Salazar, H. Muguerra, E. Arbaoui, S. Berson, C. Lévy-Clément, and V. Ivanova, *Comparative study of ZnO and CuSCN semiconducting nanowire electrodeposition on different substrates*, J. Solid State Electr. **17** (2013), 391–398.

[198] J. Cui and U. J. Gibson, *Enhanced Nucleation, Growth Rate, and Dopant Incorporation in ZnO Nanowires*, J. Phys. Chem. B **109** (2005), 22074–22077.

[199] K. Laurent, D. Yu, and Y. Leprince-Wang, *Anodic electrodeposition of ZnO onto p-Si substrates assisted by light irradiation*, J. Appl. Electrochem. **40** (2010), 1455–1460.

[200] A. E. Rakhshani, *Optoelectronic properties of p-n and p-i-n heterojunction devices prepared by electrodeposition of n-ZnO on p-Si*, J. Appl. Phys. **108** (2010), 094502.

[201] T. Singh, D. Pandya, and R. Singh, *Concentration dependent structural and optical properties of electrochemically grown ZnO thin films and nanostructures*, Appl. Surf. Sci. **270** (2013), 578–583.

[202] T. Pauporté and D. Lincot, *Electrodeposition of semiconductors for optoelectronic devices: results on zinc oxide*, Electrochim. Acta **45** (2000), 3345–3353.

[203] G. Guerguerian, F. Elhordoy, C. J. Pereyra, R. E. Marotti, F. Martin, D. Leinen, J. R. Ramos-Barrado, and E. A. Dalchiele, *ZnO/Cu_2O heterostructure nanopillar arrays: synthesis, structural and optical properties*, J. Phys. D: Appl. Phys. **45** (2012), 245301.

[204] V. Donderis, J. Orozco, J. Cembrero, J. Curiel-Esparza, L. Damonte, and M. Hernandez-Fenollosa, *Doped nanostructured zinc oxide films grown by electrodeposition*, J. Nanosci. Nanotechnol. **10** (2010), 1387–1392.

[205] M. Tolosa, J. Orozco-Messana, L. Damonte, and M. Hernandez-Fenollosa, *ZnO nanostructured layers processing with morphology control by pulsed electrodeposition*, J. Electrochem. Soc. **158** (2011), D452–D455.

[206] M. Fahoume, O. Maghfoul, M. Aggour, B. Hartiti, F. Chraibi, and A. Ennaoui, *Growth and characterization of ZnO thin films prepared by electrodeposition technique*, Sol. Energy Mater. Sol. Cells **90** (2006), 1437–1444.

[207] C.-T. Hsieh, S.-Y. Yang, J.-L. Gu, and Y.-R. Jiang, *Influence of growth parameters on texture of ZnO nanorods by using electrochemical deposition at low temperatures*, Solid State Ionics **209–210** (2012), 43–50.

[208] M. Khelladi, L. Mentar, M. Boubatra, and A. Azizi, *Study of nucleation and growth process of electrochemically synthesized ZnO nanostructures*, Mater. Lett. **67** (2012), 331–333.

[209] K. Ichinose, Y. Kimikado, and T. Yoshida, *The Effect of Pre-treatments of F-Doped SnO_2 Substrates for Cathodic Nucleation of ZnO Crystals in Aqueous $ZnCl_2$ Solution with Dissolved O_2*, Electrochemistry **79** (2011), 146–155.

[210] K. Lovchinov, M. Ganchev, A. Rachkova, H. Nichev, O. Angelov, V. Mikli, and D. Dimova-Malinovska, *Structural and optical properties of electrochemically*

deposited ZnO films in electrolyte containing $Al_2(SO_4)_3$, J. Phys. Conf. Ser. **398** (2012), 012018.

[211] A. Peic, T. Dimopoulos, R. Resel, S. Abermann, M. Postl, E. J. W. List, and H. Brückl, *Effect of AZO Substrates on Self-Seeded Electrochemical Growth of Vertically Aligned ZnO Nanorod Arrays and Their Optical Properties*, J. Nanomater. **2012** (2012), 14.

[212] H. Lee, M. Kim, and J. Yu, *Effect of AZO seed layer on electrochemical growth and optical properties of ZnO nanorod arrays on ITO glass*, Nanotechnology **22** (2011), 445602.

[213] M. D. R. Tolosa, L. C. Damonte, H. Brine, H. J. Bolink, and M. A. Hernández-Fenollosa, *Nucleant layer effect on nanocolumnar ZnO films grown by electrodeposition*, Nanoscale Res. Lett. **8** (2013), 1–6.

[214] D. Gal, G. Hodes, D. Lincot, and H. W. Schock, *Electrochemical deposition of zinc oxide films from non-aqueous solution: a new buffer/window process for thin film solar cells*, Thin Solid Films **361-362** (2000), 79–83.

[215] R. Jayakrishnan and G. Hodes, *Non-aqueous electrodeposition of ZnO and CdO films*, Thin Solid Films **440** (2003), 19–25.

[216] Z. Liu, X. Lu, S. Xie, J. Zhang, Z. Liu, and Y. Tong, *Facile Electrochemical Synthesis of ZnO/ZnS Heterostructure Nanorod Arrays*, J. Electrochem. Soc. **158** (2011), E84–E87.

[217] G. Riveros, D. Ramírez, A. Tello, R. Schrebler, R. Henríquez, and H. Gómez, *Electrodeposition of ZnO from DMSO solution: influence of anion nature and its concentration in the nucleation and growth mechanisms*, J. Braz. Chem. Soc. **23** (2012), 505.

[218] H. Gomez, G. Riveros, D. Ramirez, R. Henriquez, R. Schrebler, R. Marotti, and E. Dalchiele, *Growth and characterization of ZnO nanowire arrays electrodeposited into anodic alumina templates in DMSO solution*, J. Solid State Electr. **16** (2012), 197–204.

[219] B. O'Regan, V. Sklover, and M. Grätzel, *Electrochemical Deposition of Smooth and Homogeneously Mesoporous ZnO Films from Propylene Carbonate Electrolytes*, J. Electrochem. Soc. **148** (2001), C498–C505.

[220] M. Morisue, M. Nambu, H. Osaki, and Y. Fukunaka, *ZnO thin films electrodeposited in propylene carbonate under a magnetic field*, J. Solid State Electrochem. **11** (2007), 719–726.

[221] E. Azaceta, R. Marcilla, D. Mecerreyes, M. Ungureanu, A. Dev, T. Voss, S. Fantini, H.-J. Grande, G. Cabanero, and R. Tena-Zaera, *Electrochemical reduction of O_2 in 1-butyl-1-methylpyrrolidinium bis(trifluoromethanesulfonyl)imide ionic liquid containing Zn^{2+} cations: deposition of non-polar oriented ZnO nanocrystalline films*, Phys. Chem. Chem. Phys. **13** (2011), 13433–13440.

[222] H. Ishizaki, M. Izaki, and T. Ito, *Influence of $(CH_3)_2NHBH_3$ Concentration on Electrical Properties of Electrochemically Grown ZnO Films*, J. Electrochem. Soc. **148** (2001), C540–C543.

[223] H. Ishizaki, M. Imaizumi, S. Matsuda, M. Izaki, and T. Ito, *Incorporation of boron in ZnO film from an aqueous solution containing zinc nitrate and dimethylamine-borane by electrochemical reaction*, Thin Solid Films **411** (2002), 65 – 68.

[224] R. Könenkamp, K. Boedecker, M. C. Lux-Steiner, M. Poschenrieder, F. Zenia, C. Lévy-Clément, and S. Wagner, *Thin film semiconductor deposition on free-standing ZnO columns*, Appl. Phys. Lett. **77** (2000), 2575–2577.

[225] M. Kemell, F. Dartigues, M. Ritala, and M. Leskelä, *Electrochemical preparation of In and Al doped ZnO thin films for $CuInSe_2$ solar cells*, Thin Solid Films **434** (2003), 20 – 23.

[226] J. S. Wellings, A. P. Samantilleke, P. Warren, S. N. Heavens, and I. M. Dharmadasa, *Comparison of electrodeposited and sputtered intrinsic and aluminium-doped zinc oxide thin films*, Semicond. Sci. Tech. **23** (2008), 125003.

[227] J. Chen, H. Ye, L. Aé, Y. Tang, D. Kieven, T. Rissom, J. Neuendorf, and M. C. Lux-Steiner, *Tapered aluminum-doped vertical zinc oxide nanorod arrays as light coupling layer for solar energy applications*, Sol. Energy Mater. Sol. Cells **95** (2011), 1437–1440.

[228] G. Machado, D. Guerra, D. Leinen, J. Ramos-Barrado, R. Marotti, and E. Dalchiele, *Indium doped zinc oxide thin films obtained by electrodeposition*, Thin Solid Films **490** (2005), 124 – 131.

[229] O. Lupan, T. Pauporté, B. Viana, and P. Aschehoug, *Electrodeposition of Cu-doped ZnO nanowire arrays and heterojunction formation with p-GaN for*

color tunable light emitting diode applications, Electrochim. Acta **56** (2011), 10543–10549.

[230] J. Rousset, E. Saucedo, and D. Lincot, *Extrinsic Doping of Electrodeposited Zinc Oxide Films by Chlorine for Transparent Conductive Oxide Applications*, Chem. Mater. **21** (2009), 534–540.

[231] J. Fan, A. Shavel, R. Zamani, C. Fábrega, J. Rousset, S. Haller, F. Güell, A. Carrete, T. Andreu, J. Arbiol, J. R. Morante, and A. Cabot, *Control of the doping concentration, morphology and optoelectronic properties of vertically aligned chlorine-doped ZnO nanowires*, Acta Mater. **59** (2011), 6790–6800.

[232] J. Rousset, F. Donsanti, P. Genevée, G. Renou, and D. Lincot, *High efficiency cadmium free Cu(In,Ga)Se$_2$ thin film solar cells terminated by an electrodeposited front contact*, Sol. Energy Mater. Sol. Cells **95** (2011), 1544–1549.

[233] J. Rousset, E. Saucedo, K. Herz, and D. Lincot, *High efficiency CIGS based solar cells with electrodeposited ZnO:Cl as transparent conducting oxide front contact*, Prog. Photovoltaics **19** (2011), 537–546.

[234] R. P. Raffaelle, W. Junek, J. Gorse, T. Thompson, J. D. Harris, J. Cowen, D. Hehemann, G. Rybicki, and A. F. Hepp, *Wet-Chemical Synthesis of Thin-Film Solar Cells*, Mater. Res. Soc. Symp. Proc. **606** (2000), 155–162.

[235] N. Toyama, R. Hayashi, Y. Sonoda, M. Iwata, Y. Miyamoto, H. Otoshi, K. Saito, and K. Ogawa, *Electrochemically deposited zinc oxide for light trapping in thin film solar cells*, 3rd World Conference on Photovoltaic Energy Conversion (2003), 1601–1604.

[236] D. Attygalle, Q. H. Fan, S. Zhang, W. Ingler, X. Liao, and X. Deng, *Fabrication and Performance of Highly Textured Electrodeposited ZnO Back Reflector for nc-Si Solar Cells*, Mater. Res. Soc. Symp. Proc. **1123** (2009), 41–46.

[237] S. Karuppuchamy, K. Nonomura, T. Yoshida, T. Sugiura, and H. Minoura, *Cathodic electrodeposition of oxide semiconductor thin films and their application to dye-sensitized solar cells*, Solid State Ionics **151** (2002), 19–27.

[238] Y. Gao and M. Nagai, *Morphology evolution of ZnO thin films from aqueous solutions and their application to solar cells*, Langmuir **22** (2006), 3936–3940.

[239] V.-M. Guérin and T. Pauporté, *From nanowires to hierarchical structures of template-free electrodeposited ZnO for efficient dye-sensitized solar cells*, Energy Environ. Sci. **4** (2011), 2971–2979.

[240] C. Magne, T. Moehl, M. Urien, M. Grätzel, and T. Pauporte, *Effects of ZnO film growth route and nanostructure on electron transport and recombination in dye-sensitized solar cells*, J. Mater. Chem. A **1** (2013), 2079–2088.

[241] C. Dunkel, M. Wark, T. Oekermann, R. Ostermann, and B. M. Smarsly, *Electrodeposition of zinc oxide on transparent conducting metal oxide nanofibers and its performance in dye sensitized solar cells*, Electrochim. Acta **90** (2013), 375–381.

[242] O. Lupan, T. Pauporté, I. Tiginyanu, V. Ursaki, H. Heinrich, and L. Chow, *Optical properties of ZnO nanowire arrays electrodeposited on n- and p-type Si(111): Effects of thermal annealing*, Mater. Sci. Eng. B-Adv. **176** (2011), 1277–1284.

[243] W.-J. Li, E.-W. Shi, W.-Z. Zhong, and Z.-W. Yin, *Growth mechanism and growth habit of oxide crystals*, J. Cryst. Growth **203** (1999), 186 – 196.

[244] J. Elias, R. Tena-Zaera, and C. Lévy-Clément, *Effect of the Chemical Nature of the Anions on the Electrodeposition of ZnO Nanowire Arrays*, J. Phys. Chem. C **112** (2008), 5736–5741.

[245] R. Tena-Zaera, J. Elias, G. Wang, and C. Lévy-Clément, *Role of Chloride Ions on Electrochemical Deposition of ZnO Nanowire Arrays from O_2 Reduction*, J. Phys. Chem. C **111** (2007), 16706–16711.

[246] Q.-P. Chen, M.-Z. Xue, Q.-R. Sheng, Y.-G. Liu, and Z.-F. Ma, *Electrochemical Growth of Nanopillar Zinc Oxide Films by Applying a Low Concentration of Zinc Nitrate Precursor*, Electrochem. Solid St. **9** (2006), C58–C61.

[247] R. Tena-Zaera, J. Elias, C. Lévy-Clément, C. Bekeny, T. Voss, I. Mora-Seró, and J. Bisquert, *Influence of the Potassium Chloride Concentration on the Physical Properties of Electrodeposited ZnO Nanowire Arrays*, J. Phys. Chem. C **112** (2008), 16318–16323.

[248] S. Sun, S. Jiao, K. Zhang, D. Wang, S. Gao, H. Li, J. Wang, Q. Yu, F. Guo, and L. Zhao, *Nucleation effect and growth mechanism of ZnO nanostructures by electrodeposition from aqueous zinc nitrate baths*, J. Cryst. Growth **359** (2012), 15–19.

[249] L. Xu, Y. Guo, Q. Liao, J. Zhang, and D. Xu, *Morphological control of ZnO nanostructures by electrodeposition*, J. Phys. Chem. B **109** (2005), 13519–13522.

[250] N. F. Foster, *Crystallographic Orientation of Zinc Oxide Films Deposited by Triode Sputtering*, J. Vac. Sci. Technol. **6** (1969), 111–114.

[251] S. Sun, S. Jiao, K. Zhang, D. Wang, H. Li, S. Gao, J. Wang, Q. Yu, F. Guo, L. Zhao, and S. Su, *Morphology and properties of ZnO nanostructures by electrochemical deposition: effect of the substrate treatment*, J. Mater. Sci.: Mater. Electron. **24** (2013), 85–88.

[252] N. Orhan and M. Baykul, *Characterization of size-controlled ZnO nanorods produced by electrochemical deposition technique*, Solid State Electron. **78** (2012), 147–150.

[253] O. Lupan, T. Pauporté, I. Tiginyanu, V. Ursaki, V. Sontea, L. Ono, B. R. Cuenya, and L. Chow, *Comparative study of hydrothermal treatment and thermal annealing effects on the properties of electrodeposited micro-columnar ZnO thin films*, Thin Solid Films **519** (2011), 7738–7749.

[254] S. Yoon, I. Huh, J.-H. Lim, and B. Yoo, *Annealing effects on electrical and optical properties of ZnO thin films synthesized by the electrochemical method*, Curr. Appl. Phys. **12** (2012), 784 – 788.

[255] J. Stiegler, R. Tena-Zaera, O. Idigoras, A. Chuvilin, and R. Hillenbrand, *Correlative infrared-electron nanoscopy reveals the local structure-conductivity relationship in zinc oxide nanowires*, Nat. Commun. **3** (2012), 1131.

[256] H.-J. Engell, *Die elektrochemische Bestimmung der Abweichungen von der Stöchiometrie in Metalloxyden*, Z. Elektrochem. **60** (1956), 905–911.

[257] T. Kawaharamura and T. Hirao, *Development and Research on the Mechanism of Novel Mist Etching Method for Oxide Thin Films*, Jpn. J. Appl. Phys. **51** (2012), 036503.

[258] Z. Zembura and L. Burzynska, *The corrosion of zinc in de-aerated 0.1 M NaCl in the pH range from 1.6 to 13.3*, Corros. Sci. **17** (1977), 871 – 878.

[259] L. Sziráki, A. Cziráki, I. Geröcs, Z. Vértesy, and L. Kiss, *A kinetic model of the spontaneous passivation and corrosion of zinc in near neutral Na_2SO_4 solutions*, Electrochim. Acta **43** (1998), 175–186.

[260] M. A. Amin, *Passivity and passivity breakdown of a zinc electrode in aerated neutral sodium nitrate solutions*, Electrochim. Acta **50** (2005), 1265–1274.

[261] D.-G. Yoo, S.-H. Nam, M. H. Kim, S. H. Jeong, H.-G. Jee, H. J. Lee, N.-E. Lee, B. Y. Hong, Y. J. Kim, D. Jung, and J.-H. Boo, *Fabrication of the ZnO thin films using wet-chemical etching processes on application for organic light emitting diode (OLED) devices*, Surf. Coat. Technol. **202** (2008), 5476–5479.

[262] O. Kluth, B. Rech, L. Houben, S. Wieder, G. Schöpe, C. Beneking, H. Wagner, A. Löffl, and H. Schock, *Texture etched ZnO:Al coated glass substrates for silicon based thin film solar cells*, Thin Solid Films **351** (1999), 247–253.

[263] J. Hüpkes, J. I. Owen, S. E. Pust, and E. Bunte, *Chemical Etching of Zinc Oxide for Thin-Film Silicon Solar Cells*, ChemPhysChem **13** (2012), 66–73.

[264] J. I. Owen, S. E. Pust, E. Bunte, and J. Hüpkes, *ZnO Etch-Feature Control via Concentration and Temperature of Various Acids*, ECS J. Solid State Sci. Technol. **1** (2012), P11–P17.

[265] A. N. Mariano and R. E. Hanneman, *Crystallographic Polarity of ZnO Crystals*, J. Appl. Phys. **34** (1963), 384–388.

[266] W. Jo, S.-J. Kim, and D.-Y. Kim, *Analysis of the etching behavior of ZnO ceramics*, Acta Mater. **53** (2005), 4185–4188.

[267] X. Han and M. Tao, *Electrodeposition of low-resistivity Y-doped ZnO and its thermal stability*, Photovoltaic Specialists Conference (PVSC), 2010 35th IEEE DOI - 10.1109/PVSC.2010.5615911, 2010, pp. 000305–000310.

[268] H. C. Gatos, *Dangling Bonds in III-V Compounds*, J. Appl. Phys. **32** (1961), 1232–1234.

[269] G. Heiland and P. Kunstmann, *Polar surfaces of zinc oxide crystals*, Surf. Sci. **13** (1969), 72–84.

[270] E. Palacios-Lidón, B. Pérez-García, P. Vennéguès, J. Colchero, V. Muñoz Sanjosé, and J. Zúñiga Pérez, *Anisotropic chemical etching of semipolar* $\{10\bar{1}\bar{1}\}/\{10\bar{1}{+}1\}$ *ZnO crystallographic planes: polarity versus dangling bonds*, Nanotechnology **20** (2009), 065701.

[271] S. O. Klemm, *Microelectrochemical characterization of Zn, ZnO and Zn-Mg alloys with online dissolution monitoring*, Ph.D. thesis, Ruhr-Universität Bochum, 2011.

[272] M. Valtiner, S. Borodin, and G. Grundmeier, *Stabilization and Acidic Dissolution Mechanism of Single-Crystalline ZnO(0001) Surfaces in Electrolytes Studied by In-Situ AFM Imaging and Ex-Situ LEED*, Langmuir **24** (2008), 5350–5358.

[273] O. Fruhwirth, G. Herzog, and J. Poulios, *Dark dissolution and photodissolution of ZnO*, Surf. Technol. **24** (1985), 293 – 300.

[274] B. Szyszka, V. Sittinger, W. Dewald, A. Pflug, S. Ulrich, A. Kaiser, and W. Werner, *Reactive Magnetron Sputtering of ZnO:Al - A Status Report*, 52^{nd} SVC Annual Technical Conference Proceedings, Santa Clara, CA, USA, Society of Vacuum Coaters, Albuquerque, NM, USA, 2009, pp. 42–48.

[275] H.-J. Engell, *Über die Auflösung von Oxyden in verdünnten Säuren*, Z. Phys. Chem. **7** (1956), 158–181.

[276] R. Williams, *Electrical Effects of the Dissolution of n-Type Zinc Oxide*, J. Appl. Phys. **39** (1968), 4089–4091.

[277] H. Erbse, K. Hauffe, and J. Range, *Über die Auflösung von Zinkoxid-Einkristallen in wäßrigen Lösungen unter Einwirkung elektrischer Felder*, Z. Phys. Chem. **74** (1971), 248–264.

[278] S. C. Abrahams and J. L. Bernstein, *Remeasurement of the structure of hexagonal ZnO*, Acta Crystallogr. B **25** (1969), 1233–1236.

[279] J. Hüpkes, J. I. Owen, E. Bunte, and S. E. Pust, *Etch Model for Zinc Oxide: Single Crystals and Polycrystalline Films*, Proceedings of the 26th European Photovoltaic Solar Energy Conference, Hamburg, Germany, WIP, Munich, 2011, pp. 2323–2324.

[280] J. I. Owen, J. Hüpkes, and E. Bunte, *Observation of the Evolution of Etch Features on Polycrystalline ZnO:Al Thin-Films*, Mater. Res. Soc. Symp. Proc. **1153** (2009), A07–08.

[281] N. Kumar, G. Zhang, N. Kalyankar, M. A. Nguyen, J. Li, H. Yang, and Z.-W. Sun, *High productivity combinatorial study of wet chemical texture etch of sputter deposited Al-doped ZnO thin films for thin film Si solar cells*, Photovolt. Internat. **9** (2010), 137–141.

[282] W.-L. Lu, K.-C. Huang, C.-H. Yeh, C.-I. Hung, and M.-P. Houng, *Investigation of textured Al-doped ZnO thin films using chemical wet-etching methods*, Mater. Chem. Phys. **127** (2011), 358–363.

[283] D. Inamdar, C. Agashe, P. Kadam, and S. Mahamuni, *Doping optimization and surface modification of aluminum doped zinc oxide films as transparent conductive coating*, Thin Solid Films **520** (2012), 3871–3877.

[284] H. Gerischer and N. Sorg, *Chemical dissolution of oxides: Experiments with Sintered ZnO pellets and ZnO single crystals*, Mater. Corros. **42** (1991), 149–157.

[285] E. Abd El Aal and S. Abd El Wanees, *Galvanostatic study of the breakdown of Zn passivity by sulphate anions*, Corros. Sci. **51** (2009), 1780–1788.

[286] G. Kilinççeker and H. Galip, *Electrochemical behaviour of zinc in chloride and acetate solutions.*, Prot. Met.Phys. Chem. Surf. **45** (2009), 232–240.

[287] J. Diggle (ed.), *The Anodic Behavior of Metals and Semiconductors*, Vol. 2: Oxides and Oxide Films, Marcel Dekker, New York, 1973.

[288] K. Heusler, *Oxide electrodes*, Electrochim. Acta **28** (1983), 439 – 449.

[289] R. Frankenthal and J. Kruger (eds.), *Passivity of Metals*, The Electrochemical Society, Princeton, 1978.

[290] K. Heusler, *The influence of electrolyte composition on the formation and dissolution of passivating films*, Corros. Sci. **29** (1989), 131 – 147.

[291] S. E. Pust, J.-P. Becker, J. Worbs, S. O. Klemm, K. J. J. Mayrhofer, and J. Hüpkes, *Electrochemical Etching of Zinc Oxide for Silicon Thin Film Solar Cell Applications*, J. Electrochem. Soc. **158** (2011), D413–D419.

[292] I. Mora-Seró, F. Fabregat-Santiago, B. Denier, J. Bisquert, R. Tena-Zaera, J. Elias, and C. Lévy-Clément, *Determination of carrier density of ZnO nanowires by electrochemical techniques*, Appl. Phys. Lett. **89** (2006), 203117–3.

[293] J. van den Meerakker, E. A. Meulenkamp, and M. Scholten, *(Photo)electrochemical Characterization of Tin-doped Indium Oxide*, J. Appl. Phys. **74** (1993), 3282–3288.

[294] S. O. Klemm, S. E. Pust, A. W. Hassel, J. Hüpkes, and K. J. J. Mayrhofer, *Electrochemical texturing of Al-doped ZnO thin films for photovoltaic applications*, J. Solid State Electr. **16** (2012), 283–290.

[295] L. Wang, G. Liu, and D. Xue, *Effects of introduced electrolytes on galvanic deposition of ZnO films*, Electrochim. Acta **55** (2010), 6796–6801.

[296] T. Yoshida, J. Zhang, D. Komatsu, S. Sawatani, H. Minoura, T. Pauporté, D. Lincot, T. Oekermann, D. Schlettwein, H. Tada, D. Wöhrle, K. Funabiki, M. Matsui, H. Miura, and H. Yanagi, *Electrodeposition of Inorganic/Organic Hybrid Thin Films*, Adv. Funct. Mater. **19** (2009), 17–43.

[297] A. Goux, T. Pauporté, and D. Lincot, *Oxygen reduction reaction on electrodeposited zinc oxide electrodes in KCl solution at 70°C*, Electrochim. Acta **51** (2006), 3168–3172.

[298] E. E. Foad El Sherbini and S. S. Abd El Rehim, *Pitting corrosion of zinc in* Na_2SO_4 *solutions and the effect of some inorganic inhibitors*, Corros. Sci. **42** (2000), 785–798.

[299] M. A. Amin, H. H. Hassan, and S. S. Abd El Rehim, *On the role of* NO_2^- *ions in passivity breakdown of Zn in deaerated neutral sodium nitrite solutions and the effect of some inorganic inhibitors: Potentiodynamic polarization, cyclic voltammetry, SEM and EDX studies*, Electrochim. Acta **53** (2008), 2600–2609.

[300] S. Brehme, F. Fenske, W. Fuhs, E. Nebauer, M. Poschenrieder, B. Selle, and I. Sieber, *Free-carrier plasma resonance effects and electron transport in reactively sputtered degenerate ZnO:Al films*, Thin Solid Films **342** (1999), 167 – 173.

[301] Z. Qiao, C. Agashe, and D. Mergel, *Dielectric modeling of transmittance spectra of thin ZnO:Al films*, Thin Solid Films **496** (2006), 520–525.

[302] F. Ruske, A. Pflug, V. Sittinger, B. Szyszka, D. Greiner, and B. Rech, *Optical modeling of free electron behavior in highly doped ZnO films*, Thin Solid Films **518** (2009), 1289–1293.

[303] L. C. Lew Yan Voon, M. Willatzen, M. Cardona, and N. E. Christensen, *Terms linear in k in the band structure of wurtzite-type semiconductors*, Phys. Rev. B **53** (1996), 10703–10714.

[304] J. Hinze and K. Ellmer, *In situ measurement of mechanical stress in polycrystalline zinc-oxide thin films prepared by magnetron sputtering*, J. Appl. Phys. **88** (2000), 2443–2450.

[305] J. Han, W. Qiu, and W. Gao, *Potential dissolution and photo-dissolution of ZnO thin films*, J. Hazard. Mater. **178** (2010), 115 – 122.

[306] A. W. Hassel, K. Fushimi, and M. Seo, *An agar-based silversilver chloride reference electrode for use in micro-electrochemistry*, Electrochem. Commun. **1** (1999), 180 – 183.

[307] S. O. Klemm, J.-C. Schauer, B. Schuhmacher, and A. W. Hassel, *A microelectrochemical scanning flow cell with downstream analytics*, Electrochim. Acta **56** (2011), 4315–4321.

[308] B. Szyszka, *Transparent and conductive aluminum doped zinc oxide films prepared by mid-frequency reactive magnetron sputtering*, Thin Solid Films **351** (1999), 164 – 169.

[309] A. V. Naumkin, A. Kraut-Vass, S. W. Gaarenstroom, and C. J. Powell, *NIST X-ray Photoelectron Spectroscopy Database*, NIST Standard Reference Database 20, Version 4.1 (2012), http://srdata.nist.gov/xps/.

[310] W. H. Brattain and C. G. B. Garret, *Experiments on the Interface between Germanium and an Electrolyte*, Bell Syst. Techn. J. **34** (1955), 129–176.

[311] R. Memming and G. Schwandt, *Anodic dissolution of silicon in hydrofluoric acid solutions*, Surf. Sci. **4** (1966), 109 – 124.

[312] P. H. L. Notten, J. E. A. M. van der Meerakker, and J. J. Kelly, *Etching of III-V semiconductors*, Elsevier, Oxford, 1991.

[313] R. Memming and G. Schwandt, *Electrochemical properties of gallium phosphide in aqueous solutions*, Electrochim. Acta **13** (1968), 1299 – 1310.

[314] R. Williams, *Becquerel Photovoltaic Effect in Binary Compounds*, J. Chem. Phys. **32** (1960), 1505–1514.

[315] E. H. Rhoderick and R. H. Williams, *Metal semiconductor contacts.*, 2. ed. ed., Oxford science publications. electronic engineering ; 19., Clarendon Pr., Oxford, 1988.

[316] H. Gerischer, *The impact of semiconductors on the concepts of electrochemistry*, Electrochim. Acta **35** (1990), 1677–1699.

[317] U. Rau and J. H. Werner, *An Analytical Model for Rectifying Contacts on Polycrystalline Semiconductors*, Solid State Phenom. **67-68** (1999), 553–558.

[318] T. Hoar, D. Mears, and G. Rothwell, *The relationships between anodic passivity, brightening and pitting*, Corros. Sci. **5** (1965), 279–289.

[319] D. C. W. Kannangara and B. E. Conway, *Zinc Oxidation and Redeposition Processes in Aqueous Alkali and Carbonate Solutions*, J. Electrochem. Soc. **134** (1987), 894–906.

[320] C. Wöll, *The chemistry and physics of zinc oxide surfaces*, Prog. Surf. Sci. **82** (2007), 55–120.

[321] L. Baugh, *Corrosion and polarization characteristics of zinc in neutral - acid media - I. Pure zinc in solutions of various sodium salts*, Electrochim. Acta **24** (1979), 657–667.

[322] E. E. Abd El Aal, *Effect of* Cl^- *anions on zinc passivity in borate solution*, Corros. Sci. **42** (2000), 1–16.

[323] I. M. Kolthoff, *Treatise on analytical chemistry - theory and practice*, 2. ed. ed., Treatise on analytical chemistry ; 1,2., Vol. 2, Wiley,, New-York, NY, 1979.

[324] I. Katsounaros, J. C. Meier, S. O. Klemm, A. A. Topalov, P. U. Biedermann, M. Auinger, and K. J. J. Mayrhofer, *The effective surface pH during reactions at the solid-liquid interface*, Electrochem. Commun. **13** (2011), 634–637.

[325] E. Bustarret, M. A. Hachicha, and M. Brunel, *Experimental determination of the nanocrystalline volume fraction in silicon thin films from Raman spectroscopy*, Appl. Phys. Lett. **52** (1988), 1675–1677.

[326] L. Houben, M. Luysberg, P. Hapke, R. Carius, F. Finger, and H. Wagner, *Structural properties of microcrystalline silicon in the transition from highly crystalline to amorphous growth*, Philosophical Magazine A **77** (1998), 1447–1460.

[327] C. Smit, R. A. C. M. M. van Swaaij, H. Donker, A. M. H. N. Petit, W. M. M. Kessels, and M. C. M. van de Sanden, *Determining the material structure of microcrystalline silicon from Raman spectra*, J. Appl. Phys. **94** (2003), 3582–3588.

[328] Y. Mai, S. Klein, R. Carius, J. Wolff, A. Lambertz, F. Finger, and X. Geng, *Microcrystalline silicon solar cells deposited at high rates*, J. Appl. Phys. **97** (2005), 114913.

[329] K. Sharma, M. V. Ponomarev, M. C. M. van de Sanden, and M. Creatore, *On the effect of the underlying ZnO:Al layer on the crystallization kinetics of hydrogenated amorphous silicon*, Appl. Phys. Lett. **102** (2013), 212107.

[330] T. Sontheimer, S. Scherf, C. Klimm, C. Becker, and B. Rech, *Characterization and control of crystal nucleation in amorphous electron beam evaporated silicon for thin film solar cells*, J. Appl. Phys. **110** (2011), 063530.

[331] R. Könenkamp, R. C. Word, M. Dosmailov, and A. Nadarajah, *Pentagonal ZnO nanorods*, Phys. Status Solidi R **1** (2007), 101–103.

[332] J. Tang, J.-J. Zheng, Y.-T. Yu, l. Chen, N. Zhang, and Z. Tian, *Selective etching of ZnO films on an ITO substrate using a scanning electrochemical microscope*, Electrochim. Acta **83** (2012), 247–252.

[333] J. Hüpkes, H. Zhu, J. Owen, G. Jost, and E. Bunte, *Instabilities in reactive sputtering of ZnO:Al and reliable texture-etching solution for light trapping in silicon thin film solar cells*, Thin Solid Films **520** (2012), 1913 – 1917.

[334] N. Fujimura, T. Nishihara, S. Goto, J. Xu, and T. Ito, *Control of preferred orientation for* ZnO_x *films: control of self-texture*, J. Cryst. Growth **130** (1993), 269–279.

[335] G. Schöpe, *DC-Sputtern transparenter, leitfähiger Zinkoxidschichten für Dünnschichtsolarzellen von metallischen Zn:Al-Targets*, Master's thesis, Fachhochschule Aachen, 1998.

[336] T. Repmann, *Stapelsolarzellen aus amorphem und mikrokristallinem Silizium*, Ph.D. thesis, RWTH Aachen, 2003.

[337] J. M. Palmer and B. G. Grant, *The Art of Radiometry*, SPIE Pres, 2010.

[338] Y. Gotoh, A. Adachi, and M. Mizuhashi, *Evaluation of optical absorption of textured TCO substrates using immersion liquid*, Rep. Res. Lab. Asahi Glass Co. Ltd. **37** (1987), 13–21.

[339] M. Mizuhashi, Y. Gotoh, and K. Adachi, *Texture Morphology of* SnO_2*:F Films and Cell Reflectance*, Jpn. J. Appl. Phys. **27** (1988), 2053–2061.

[340] W. B. Jackson, N. M. Amer, A. C. Boccara, and D. Fournier, *Photothermal deflection spectroscopy and detection*, Appl. Opt. **20** (1981), 1333–1344.

[341] N. M. Amer and W. B. Jackson, *Optical Properties of Defect States in a-Si:H*, Semiconductors and Semimetals (J. J. Pankove, ed.), Vol. 21 B, Academic Press, New York, 1984, p. 83.

[342] D. Ritter and K. Weiser, *Suppression of interference fringes in absorption measurements on thin films*, Opt. Commun. **57** (1986), 336 – 338.

[343] L. J. van der Pauw, *A Method of Measuring the Resistivity and Hall Coefficient on Lamellae of Arbitrary Shape*, Philips Tech. Rev. **20** (1958/1959), 220–224.

[344] H. H. Wieder, *Electrical and galvanomagnetic measurements on thin films and epilayers*, Thin Solid Films **31** (1976), 123 – 138.

[345] J. W. Orton and M. J. Powell, *The Hall effect in polycrystalline and powdered semiconductors*, Rep. Prog. Phys. **43** (1980), 1263.

[346] C. V. Raman and K. S. Krishnan, *The optical analogue of the Compton effect*, Nature **121** (1928), 711.

[347] P. Persans, *Raman scattering as a probe of structure in amorphous multilayers*, Amorphous Silicon and Related Materials Vol. B (H. Fritzsche, ed.), World Scientific Publishing Company, 1988, p. 1045–1170.

[348] F. Köhler, *Zur Mikrostruktur siliziumbasierter Dünnschichten für die Photovoltaik*, Ph.D. thesis, Rheinisch-Westphälische Technische Hochschule, 2012.

[349] J. Metzdorf, *Calibration of solar cells. 1: The differential spectral responsivity method*, Appl. Opt. **26** (1987), 1701–1708.

[350] T. Wittchen, H.-C. Holstenberg, D. Hunerhoff, J. Zhang, and J. Metzdorf, *Solar cell calibration and characterization: simplified DSR apparatus*, Proc. 20th IEEE PVSC, Vol. 2, 1988, pp. 1251–1257.

[351] T. Kirchartz, K. Ding, and U. Rau, *Fundamental Electrical Characterization of Thin-Film Solar Cells*, pp. 33–60, Wiley-VCH, 2011.

[352] P. J. Mohr, B. N. Taylor, and D. B. Newell, *CODATA recommended values of the fundamental physical constants: 2010*, Rev. Mod. Phys. **84** (2012), 1527–1605.

[353] N. Ashkenov, B. N. Mbenkum, C. Bundesmann, V. Riede, M. Lorenz, D. Spemann, E. M. Kaidashev, A. Kasic, M. Schubert, M. Grundmann, G. Wagner, H. Neumann, V. Darakchieva, H. Arwin, and B. Monemar, *Infrared dielectric functions and phonon modes of high-quality ZnO films*, J. Appl. Phys. **93** (2003), 126–133.

[354] D. Reynolds, D. Look, and B. Jogai, *Optically pumped ultraviolet lasing from ZnO*, Solid State Commun. **99** (1996), 873 – 875.

[355] R. K. Swank, *Surface Properties of II-VI Compounds*, Phys. Rev. **153** (1967), 844–849.

A. Methods and materials

This chapter provides the reader with details on all relevant information about the deposition systems, the measurement setups and conditions, and the samples which were used. The properties of each setup, the manufacturers, and estimations on the measurement errors are addressed.

A.1. Sputter Deposition Systems

Two sputter deposition systems were utilized for the deposition of different ZnO:Al and In_2O_3:Sn thin films as well as Ag solar cell back reflectors. The TCO thin films were deposited on (10 cm × 10 cm) *Eagle XG* glass substrates (Corning Inc., Corning, NY, USA). Prior to deposition, substrates were cleaned by sonication in a warm (65 °C) basic solution.

A.1.1. Zinc Oxide Sputter Deposition

All ZnO:Al thin films investigated in this work were sputter deposited in a commercially available vertical in-line system *VISS 300* (VON ARDENNE Anlagentechnik GmbH, Dresden, Germany). The system can handle samples up to 30 cm × 30 cm. However, for the depositions in this work only 10 cm × 10 cm samples were used of which up to nine can be mounted on the carrier. The carrier is moved dynamically in front of the ZnO:Al target during the deposition in order to enhance homogeneity of the resulting thin films. The layer thickness can be altered by the transport speed and the amount of cycles passing the target. Samples were heated for at least one hour prior to deposition. The base pressure before deposition is 8×10^{-5} Pa. The flow of the argon sputtering gas and reactive oxygen gas are controlled by mass flow controllers. The target was pre-sputtered for at least 10 min before the substrates made a first pass in front of the target. Further details on the sputter system can be found elsewhere [333].

If not stated otherwise, the ZnO:Al thin films utilized in this work were deposited using RF magnetron sputtering (13.56 MHz) from a planar ceramic target consisting of ZnO with 1 w/w% Al_2O_3 (Cerac Inc., Milwaukee, WI, USA). The deposition was carried out at a substrate temperature of 300 °C, a discharge power density of $2\,\mathrm{W\,cm^{-2}}$, and an Ar pressure of 0.1 Pa. During the process the carrier passed the target 27 times. Details about the process have been published in Ref. [3]. Furthermore, a DC cathode is available in the same processing chamber which is equipped with a silver target used for the deposition of back reflectors for solar cells.

The as-deposited polycrystalline layers had a relatively homogeneous thickness with a maximum variation around 6 % over the 30 cm × 30 cm area. The thickness variation over a single 10 cm × 10 cm sample was approximately 2 %. Thus, for a standard thickness deposition with a target value of 800 nm, the thickness could vary up to 50 nm from one 10 cm × 10 cm substrate to another, and less than 20 nm over a single substrate. The crystalline grains were approximately 100 nm in diameter oriented along the c-axis [334].

A.1.2. Indium Tin Oxide Sputter Deposition

The In_2O_3:Sn thin films used as substrates for the electrodeposition of ZnO (see chapter 4) were deposited in a static sputtering system (Kurt J. Lesker Company, Jefferson Hills, PA, USA). A circular target with a diameter of 15.24 cm (6 inches) is mounted onto a cathode in a distance of 10 cm from the substrate holder. During pre-sputtering a movable shutter separates the direct path between the target and the substrate. Samples are heated from the backside by radiative heating from an isothermal metal plate located two cm above the substrate holder, the metal plate is heated by two halogen lamps. Two turbo pumps, one for the loading chamber and one for the sputtering chamber, evacuate the system. During sputtering, the pressure is controlled by an adjustable valve in front of the turbo pump, and the sputtering gas stream is controlled by mass flow controllers.

The In_2O_3:Sn thin films were RF sputter deposited from a In_2O_3:SnO_2 target (Umicore, Brussels, Belgium) with a SnO_2 content of 5 w/w%. The base pressure before sputtering was 4×10^{-7} mbar. During sputtering a power of 190 W was applied and the substrate was maintained at room temperature. The argon and oxygen gas flows were 9 sccm and 1 sccm, respectively. Note that the oxygen content in the oxygen precursor gas was only 1 %. The deposition time was 3 min. Details on the homogeneity of the thin films can be found elsewhere [335].

A.2. Solar Cell Deposition

All silicon layers within this work were deposited in an in-house modified plasma enhanced chemical vapor deposition (PECVD) system (Materials Research Group, Inc., Roselle, NJ, USA) which can handle samples with sizes up to 30 cm × 30 cm. Hydrogen and silane were used as precursor gases for silicon. During deposition of *p*- and *n*-type silicon additionally trimethylborane and phosphine gases, respectively, were introduced. An RF plasma excitation frequency of 13.56 MHz was used to enhance gas decomposition allowing for substrate temperatures below 250 °C. Additional details on the PECVD system can be found elsewhere [336].

A.3. Electrochemical Measurements

Electrolytes were prepared from ultrapure deionized water (18 MΩ, Millipore, Schwalbach, Germany) and analytical grade chemicals. The determination of pH values and conductivities of electrolyte solutions was conducted utilizing an *inoLab Level 3* measuring system (WTW GmbH & Co. KG, Weilheim, Germany). The accuracy is specified to be below ±0.5 %.

Electrochemical experiments have been performed with a *Gamry Reference 600* (C3, Haar, Germany) potentiostat/galvanostat. It is capable of measuring impedance spectra in the frequency range between 10 µHz and 1 MHz and has a minimum voltage and current resolution of 1 µV and 20 aA, respectively. The accuracy of the measured potential and current are ±0.3 % and ±0.3 % of the selected current range, respectively.

The TCO samples investigated in this work were either 100 mm × 100 mm, 50 mm × 50 mm, 50 mm × 25 mm, or 50 mm × 11 mm. The actual geometrical area exposed to the electrolyte was measured by means of a micrometer caliper in order to be able to report current densities J and charge densities Q independent of the sample size. The measurement error of a length measurement was estimated to be ±0.2 mm, which corresponds to an measurement error of 0.122 cm^2 for a sample area of 5 cm × 1.1 cm. By simple calculations using propagation of uncertainty and taking into account the accuracy of the potentiostat (0.18 mA for the current range up to 60 mA) a relative error of 4 % for the current density was determined for these samples and can be regarded as an upper limit for all measurements since the relative error decreases with sample size and is in most cases well below. The same relative error applies for the reported charges in mC cm^{-2}.

Two different electrochemical cells were used for the electrochemical measurements. A temperature controlled double-walled glass cell and an in-house built cell for samples of 10 cm × 10 cm. Most measurements were conducted in the smaller glass cell. If not stated otherwise, the electrochemical measurements were conducted in a conventional three-electrode setup, utilizing a Pt mesh (5 cm × 5 cm, Goodfellow GmbH, Bad Nauheim, Germany) as counter electrode (CE) and an Ag|AgCl|3 M KCl reference electrode (RE, Deutsche Metrohm, Filderstadt, Germany) to which all given potentials are referred.

The temperature control during chemical and electrochemical measurements was provided by a bath/circulation thermostat *Ecoline Staredition E306* (LAUDA Dr. R. Wobser GmbH & Co. KG, Lauda-Königshofen, Germany). A temperature range of room temperature to 90 °C was accessible with an accuracy of ±0.5 °C.

With focus on upscaling the developed processes for the application in a standard solar cell geometry at IEK-5 a suitable electrochemical cell for samples of 10cm × 10cm was designed and constructed within the frame of this work. It consists of a bottom of stainless steel on which the ZnO:Al coated glass samples are placed and a frame made of polyether ether ketone with excellent mechanical and chemical resistance properties that are retained to high temperatures. The frame is mounted on the bottom part by screws. A technical drawing is depicted in Fig. A.1. The contact to the TCO layer was provided by a conductive silver-covered silicone ring pressed onto the sample surface along the edges. It was isolated from the electrolyte by an O-ring seal. The actual contacting was done through two Cu contact pins pressing through the frame on the silver-covered silicone ring (see Fig. A.1).

As a counter electrode (CE) a Pt grid was clamped in a second frame and is placed in parallel above the substrate. A *CHI111* Ag|AgCl|3 M KCl electrode (CH Instruments, Inc., Austin, TX, USA) was used as a reference. Temperature control was provided by a hot plate on which the cell was placed during measurements and a temperature sensor mounted in the bottom.

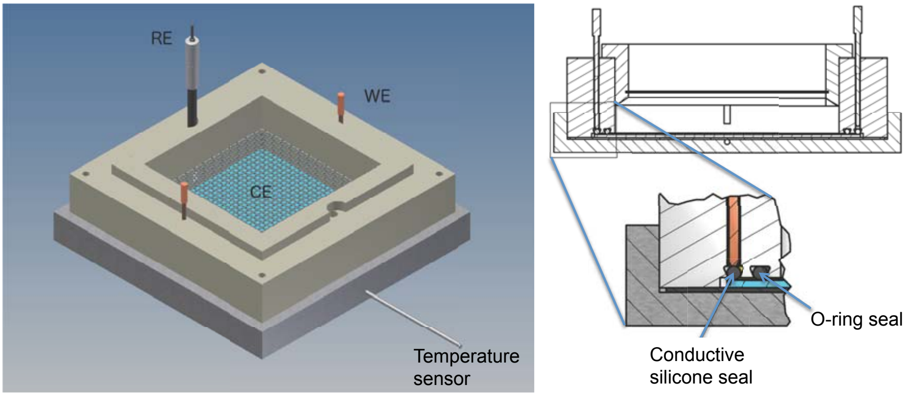

Fig. A.1. Technical drawing of the constructed electrochemical cell for the treatment of10 cm × 10 cm samples. See text for details.

A.4. Physical and Chemical Characterization of Thin Films

A.4.1. Profilometer

Film thicknesses have been measured with a *Dektak 3030* surface profiler (Veeco Instruments Ltd., Santa Barbara, CA, USA). It provides a measuring range of 10 nm to 1.31×10^5 nm. The vertical resolution in the range used in this work (up to 6.55×10^2 nm) is specified to be1 nm. The profilometer can collect 0.04 – 40 data points per µm and offers a scan length of 50 µm to 50 mm. Levelling to correct for a tilt is available and the probe is a diamond stylus of 12.5 µm tip radius. Positioning is done with an x-y positioning system.

The film thicknesses of ZnO layers were determined by scanning a step prepared beforehand by means of masked etching in 2 w/w% HCl. The accuracy of the measurement can be increased by repetitive measurements. For flat samples a measurement error below 10 nm is reasonable. However, the surface roughness of chemically textured ZnO layers often exhibit vertical feature sizes of several 100 nm in direction. The probe tip diameter, however, is too wide to detect the fine structure of these features, leading to a systematic overestimation of the measured film thickness at a measured step. Thus an error of ±50 nm is estimated for rough samples.

A.4.2. UV-VIS-NIR Photospectroscopy

Optical measurements were performed using a dual beam photospectrometer *Lambda 950* (Perkin Elmer, Waltham, MA, USA). As light sources it uses a tungsten-halogen and a deuterium lamp and features a holographic grating monochromator. Furthermore two detectors are used. For the ultraviolet to visible (UV/Vis) wavelength range a photomultiplier (R6872) is used, while the near infrared (NIR) wavelength range is evaluated with a Peltier-cooled PbS detector. Thus, the setup allows for the determination of reflectance as well as both total and diffuse transmittance in the spectral range between 175 and 3300 nm. For diffuse transmittance measurements an integrating sphere (Ulbricht sphere) is used [337]. The measurement error is estimated to be below 1 %. Diiodomethane (CH_2I_2) was used for refractive index matching on rough samples to avoid measurement errors due to light scattering and internal light trapping [338, 339].

A.4.3. Photothermal Deflection Spectroscopy (PDS)

The photothermal deflection spectroscopy (PDS) measurements were performed utilizing an in-house built setup. A typical setup and the evaluation procedure for the calculation of the absorption coefficient α can be found elsewhere [340–342]. The measurement error is assumed to be below 10 %.

A.4.4. Hall Measurements

A van der Pauw setup *RH 2030* (PhysTech GmbH, Moorsburg, Germany) was used for ex-situ electrical characterization of TCO films under ambient conditions [343]. Measurements in the current range between 1 nA and 10 mA are feasible. The maximum resolution is 25 pA. The voltage measurement facility can measure in the range between 10 µV and 10 V with a resolution below 1 µV. The voltage range is selected automatically and the input resistance is higher than 10^{13} Ω. The magnetic field is provided by an *N38 Magnet* (Oxford Instruments, Abingdon, UK) with a magnetic flux density of 0.82 T. The sample geometry was quadratic with an edge length of 11 cm × 11 cm. In the corners of the sample four pins were pressed onto the surface to form ohmic contacts.

Theoretically the setup is able to determine resistances between $1 \times 10^{-3}\,\Omega$ and $1 \times 10^{9}\,\Omega$. For a 1 µm thick layer this translates in a resistivity range of $1 \times 10^{-5}\,\Omega\,\mathrm{cm}$ to $1 \times 10^{7}\,\Omega\,\mathrm{cm}$ and a charge carrier concentration of $1 \times 10^{7}\,\mathrm{cm}^{-3}$ to $1 \times 10^{21}\,\mathrm{cm}^{-3}$. However, for samples with carrier concentrations below $1 \times 10^{18}\,\mathrm{cm}^{-3}$ the contact resistance makes a reliable measurement difficult.

The measurement error is assumed to be 5 % for the resistance and the charge carrier mobilities. For the resistivity and the charge carrier concentrations additionally the error of the layer thickness measurement has to be taken into account (see subsection A.4.1) leading to an estimated measurement error of $< 10\,\%$ for rough samples and $< 6\,\%$ for flat samples. A comprehensive discussion on measurement errors in Hall measurements of polycrystalline thin films can be found elsewhere [344, 345].

A.4.5. Scanning Electron Microscopy (SEM)

Scanning electron microscopic (SEM) images have been recorded utilizing a *Magellan 400* SEM (FEI Company, Hillsboro, OR, USA) or a *LEO Gemini 1550* (Carl Zeiss NTS GmbH, Oberkochen, Germany), respectively. Topography images were recorded with an incident electron beam at an angle of 50°.

The *LEO Gemini 1550* features a field emission cathode. The acceleration voltage was adapted to the individual samples in the range of 5 – 20 kV. Particularly for low conductive samples small voltages were applied in order to prevent charging effects. An in-lens detector and an Everhart-Thornley type of detector (SE2) for the detection of both secondary electrons and back scattered electrons were available. The maximum resolution is in the range of 1 -10 nm depending on the sample properties.

The *Magellan 400* offers a Schottky type emitter and can operate in a wide rang of acceleration voltages between 1 and 30 kV with a specified resolution below 1 nm. It is equipped with an in-lens detector for secondary and back scattered electrons, an Everhardt Thornley detector for secondary electrons, and a retractable low-kV, high contrast solid state detector (vCD).

A.4.6. Focused Ion Beam (FIB)

The preparation of thin film cross sections by means of focused ion beam (FIB) was performed using a *Helios NanoLab 600i* (FEI Company, Hillsboro, OR, USA). It allows for the parallel treatment with ion beam and imaging with electron beam. The included SEM features a Schottky thermal field emitter and offers a resolution below 1.4 nm in the voltage range between 1 kV and 30 kV. It uses an in-lens detector for secondary and backscattered electrons, an Everhart-Thornley detector for secondary electrons and an ion conversion and electron detector for secondary ions and electrons. The maximum resolution of the ion beam is specified to be below 4.0 nm. Prior to ion beam cutting a thin Pt layer was sputtered locally on the area to be treated to avoid surface damaging by the ion beam.

A.4.7. X-ray Photoelectron Spectroscopy

X-ray photoelectron spectroscopy (XPS) measurements were performed using a *PHI 5000 VersaProbe II* system (Physical Electronics, Inc, Chanhassen, Minnesota, USA). Monochromatic Al Kαradiation was used to probe the samples. The reported binding energies were referenced to the C1s electron peak due to residual hydrocarbons on the sample surface, taken at 285.0 eV. After subtraction of a Shirley background, the data were fitted with Gaussian/Lorentzian functions to quantify the amount of the particular elements.

A.4.8. Raman Spectroscopy

The crystalline volume fraction of Si thin films was measured using Raman spectroscopy [346, 347]. A laser with a wavelength of $\lambda = 488$ nm was used to probe the Si layers through the glass/ZnO:Al substrate. The corresponding information depth in microcrystalline Si is approximately 150 nm, depending on the crystallinity [348]. After substraction of the ZnO:Al background signal the Raman spectra were evaluated as reported in Ref. [325–327]. An error of 3 % was estimated in the reported crystallinity values.

A.5. Solar Cell Characterization

A.5.1. Spectral Response and Quantum Efficiency

Spectral response (*SR*) measurements of solar cells were performed upon monochromatic illumination with a chopped light beam from a xenon lamp using lock-in technique. Therefore a monochromator was used to select specific wavelengths in the spectral range between 300 nm and 1100 nm in 10 nm increments. The quantum efficiency (*QE*) of a solar cell as a function of wavelength λ is given by

$$QE(\lambda) = SR(\lambda)\frac{\mathrm{h\,c}}{\mathrm{e}\,\lambda} \tag{A.1}$$

with h, c, and e being the Planck constant, speed of light, and elementary charge, respectively. To determine the individual *QE* of a top (bottom) subcell in a tandem device, the bottom (top) cell was saturated continuously with light of long (short) wavelength that is only absorbed in the bottom (top) cell. Therewith, the subcell of interest was always limiting the current of the tandem device. The relative error for the *QR* measurements was less than 2 %. Additional details on the measurement setup and the determination of quantum efficiencies can be found elsewhere [349–351].

A.5.2. Current-Voltage Characteristic

Solar cell characteristics were determined by measuring the current density as a function of voltage with a source-measurement unit *SMU 238* (Keithley Instruments, Inc., Solon, OH, USA) upon illumination. Measurements were performed under standard test conditions, *i.e.* illumination with AM1.5 spectrum of 100 mW cm^{-2} and a temperature of 25 °C. The solar spectrum was provided by a class A double source (xenon and halogen) solar simulator (*WXS-140S-Super*, Wacom Electric Co., Saitama, Japan). It was calibrated prior to measurements using a photodiode (*S1236-8BQ*, Hamamatsu Photonics Deutschland GmbH, Herrsching am Ammersee, Germany). A deviation of less than 2 % was observed upon repeated measurement of the same solar cell. Details of current-voltage measurements on thin film solar cells can be found in Ref. [351].

Glossary

Common Abbreviations

Acronym	**Meaning**
AC	alternating current
AM	air mass
CE	counter electrode
CVD	chemical vapor deposition
DC	direct current
ECD	electrochemical deposition
EQE	external quantum efficiency
FF	fill factor
FIB	focused ion beam
GB	grain boundary
HER	hydrogen evolution reaction
ICP-MS	inductively coupled plasma - mass spectroscopy
IEK-5	Institut für Energie- und Klimaforschung 5
IR	infrared
ITO	indium tin oxide (In_2O_3:Sn)
IQE	internal quantum efficiency
NIR	near infrared
OCP	open circuit potential
OER	oxygen evolution reaction
PDS	photothermal deflection spectroscopy
PECVD	plasma enhanced chemical vapor deposition
PLD	pulsed laser deposition
PZC	point of zero charge
RE	reference electrode
RF	radio frequency (13.56 MHz)
RPM	rounds per minute
RT	room temperature
sccm	standard cubic centimeter per minute ($cm^3/(60\ s)$ at 101325 Pa and 273.15 K)
SEM	scanning electron microscopy

SHE	standard hydrogen electrode
TCO	transparent conductive oxide
UHV	ultra-high vacuum
UV	ultraviolet
Vis	visual
XPS	x-ray photoelectron spectroscopy
XRD	x-ray diffraction

Formula Abbreviations

Symbol	**Description**	**Unit**
a_0^*	effective Bohr radius	nm
A	absoptance	
A	area	cm^2
d	thickness	nm
d_{eff}	effectively dissolved thickness	nm
C	capacity	F
C_{sc}	capacity of the space charge region	F
C_{H}	capacity of electrochemical double layer	F
E	potential	V
E°	standard electrode potential	V
$\vec{E}$	electric field	$\mathrm{V\,m^{-1}}$
E_{C}	conduction band energy	eV
E_{F}	Fermi energy	eV
E_{fb}	flat band potential	V
E_{g}	band gap energy	eV
E_{onset}	onset potential	V
E_{photon}	energy of incident light	eV
E_{V}	valence band energy	eV
E_{t}	trap state energy	eV
f	frequency	Hz
G	Gibbs energy	J
I	current	A
$I_{\mathrm{C}}^{\mathrm{RS}}$	crystalline volume fraction	
j	current density	mA
j_0	dark saturation current	$\mathrm{mA\ cm^{-2}}$
j_{sc}	short circuit current density	$\mathrm{mA\ cm^{-2}}$

k	imaginary part of refractive index (extinction coefficient)	
m_h^*	effective hole mass	
m_e^*	effective electron mass	g
M	molar mass	$\mathrm{g\,mol^{-1}}$
n	electron density	$\mathrm{cm^{-3}}$
n	refractive index	
N_A	acceptor density	$\mathrm{cm^{-3}}$
N_C	state density at conduction band	$\mathrm{eV^{-1}\ cm^{-3}}$
N_D	donor density	$\mathrm{cm^{-3}}$
N_V	state density at valence band	$\mathrm{eV^{-1}\ cm^{-3}}$
n_i	intrinsic charge carrier density	$\mathrm{cm^{-3}}$
N_i	number of particles of species i	
N_t	trap state density	$\mathrm{cm^{-3}}$
p	hole density	$\mathrm{cm^{-3}}$
p	pressure	mbar
P	power	W
q	charge density	$\mathrm{mC\,cm^{-2}}$
Q	charge	C
R	resistance	Ω
R	reflectance	
R_ct	charge transfer resistance	Ω
R_P	parallel resistance	$\Omega\ \mathrm{cm^{-2}}$
R_S	series resistance	$\Omega\ \mathrm{cm^{-2}}$
R_sh	sheet resistance	Ω
t	time	s
T	transmittance	
T	temperature	K or °C
T_t	total transmittance	
$\vec{v}$	velocity (*e.g.* of an electron)	$\mathrm{m\,s^{-1}}$
V_H	potential drop across the Helmholtz layer	mV
V_oc	open circuit voltage	mV
W	width of the space charge region	cm
x	stoichiometry number	
z	charge number	
z_i	charge number of species i	

Greek symbols

Symbol	**Description**	**Unit**
α	absorption coefficient	μm^{-1}
ϵ_r	relative dielectric constant	
η	efficiency	%
λ	wavelength	nm
μ_i	chemical potential of species i	J mol^{-1}
$\tilde{\mu}_i$	electrochemical potential of species i	J mol^{-1}
μ_n	electron mobility	cm^{2}V^{-1}s^{-1}
μ_p	hole mobility	cm^{2}V^{-1}s^{-1}
ν	scan rate	mV s^{-1}
ν	frequency	Hz
ν_{mol}	rate of dissolution	mol cm^{-2} s^{-1}
ν_d	rate of dissolution	nm s^{-1}
ϕ	inner potential	V
φ_{sc}	potential drop across the space charge region	V
ρ	mass density	g cm^{-3}
ρ	resistivity	Ω cm
σ	electric conductivity	S cm^{-1}
τ	charge carrier lifetime	μs
ω	angular frequency	rad s^{-1}
ω_p	plasma frequency	rad s^{-1}

Chemical symbols

μc-Si:H	hydrogenated microcrystalline silicon
a-Si:H	hydrogenated amorphous silicon
Cl^-	chloride ion
SO_4^{2-}	sulfate ion
PO_4^{3-}	phosphate ion
H_2	hydrogen
H_2O	water
H_2O_2	hydrogen peroxide
H_2SO_4	sulfuric acid
HCl	hydrochloric acid

$HClO_4$	perchloric acid
HF	hydrofluoric acid
HNO_3	nitric acid
HSO_4^-	hydrogen sulfate
In_2O_3:Sn	tin-doped indium oxide
K_2SO_4	potassium sulfate
$K_3[Fe(CN)_6]$	potassium hexacyanoferrat
KCl	potassium chloride
$KClO_4$	potassium perchlorate
KNO_3	potassium nitrate
NaCl	sodium chloride
NO_3^-	nitrate ion
SiH_4	mono silane
SnO:F	fluoride-doped tin oxide
Zn^{2+}	zinc ion
ZnO	zinc oxide
ZnO:Al	aluminum-doped zinc oxide
ZnO:Ga	gallium-doped zinc oxide
$Zn(OH)_2$	zinc hydroxide

Constants

Avogadro constant	N_A	$= 6.022\,141\,29(27) \times 10^{23}\ \mathrm{mol^{-1}}$
Boltzmann constant	k_B	$= 1.380\,648\,8(13) \times 10^{-23}\ \mathrm{J\,K^{-1}}$
		$= 8.617\,332\,4(78) \times 10^{-5}\ \mathrm{eV\,K^{-1}}$
Molar gas constant	R	$= 8.314\,462\,1(75)\ \mathrm{J\,mol^{-1}\,K^{-1}}$
Planck constant	h	$= 6.626\,069\,57(29) \times 10^{-34}\ \mathrm{J\,s}$
		$= 4.135\,667\,516(91) \times 10^{-15}\ \mathrm{eV\,s}$
Elementary charge	e	$= 1.602\,176\,565(35) \times 10^{-19}\ \mathrm{C}$
Electron mass	m_e	$= 9.109\,382\,91(40) \times 10^{-31}\ \mathrm{kg}$
Faraday constant	F	$= 96\,485.3365(21)\ \mathrm{C\,mol^{-1}}$
Dielectric constant (vacuum)	ε_0	$= 8.854\,187\,817 \times 10^{-12}\ \mathrm{F\,m^{-1}}$
Temperature at absolute zero	T_0	$= 0\ \mathrm{K} = -273.15\ ^\circ\mathrm{C}$
Speed of light in vacuum	c	$= 299\,792\,458\ \mathrm{m\,s^{-1}}$

Values were taken from Ref. [352].

Material Parameters

Static dielectric constant of ZnO	$\varepsilon^{\perp}$	$= 7.46$	for $E \perp c$	[353]
	$\varepsilon^{\parallel}$	$= 8.59$	for $E \parallel c$	[353]
High frequency dielectric constant of ZnO	$\varepsilon_{\infty}^{\perp}$	$= 3.7$	for $E \perp c$	[353]
	$\varepsilon_{\infty}^{\parallel}$	$= 3.78$	for $E \parallel c$	[353]
Band gap of intrinsic ZnO	E_{g}	$= 3.36\,\mathrm{eV}$		[303, 354]
Intrinsic electron density of ZnO	n_{i}	$< 10^{6}\mathrm{cm}^{-3}$		[59]
Hexagonal lattice constants of ZnO	a	$= 0.325\,\mathrm{nm}$		[54]
	c	$= 0.521\,\mathrm{nm}$		[54]
Ionization energy (= vacuum level - valence band maximum)	E_{ion}	$= 7.82\,\mathrm{eV}$		[355]
molar mass of ZnO	M	$= 81.369\,\mathrm{g\,mol}^{-1}$		[278]
density of ZnO	ρ	$= 5.6730\,\mathrm{g\,cm}^{-3}$		[278]

Publications

Journal Articles

S. E. Pust, J.-P. Becker, J. Worbs, S. O. Klemm, K. J. J. Mayhofer, and J. Hüpkes, *Electrochemical etching of zinc oxide for silicon thin film solar cell applications*, Journal of the Electrochemical Society **2011**, 158(7), D413-D419

J.-P. Becker, S. E. Pust, and J. Hüpkes, *Effects of the electrolyte species on the electrochemical dissolution of polycrystalline ZnO:Al thin films*, Electrochimica Acta **2013**, 112, 976–982

Oral Presentations

S. E. Pust, J.-P. Becker, S. O. Klemm, J. Worbs, M. Thomas Desessarts, K. J. J. Mayrhofer, J. Hüpkes, *Anodic electrochemical texturing of zinc oxide thin films: mechanistical considerations and application in thin-film silicon solar cells*, Electrochemistry 2012, Munich, Germany, 17 - 19 September 2012

J.-P. Becker, S. E. Pust, and J. Hüpkes, *Electrochemical texturing of ZnO:Al thin films for improved light scattering*, 4th International Symposium on Transparent Conductive Materials, Hersonissos, Crete, Greece, 21 - 26 October 2012

J.-P. Becker, S. E. Pust, and J. Hüpkes, *Anodic electrochemical etching of ZnO:Al thin films for solar cell applications*, 13th Topical Meeting of the International Society of Electrochemistry - Advances in Electrochemical Materials Science and Manufacturing, Pretoria, South Africa, 7 - 10 April 2013

Poster Presentations

J.-P. Becker, S. E. Pust, and J. Hüpkes, *Combined chemical/electrochemical etching of ZnO:Al for silicon thin-film photovoltaic application*, GDCh Wissenschaftsforum Chemie 2011, Bremen, Germany, 4 - 7 September 2011

J.-P. Becker, S. E. Pust, and J. Hüpkes, *Anodic electrochemical texturing of ZnO:Al thin films*, 12th International Fischer Symposium on ”Frontiers in Nanoelectrochemistry”, Lübeck, Germany, 3 - 7 June 2012

Curriculum Vitae

Name: Jan-Philipp Becker
Date of birth: May 24th, 1982
Place of birth: Berlin (Germany)

1998 - 2001	Secondary school education at the Humboldtschule, Hannover (Germany)
2001	Degree: Abitur
2001 - 2002	Civil service at the Siloah Hospital, Hannover (Germany)
2002 - 2005	Undergraduate studies in physics at the Leibniz Universität Hannover, Hannover (Germany)
2004	Degree: Vordiplom
2005 - 2009	Graduate studies in physics at the Universität Bremen, Bremen (Germany)
2009	Degree: Diplom-Physiker Thesis "Analyse und Optimierung von Silicium-Heteroübergängen" (German)
2006 - 2009	Research Assistant in the Optical Metrology and Optoelectronic Systems Group at the Bremen Institute for Applied Beam Technology BIAS, Bremen (Germany)
2008 - 2010	Research Assistant in the High-Efficiency Cell Fabrication and Analysis Group at the Fraunhofer Institute for Solar Energy Systems, Freiburg (Germany). This work partially served as the basis for the diploma thesis.
2010 - 2013	PhD studies in the Light Scattering Contacts Group of the Photovoltaics Departement at the Institute for Energy and Climate Research at the Forschungszentrum Jülich, Jülich (Germany)
October 2013 - present	Scientist in the Materials and Solar Cell Development Group of the Photovoltaics Departement at the Institute for Energy and Climate Research at the Forschungszentrum Jülich, Jülich (Germany)

Acknowledgements

It is with great pleasure that I thank the many people who helped make this thesis possible, whether directly or indirectly.

I thank Prof. Dr. Uwe Rau for giving me the opportunity to work at a world-renowned institute and for taking such a great interest and supporting me in my research. Prof. Dr. Rau always made time for me; engaging in fruitful discussions, helping me to clarify my goals and the steps that needed to be taken to reach them and providing me with helpful feedback on my research projects. I also kindly thank Prof. Dr. Gunther Wittstock for his willingness to review this thesis and for his generosity in providing me with the possibility to run experiments in his lab.

I would like to express my deep gratitude to Dr. Sascha Pust, for being an excellent advisor. His constant support, encouragement, and invaluable advise enabled me to become acquainted with the field of electrochemisty quickly and gave me the neccessary tools to monitor and handle every situation. As a mentor, he struck the perfect balance between encouraging me to take initiative and direct my own projects and guiding me when I was unable to figure things out on my own. He gently encouraged me towards independence while at the same time giving me the security that he was always there if I needed him.

I would also like to thank Dr. Jürgen Hüpkes, for sharing his profound knowledge on zinc oxide thin films, his critical, yet highly constructive, feedback, his creative ideas and inspiring discussions.

Special thanks go to Magali Thomas Desessarts, Sumana Raj, and Burak Bayindırlı, who were a great support in the lab and allowed me to learn a lot about myself.

I thank all those who helped me with sample preparation: Hildegard Siekmann, Ulrike Gerhards, Alain Doumit, Joachim Kirchhoff, Sandra Tillmanns, Juraj Hotovy, Gunnar Schöpe, Andreas Bauer and the many who assisted with sample characterization: Brigitte Zwaygardt, Josef Klomfaß, Oliver Thimm, Hans-Peter Bochem, Dr. Elmar Neumann, Dr. Uwe Zastrow, Dr. Astrid Besmehn, Markus Hülsbeck, Christoph Zaren, and Wilfried Reetz.

A special thanks also to my direct colleagues for making life at work so much fun and also for all the helpful discussions and comments during group meetings and otherwise. Thank you Dr. Jorj Owen, Nicolas Sommer, Dr. Gabrielle Jost, Marek Warzecha, Erik Schumann, Philipp Stützel, David Wippler, and Dr. Wendi Zhang.

For sharing their expertise on solar cells, I would like to thank Dr. Aad Gordijn, Dr. Tsvetelina Merdzhanova, Dr. Matthias Meier. In addition, I would like to thank Dr. Karl J. J. Mayrhofer and Dr. Sebastian O. Klemm at Max-Planck-Institut für Eisenforschung Düsseldorf and Prof. Dr. Klaus Ellmer and André Bikowski at Helmholtz-Zentrum Berlin for their collaboration and support.

Thank you to my friends and colleagues: Max Siegloch, Stephan Michard, Chao Zhang, Thi Minh Hang Tran, André Hoffmann, Stephan Lehnen, Marvin Goblet, Andreas Lambertz, Jonas Noll, Bugra Turan, Dr.Carolin Ulbrich, Karen Wilken, Félix Urbain for being great colleagues and always offering a helping hand.

I would also like to acknowledge the financial support of the Deutsche Forschungsgemeinschaft (DFG, grant Pu 447/1) for which I am grateful.

This thesis would not exist without the indispensible, enduring, and committed support from my family and friends.

I thank my close friends and flatmates for bringing so much joy and color to my life and for helping me regenerate after stressful weeks: Dr. Malte Prieß, Golnar Afshar, Martin Bivour, Dr. Gerrit Maschwitz, Dr. Kerstin Güssow, Florian Petersen, Hanne Decker, Andreas Voelk and many others.

My warmest gratitude goes to Dr. Sara van Leeuwen for her constant support and unconditional love during the most challenging time of this thesis.

Thank you also to my sister Greta-Marie Becker for her love, her encouragement and for making me proud to be her brother.

Finally, I thank my parents, Dagmar Struckmeier-Becker and Reinhard Becker, who gave me a solid base from which to grow, shared happy and sad moments with me, supported me in every possible way, and always believed in me without a doubt. It is because of their unconditional love and utmost dedication that I have always felt free to follow my dreams.

Band / Volume 233
Numerische Simulationen von Abfallgebinden aus der Wiederaufarbeitung von Kernbrennstoffen
S. Schneider (2014), 201 pp
ISBN: 978-3-89336-998-0

Band / Volume 234
Materials for Advanced Power Engineering 2014
J. Lecomte-Beckers, O. Dedry, J. Oakey, B. Kuhn (Ed.)
(2014), xxi, 930, viii pp
ISBN: 978-3-95806-000-5

Band / Volume 235
Untersuchungen zur Abtrennung, Konversion und Transmutation von langlebigen Radionukliden
Ein Beitrag zur fortschrittlichen Entsorgung von hochradioaktiven Abfällen
G. Modolo (2014), 291 pp
ISBN: 978-3-95806-005-0

Band / Volume 236
Keramische Membranen für die H_2-Abtrennung in CO-Shift-Reaktoren
D. van Holt (2014), IV, 169 pp
ISBN: 978-3-95806-007-4

Band / Volume 237
Entwicklung von porösen Silica-Membranen zur CO_2-Abtrennung aus dem Rauchgas fossil befeuerter Kraftwerke
J. S. Eiberger (2014), II, 163 pp
ISBN: 978-3-95806-008-1

Band / Volume 238
Development of a highly sensitive and versatile mass spectrometer system for laboratory and atmospheric measurements
S. Albrecht (2014), iv, 171 pp
ISBN: 978-3-95806-009-8

Band / Volume 239
High Temperature Corrosion of Alloys and Coatings in Gas-Turbines Fired with Hydrogen-Rich Syngas Fuels
W. Nowak (2014), 201 pp
ISBN: 978-3-95806-012-8

Band / Volume 240
Einfluss neuer Membranmaterialien auf Herstellung und Betrieb von Direktmethanol-Brennstoffzellen
S. Hürter (2014), V, 164 pp
ISBN: 978-3-95806-013-5

Schriften des Forschungszentrums Jülich
Reihe Energie & Umwelt / Energy & Environment

Band / Volume 241
Spannungsinduziertes Versagen in Hochtemperaturschichtsystemen
C. Nordhorn (2014), v, 118 pp
ISBN: 978-3-95806-016-6

Band / Volume 242
Änderungsdetektion digitaler Fernerkundungsdaten mittels objekt-basierter Bildanalyse
C. Listner (2014), 176 pp
ISBN: 978-3-95806-017-3

Band / Volume 243
Räumlich hoch aufgelöste Modellierung des Spaltprodukt-verhaltens in einem HTR-Core mit kugelförmigen oder prismatischen Brennelementen
A. Xhonneux (2014), viii, 239 pp
ISBN: 978-3-95806-020-3

Band / Volume 244
Effects of Cercospora leaf spot disease on sugar beet genotypes with contrasting disease susceptibility
S. Schmittgen (2015), 121 pp
ISBN: 978-3-95806-021-0

Band / Volume 245
Light scattering and trapping in thin film silicon solar cells with an n-i-p configuration
W. Böttler (2015), 132 pp
ISBN: 978-3-95806-023-4

Band / Volume 246
Nanostructured Si-alloys for silicon solar cells
K. Ding (2015), 210 pp
ISBN: 978-3-95806-024-1

Band / Volume 247
Electrochemical Texturing and Deposition of Transparent Conductive Oxide Layers for the Application in Silicon Thin-Film Solar Cells
J.-P. Becker (2015), ix, 156, XXIV pp
ISBN: 978-3-95806-027-2

Weitere ***Schriften des Verlags im Forschungszentrum Jülich*** unter
http://wwwzb1.fz-juelich.de/verlagextern1/index.asp

Energie & Umwelt /
Energy & Environment
Band / Volume 247
ISBN 978-3-95806-027-2

JÜLICH
FORSCHUNGSZENTRUM